Residential and District-Scale Ground-Coupled Heat Pump Performance with Fiber Optic Distributed Temperature Sensing

By

Matthew Dean Walker

A thesis submitted in partial fulfillment of the requirements for the degree of

Master of Science

Geological Engineering

At the

University of Wisconsin-Madison

2015

Residential and District-Scale Ground-Coupled Heat Pump Performance with Fiber Optic Distributed Temperature Sensing

by

Matthew Dean Walker

Approved by

James M. Tinjum, P.E., Associate Professor

January 16, 2015

Abstract

Ground-coupled heat pumps (GCHP) have garnered considerable attention in recent years as an energy-saving alternative to conventional space heating and cooling systems, but there exists some debate about their effectiveness and efficiency. Some of this debate stems from the inherent complexity of the subsurface heat transfer problem; the rate of subsurface heat transfer ultimately drives GCHP system performance. A given GCHP site may have many geologically distinct layers of soil and rock—each with its own macro-scale thermal properties—which complicates the prediction of heat transfer. Even within a given layer, there exists variability in its properties due to depositional processes, weathering, and fracturing.

This work opens with an introduction that prefaces the study and fundamentals of GCHPs, with particular attention paid to the interaction between site geology and heat transfer within the system (Chapter 1). The general concept of using heat pumps for heating and cooling is discussed, and some of the tools for GCHP design, like thermal response tests (TRTs), are briefly explained. The background (Chapter 2) introduces distributed temperature sensing (DTS), the history of its development, and the methods behind its use.

The first paper presented in this thesis (Chapter 3) is a two-part study, the first focusing on recording thermal properties of specific lithofacies in a particular region (Wisconsin, USA), and the second part modeling how these measurements could change expected GCHP design and performance in a typical residential setting. Representative sedimentary, igneous, and metamorphic rocks from Wisconsin were characterized in previous work by Meyer (2013) using guarded-comparative-longitudinal heat flow experiments (ASTM E1225), calorimetry, and weight-volume assessments. The model was developed by coupling the rate of heat extraction in a heat pump to an analytical model of heat transfer through a pipe with constant wall temperature. The constant-wall temperature used in the pipe model was taken from an

implementation of the infinite line source (ILS) model. This strategy allows the modeled heat extraction rate to be limited by the characteristics of the pipe, which is an advantage over using the ILS model on its own. However, coupling ILS to pipe conduction is still a major simplification in modeling subsurface heat transfer.

The indexed thermophysical values from Meyer (2013) and supplemental laboratory measurements were used to construct a hypothetical vertical heat exchange loop penetrating vertically consecutive Paleozoic strata. The hypothetical loop was examined using the rate of system temperature drop under full load as a measure of performance during the heating season. Expected system performance was compared between commonly cited thermal conductivity values of their general lithologies (e.g., sandstone, dolomite, shale) and the laboratory-measured thermal properties of the specific formations. Thermal conductivity indexed by general lithology proved to be insufficient as a design parameter to generate accurate assessments of GSHP performance.

The second paper of this study (Chapter 4) and its appendix (Appendix 1) describe the design and implementation of distributed temperature sensing (DTS) as a method of evaluating subsurface heat transfer. DTS is a measuring technique that utilizes fiber-optic cable to measure temperature along continuous profiles. DTS fibers were deployed permanently in an instrumented GCHP system at a residence located in Grand Marsh, Wisconsin, USA. The site was originally intended to be a test location for an unconventionally deep borehole described in Meyer (2013), but was instead converted to a more traditional system with three vertical ground heat exchangers (GHEs) of ~100 m depth each. However, the system was atypical in a number of ways. Air conditioning, space heating, and domestic hot water were supplied by a pair of heat pumps sharing the same GHE loop. A manifold separately controlling flow to each of the GHEs was constructed to allow the flow circuit to be configured as parallel, series, or single-GHE. Temperature, flow rate, and power sensors were installed on components of the heat pump

system in a plan similar to that described in the appendix of Meyer (2013). This allowed the system's coefficient of performance (COP) to be measured along with weather conditions on the site. The dataloggers collecting these measurements were connected to network-connected laptops for remote monitoring and configuration.

Though monitoring on the site is in the early stages, daily COP observations were made and related to the electrical power consumption of the heat pumps and the weather conditions during the first half of the 2014-2015 heating season. The daily COP was correlated with which of the two heat pumps delivered the majority of heating to the residence on that day. The water-to-air heat pump was the more efficient of the two, so higher proportional use of the water-to-air heat pump was correlated positively to the daily COP. Heating COP was also positively correlated to the entering water temperature (EWT). This outcome was expected because the Carnot efficiency (i.e., the theoretical maximum efficiency for any heat pump or heat engine) is directly related to the temperature difference between the heat source and heat sink. Heat pump usage, as indicated by their electrical power consumption, was correlated with drops in outdoor temperature.

Representative temperature profiles within the system's GHEs were acquired with the DTS system during seasons with different space conditioning requirements. The profiles, which were taken in January of 2014, indicated that heat recovery was lower than desired. The 2013-2014 heating season was colder than normal, with 223 more heating degree days (Celsius) during the Dec-January time period than average for the central Wisconsin region (Wisconsin Department of Administration). The profiles also showed that heat transfer in the horizontal trenches leading to the GHEs was limited at best, and, during extreme conditions, the direction of heat flux within the trenches could be reversed, likely due to the depressed temperature at the trench's shallow depth (2 m). Summer profiles showed that heat was easily transferred to the subsurface, due in

part to relatively cool ambient temperatures underground (<12 °C) and heat already extracted during the preceding heating season.

The final component of this research was the installation of a DTS network at a large heat exchange borefield in Verona, Wisconsin, USA. Described in Appendix 1, this effort has already produced background DTS measurements and will begin to record the effect of activating a portion of the borefield of over 2500 150-m-deep GHEs early in 2015. The DTS array at this borefield features eight double-ended loops of fiber optic cable connecting 13 boreholes, each with a depth of 150 m. The total length of DTS fiber at this system will surpass 10 km.

Acknowledgements

First, I would like to thank the members of my committee, Professors Tinjum, Hart, and Fratta, for their countless hours of work, bountiful knowledge, and forgiving humor. Without their direction and unique skillsets, the studies that I present here would have never been dreamt of, much less implemented in the field. It was their hosting of the Research Experience for Undergraduates in Energy Geotechnics which originally spurred me to pursue research in the Geological Engineering Program's geothermal research group while I was an undergraduate.

I owe the greatest debt of gratitude to my parents, Mike and Peggy Walker. They have ceaselessly supported me through the highs and lows of life. The values that they instilled in me at a young age have made my achievements possible, namely: the value of reading and the value of listening. With those principles, my desire for knowledge has been insatiable ever since I first opened a volume of the *World Book Encyclopedia* at the Harmon household. For that, I owe my maternal grandparents, Maurice and Philomene Harmon, my sincerest thanks. I hope they both would have approved of my choice to attend their home state's flagship institution. My paternal grandparents, Ellsworth and Beverly Walker, constantly supported me during the time we had together. Grandma Walker was always eager to talk to me about my life and research, offering never-ending love and praise till the very end. I also owe thanks to my great-great aunt, Edna Johnson. Edna's passion for amateur geology struck a chord with me as a child, something my dad reminded me of when I sought his advice on which major to choose in my freshman year at Madison. Katie Roberts, thank you for being a constant companion.

Within the geotechnical engineering family, there are too many names to thank individually, but Xiaodong "Buff" Wang warrants special mention as both an extraordinary experimentalist in all aspects of instrumentation and a road trip partner of the highest quality (for which I should also mention Ben Warren and Jiannan "Nick" Chen). I would like to acknowledge the members of the

geothermal research group including Professors Choi and Likos and graduate students Ayse Ozdogan, Lauren Meyer, Saurabh Ghanekar, and Joel Bautista for their support. Lauren built the foundation for my research as the group's first student to graduate, acquiring much of the instrumentation that is used at the Grand Marsh site to this day. Thanks are offered to Bryan Stressler and Andrew Ruetten for their efforts in preparing and conducting thermal conductivity experiments on rock samples. I would also like to thank the most recent additions to the research group, Ian Atkins, Eleanor Bloom, Adam McDaniel, and Levi Mitchell, for their assistance, especially in field work.

The two field projects described in this thesis were supported by people and organizations outside of the support of grants. The efforts of Bruce Walker and Michelle Schank are the basis for all of the work that the research group does in Grand Marsh. Michelle deserves special praise for allowing myself and other members of the group intrude into her home. I would like to thank Epic Systems for hosting our research at Borefield #4 and truly massive donations of time and resources. General Heating & Air Conditioning, Bertram Drilling, Rygan Inc., and Morse Group are also acknowledged for their support in installing instrumentation and advising instrumentation design.

I would like to thank many organizations for their magnanimous gifts. The National Science Foundation supported work at the Grand Marsh field site under Grant Numbers 1156674 and 1317315, "REU Site: Geothermal and Energy Geotechnics" and "RAPID: DTS for Performance Assessment and Long-Term Implications of an Unconventionally Deep Geothermal Exchange Well", respectively. The University of Wisconsin-Madison Graduate School also supported work at the Grand Marsh field site with Wisconsin Well and Water Systems, LLC., under the Innovation & Economic Development Research Program. The Wisconsin Energy Institute Seed Grant and Wisconsin Department of Natural Resources under grant number WR14R002 supported work at our Verona field site. I was also personally supported by teaching

assistantships from UW-Madison's Department of Civil and Environmental Engineering and a project assistantship through the Wisconsin Geological and Natural History Survey funded by the Department of Energy. Any opinions, finding, and conclusions or recommendations expressed in this material are those of the authors and do not necessarily reflect the views of the funding organizations.

Table of Contents

List of Figures

Chapter 1: Introduction

The effect of a heterogeneous distribution of subsurface thermal properties on the performance of ground-coupled heat pumps (GCHPs) has yet to be discerned with great detail. Specifically, the distribution of heat flux between ground-loop heat-exchange fluid and surrounding subsurface media along a vertical ground heat loop is poorly understood. Attempts to model the problem have generally made simplifying assumptions about the subsurface stratigraphy (homogeneous, laterally continuous, etc.) and the distribution of temperatures or heat flux along the ground loop (linear temperature decay, analytical solutions for log temperature difference, etc.). To better understand the problem, this study attempts to experimentally determine heat flux distributions as a function of site geology, seasonal effects, and home heating and cooling demand. This determination was made through the use of system instrumentation and distributed temperature sensing.

1.1 Ground-Coupled Heat Pumps: Geological Perspective

GCHPs are heat pumps usually used for heating and/or cooling homes and businesses, using the subsurface as a heat source or sink. GCHPs have numerous advantages over conventional heating and cooling technologies. These advantages are mostly related to the superior energy efficiency of GCHPs, which may lead to lower operating and environmental costs than other commonly used heating and cooling strategies. However, the aforementioned advantages are dependent on the assumption that GCHPs can operate with significantly higher efficiency than the technologies that they are being compared against. While the heat pump component of a GCHP system may operate efficiently and in a well-understood manner according to manufacturer performance tables, the heat exchanger in contact with the ground, called the ground loop or ground heat exchanger (GHE), is usually subjected to rough guidelines or educated guesses in its design. Importantly, two facilities may have similar heating and cooling

loads, and they may employ the same heat pumps; however, no two sites have the same subsurface conditions. As a result, the overall system design would need to be different in the two cases for the systems to reach similar performance.

The GHE design must also consider many options for its installation beyond its length and the number of boreholes. Different pipe material, pipe geometry, grout material, and fluid types can be implemented for a given site. All of these choices influence the rate of heat transfer and the selection of other system components like circulation pumps. According to many previous studies (e.g., Beier et al. 2012), the grout chosen for the completion of the GHE borehole is especially important. Many standard grouts for well completion work (e.g., drinking water wells) are based at least in part on bentonite. Bentonite and other clays are thermally resistive (relative to sand and rock media), and GHE installers typically replace at least some of the standard grout components with sand, graphite, or other fillers to reduce the effective resistivity of the grouted bore (Lee et al. 2010).

The initial investment for systems properly designed for different geological settings could be vastly different based on the relative favorability of the thermal properties of the site geology. For example, a site with exceptional thermal conductivity may only require a single boring of moderate length to fulfill the heating and cooling demands of the facility, but the identical facility at a site with poor thermal conditions could require much more exchange surface (i.e., more boreholes, longer boreholes, or both) to provide the same capacity. Since the installation of a GHE is by far the most expensive component of a GCHP system (Dickie 2010), understanding how thermal properties of the subsurface affect the heat exchange process is paramount to the economic and thermodynamic optimization of the systems.

A variety of geological and thermal factors can affect the efficiency of a GCHP system. These properties include the thermal conductivities and volumetric heat capacities of the site soil and

rock. Since the presence of fluids in soil and rock pore space also affects the apparent bulk thermal properties of the subsurface, porosity, pore-size distribution, and piezometric levels are important to assessments of site thermal properties. Additionally characteristic hydrogeology can supply or extract additional heat through advection if groundwater flow is present. Gehlin and Helström (2003) found the effect of advected heat through fractures and pore spaces to be significant; in their study, increasing the specific flow rate from $1x10^{-8}$ m/s to $2x10^{-7}$ m/s quadrupled the GHE's effective thermal conductivity. Undisturbed ground temperature can also be important, especially for imbalanced systems—those which extract more heat than they inject, or vice versa. Ground temperature can be thought of as a sink or reservoir for heat; in cases with high ground temperature, the reservoir is already quite full, so using it to dump more heat than is being extracted could lead to unsatisfactory performance. If the reservoir is "full" (i.e., has high temperature), the system may operate inefficiently or it may be unable to meet the load imposed by facility thermostats leading to increased indoor temperatures.

1.2 Distributed Thermal Property Estimation

Distributed thermal property estimation is a relatively new field of study, which began with the development of distributed thermal response tests (DTRTs), sometimes referred to as enhanced geothermal response tests (EGRTs), pioneered by Fujii et al. (2009) and Acuña et al. (2009). A wealth of information is available by measuring distributed heat fluxes and comparing them against geophysical borehole logs, laboratory tests, and models of subsurface heat transfer. The main use of this information is a record of true *in situ* interactions for an operating system. Distributed thermal data in an operating GCHP system require fewer assumptions about the nature of heat transfer in the subsurface when compared to laboratory experiments, modeling efforts, or even some other *in situ* tests like traditional thermal response tests (TRTs) or DTRTs.

Laboratory experiments like thermal conductivity measurements by divided bar or thermal probe cannot fully represent *in situ* conditions due to disturbance of the material being tested, the

inherent heterogeneity of earth materials, and the removal of *in situ* state conditions (e.g., effective stress, temperature, and saturation). The application of laboratory measurements to geothermal field assessments and GCHP system design is always preceded by recognition of how laboratory measurements cannot truly encompass true field conditions. A separate, but related, issue is the use of broad categorical bins for assessment of thermal properties at potential GCHP field sites. For example, siliciously cemented, low-porosity quartz arenite sandstone may have less in common with other “sandstones” than it does with quartzite, but the broad label of “sandstone” will identify it with lower conductivity averages which are not representative of its true properties. This issue was identified and addressed in Meyer (2013) and Walker et al. (2015) for Wisconsin rocks by using stratigraphic bins with more detail than broad rock types (e.g., Wolf River Batholith rather than “granite”, Jordan Formation rather than “sandstone”, and Prairie du Chien Group rather than dolomite). The task was well matched to the region’s spatially extensive, shallowly dipping sedimentary strata; GCHP systems designed for install in a large geographic area could benefit from each sample measured.

Modeling efforts for GHE heat transfer during typical GCHP operation would benefit from measured temperature profiles to match the modeled results. This comparison process would validate modeling assumptions such as thermal properties, model geometry, boundary conditions, time steps, and initial conditions. This usage of DTS in GHEs has already been advanced to some extent by Beier et al. (2012) and Acuña (2013) as a means of better interpreting TRTs. However, at the time of writing, there are no known cases utilizing permanently-installed DTS in a normally functioning GCHP system from which modeling of such systems might be validated.

DTRTs utilize DTS to measure profiles of temperature in GHE pipes during TRTs. TRTs were developed concurrently in the theses of Austin (1995) and Gehlin (1996). While they took different approaches in the assembly of their respective TRT devices, both publications were

based on the premise of injecting heat at a constant, specified rate through a GHE to determine the average effective thermal properties of the rock mass surrounding the borehole and within the borehole itself (e.g., effective thermal conductivity and thermal borehole resistance). The aforementioned work by Fujii et al. (2009), Acuña et al. (2009), Beier et al. (2012), and Acuña (2013) all represent efforts to improve TRTs by breaking down the “effective” thermal properties of the GHE into distributed thermal properties at known depths.

Chapter 2: Background

Both Chapter 3 and Chapter 4 have their own introductions and backgrounds designed to act as standalone documents or journal articles. Therefore, there is little need to restate that material in this background. However, the thesis format provides an opportunity to provide a more extensive background on DTS, which heretofore has not been extensively used as a measurement technique in research carried out in the UW-Madison Geological Engineering Program. That said, work performed within Civil and Environmental Engineering's Water Resources Engineering and Science Program has comprehensively used DTS to monitor soil moisture, and collaborative efforts between the Department of Geoscience and Wisconsin Geological and Natural History Survey hydrogeology groups has used DTS to characterize fluid flow in boreholes. Specifically, the work in Striegl (2011), Striegl and Loheide (2012), Sourbeer (2013), Bahr et al. (2011), and Leaf et al. (2012) are recognized.

2.1 DTS Introduction

DTS is a measuring technique that utilizes fiber-optic cable to measure temperature along continuous profiles. The application of this technology has rapidly expanded in both industry and academia due to inherent advantages over networks of conventional temperature-logging sensors (e.g., thermocouples, thermistors, and other temperature detectors) (Lee 2003). Fiber-optic sensing systems generally function by shooting laser light through an optical fiber and analyzing backscatter of this light as it relates to differing physical conditions. A series of different fiber-optic sensing techniques are used to measure distributed strain, pressure, electrical current, and voltage (Lee 2003), in addition to this work's focus on distributed temperature. Fiber-optic sensors can be divided into groups based on the principle of their property measurement (Rayleigh, Raman, and Brillouin scattering), forward or backscatter measurement, reflectometry used (time domain vs. frequency domain), and measurement

distribution (point, distributed, or quasi-distributed measurements) (Grattan and Sun 2000). DTS as used in this work is a time-domain Raman backscatter method for fully distributed measurements.

2.2 History of Raman-based DTS Development and Application

DTS was pioneered in the early and mid-1980s by researchers in the United Kingdom who noticed the relative temperature sensitivity of the anti-Stokes band of Raman backscatter, with respect to Stokes or Rayleigh backscatter (Hartog 1983; Hartog et al. 1985; Dakin et al. 1985). The development of many DTS devices was based on earlier work by Barnoski and Jensen (1976) to develop optical time domain reflectometry (OTDR). Early field application efforts were stymied by insufficient power in the optical signal, which limited the usable length of fiber sensors to a few hundred meters (Kurashima et al. 1990). Hurtig et al. (1994) was one of the first applications of DTS for down-hole temperature logging, though at that time, measurements were still limited to relatively shallow boreholes. However, continued development of lasers and sensors for Raman-based OTDR on multimode cables led to examples of much deeper DTS installations reaching over 600 m (Hurtig et al. 1997) and finer spatial and temporal resolutions (Großwig et al. 1996). Farahani and Gogolla (1999) detailed mechanisms for the generation of Raman backscatter in multimode fibers and developed optical frequency domain reflectometry (OFDR) for DTS based on original work by Ghafoori-Shiraz and Okoshi (1986).

By the mid-2000s, research and commercial uses of DTS proliferated quite rapidly, providing more earth sciences applications and better tools for managing DTS. Since then, many sub-fields of earth science have taken advantage of DTS for applications as diverse as hydrologic monitoring (Lowry et al. 2007; Selker et al. 2006a; Selker et al. 2006b), fluid flow in boreholes (Leaf et al. 2012), soil moisture monitoring (e.g., Steele-Dunne et al. 2010, Sayde et al. 2010, Streigl and Loheide 2012), ground surface temperature reconstructions (Freifeld et al. 2008), hydraulic and thermal tomography (Oberdorfer et al. 2013), and effective subsurface thermal

properties (Fujii et al. 2009; Acuña et al. 2009; Beier et al. 2012). The main focus of this thesis' work is mostly in line with the last cited examples insofar as their use of DTS in ground heat exchangers (GHE). However, the work, which is mainly presented in Chapter 4 and Appendix 1, is not a temporary test as in those publications' enhanced or distributed thermal response tests (EGRT and DTRT, respectively); instead, monitoring is, and will be, continuous in long-term deployments, which has more in common with the former examples in soil moisture monitoring.

In addition to the aforementioned academic uses of DTS, Raman-based DTS has been used in industrial applications over the past decade, providing useful information on the capabilities of DTS (Ukil et al. 2012). The power generation and transmission industry has been interested in DTS as a method of monitoring temperatures along stretches of power cables, especially those buried underground. Yilmaz and Karlik (2006) investigated the use of DTS in buried electrical distribution and collector cables, finding it to be effective in identifying "hotspots," which would be otherwise difficult to discern with conventional monitoring techniques. Case studies on power cable monitoring with DTS, such as Schmale et al. (2011), are now widely available as DTS applications companies have formed and begun retailing their services. DTS is also becoming a common tool for the oil and natural gas exploration and extraction industry as many reservoir features can be identified with temperature profiles (Smolen and Spek 2003).

2.3 Raman DTS Premise

DTS systems utilize infrared light confined within glass optical fiber through total internal reflection, usually by using fiber core and cladding of different indices of refraction (Tyler et al. 2009). Physical conditions of interest (e.g., temperature and strain) are matched to positions along the optical fiber by the travel time of the reflected light. For temperature measurements, the light segment of interest to the interrogator equipment is the Raman backscatter. Raman backscatter is inelastic—backscattered waves are shifted to either higher or lower wavelengths than the incident waves (Selker et al. 2006a). The higher-wavelength component of the

inelastically scattered waves is referred to as the Stokes component, whereas the lower-wavelength (higher frequency) component is the anti-Stokes component (Figure 1) (Suárez et al. 2011). Of all backscatter spectra, anti-Stokes Raman backscatter is, by far, the most temperature-dependent. As a result, the ratio of anti-Stokes intensity to Stokes intensity at given locations in the fiber can be related to the fiber's temperature through calibration processes, which will be described further in Section 2.4.

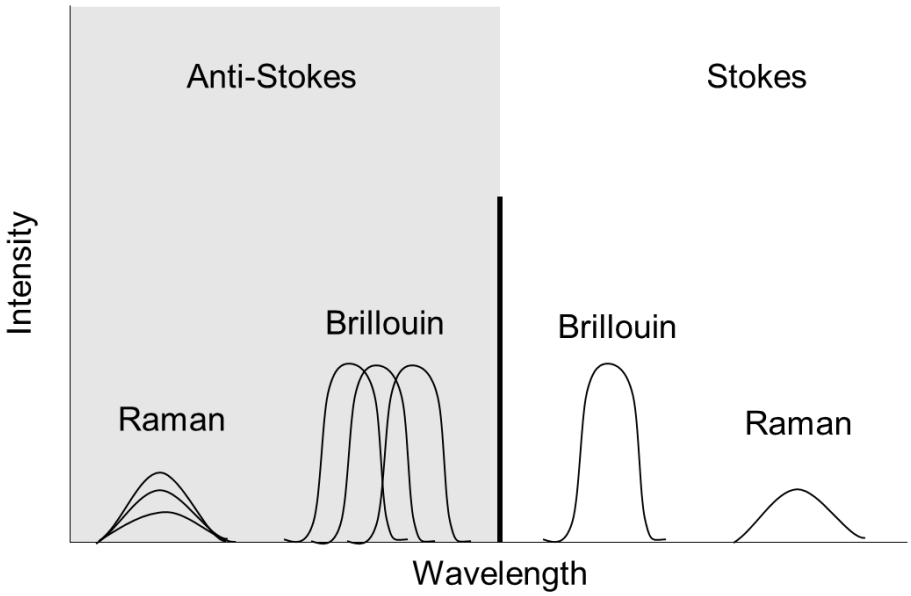

Figure 1: Distribution of backscatter intensity from incident light represented by the centerline. Multiple intensity and wavelength distributions for the anti-Stokes backscatter represent the temperature dependence of anti-Stokes Raman intensity and Brillouin wavelength, respectively. Figure developed from work in Suárez et al. (2011b).

The capability of a given DTS system to make accurate measurements depends on the quality of cable, splices, connectors, calibration, integration domain, and interrogator used. These components are chosen to ensure that a strong anti-Stokes to Stokes ratio is available to calculate temperatures along the fiber with the least amount of uncertainty. For a given pulse of laser light, only a very small component of that light is scattered back toward the laser source. Of this scattered light, an even smaller component falls into the Raman spectra as the vast majority is elastically scattered as Rayleigh waves. According to Farahani and Gogolla (1999),

the capture coefficient for Raman backscatter in multimode fiber is on the order of 10^{-10} m^{-1}, representing how much light is directed back at the source per meter. These already sparse signals are further attenuated naturally as they travel through the fiber, typically at a rate of 1 to 1.5 dB km^{-1} (Sensornet). Any splices or connectors between separate fiber segments add step losses to the attenuation along the continuous fiber. These step losses can affect both components of the Raman backscatter equally, which causes lower precision in the measurements due to the lowered signal strength. They can also differentially attenuate the anti-Stokes and Stokes signals through the step loss, a process that lowers measurement accuracy by biasing the temperature calculations.

For these reasons, components of the typical DTS system are chosen to maximize the return of raw data. Raman-based DTS systems usually utilize multimode cable, which allows more optical power to be applied to the fiber than single-mode cables typically used in long-distance communication (Sensornet). Cables are typically spliced using fusion splices, which tend to have lower losses than mechanical splices, and angle-polished connectors (APC) are used rather than other polishing types to keep connection losses low (Sensornet). Furthermore, present-day field applications use specific laser wavelengths, which have been shown to produce low signal attenuation (Yilmaz and Karlik 2006)—near infrared wavelengths (700 nm – 1400 nm) are nearly always used, and 1064 nm is common for use in multimode cables for some brands of DTS systems such as those by Sensornet Ltd. (Hertfordshire, UK) and Silixa Ltd. (Hertfordshire, UK). Other strategies to obtain the greatest amount of usable signal include decreasing temporal and spatial resolution for a greater sample of backscatter. By increasing the integration time for a measurement (i.e., decreasing temporal resolution), more backscatter will be available to inform the calculation of temperature values. The same is true for increasing the sampling distance; more signal backscatter is received for each temperature calculation.

Finally, more powerful lasers and sampling equipment will also decrease the uncertainty in DTS measurements, which is, mostly but not entirely, a function of the DTS interrogator cost.

2.3 DTS Network Considerations

The design of a data collection network utilizing DTS must consider the limitations of the hardware chosen, the measurement repeatability, and the temperature accuracy. Different DTS models have inherently different spatial sample distances and spatial resolutions. This is mainly due to differences in hardware like the lasers and receivers employed. Increasing spatial resolution (e.g., 2 m to 0.25 m) requires substantial investment in higher-cost hardware. For the experimental setup, tradeoffs exist between the accuracy of the system at long distances (> 10 km), degree of calibration required, and acquisition time. In addition to deciding how to balance the aforementioned tradeoffs, users have choices for cable configuration: single-ended, double-ended, and/or duplexed cables.

Single-ended setups are the simplest from the standpoint that they have only one connection to the interrogator, but they are limited in their ability to calibrate for certain forms of differential attenuation (Hausner et al. 2011; van de Giesen et al. 2012). If desired, a single-ended cable would only have to travel away from the interrogator, rather than completing a loop. Double-ended measurements can better calibrate for differential attenuation between the Stokes and anti-Stokes components, but they require two interrogator channels for each fiber. This is potentially the largest cost associated with double-ended measurements at a site with many DTS fibers; increasing the number of required connectors may necessitate additional equipment in the form of multiplexers or additional interrogators. Since the fiber must connect to the interrogator twice, the double-ended configuration requires twice as much fiber as a single-ended configuration to reach the same area(s) of interest, which could also become a cost consideration.

Duplexing can add a form of redundancy to both single and double-ended configuration by having the cable pass through the same place twice. Ideally, the two measurements will be nearly identical if proper calibration was performed. Furthermore, a given section of cable will pass through the same calibration bath twice with a duplexed configuration: once when leaving the interrogator, and once when returning. This simplifies calibration since only one bath needs to be maintained for two calibration sections, and the user can be certain the temperature of those sections are identical (if the bath is properly mixed). A final method for reducing uncertainty in calculated distributed temperatures is the process of wrapping fibers around cylinders for even greater spatial resolution and redundancy, especially when used with a double-ended and/or duplexed setup (Suárez et al. 2011).

For many applications, users must balance the need for high-frequency measurements (e.g., 30 s per measurement) and high-precision measurements. The relative scarcity of the anti-Stokes Raman signal (discussed in depth in Section 2.4) means that the error in a given measurement is highly dependent on averaging time and averaging spatial length (Sensornet). Many sources (e.g., Farahani and Gogolla (1999), Sensornet, Tyler et al. (2009), and Hausner et al. (2011)) state that error is a function of the inverse of the square root of both the spatial interval and temporal interval used for averaging due to the central limit theorem. As such, users of DTS systems must be aware of the systems' limitations in applications where high temporal and spatial resolutions are demanded, along with low temperature error. Beyond the limitations of the physics of the Raman scattering phenomenon, the limitations of the instruments themselves must be considered. Even if requirements for temperature precision are relaxed, the sensitivity of the sensors within the interrogator have their own limits for spatial and temporal resolution, related to how quickly the interrogator can resolve and process individual backscatter pulses (Sensornet). For example, the Sentinel DTS system by Sensornet Ltd. can resolve temperature to < 0.1 °C in a 60-s integration at 4 km. The Halo DTS system, on the other hand, also by

Sensornet, can attain temperature resolution of < 0.25 °C in a 60-s integration at 4 km. These systems obey the increase in resolution with the square root of integration time mentioned above, so both marks would improve if scenarios allowed for it (e.g., in Appendix 1).

2.4 DTS Calibration

Deploying a DTS system, whether comprised of a single fiber or dozens of fibers spliced into a network, requires a thoughtful instrumentation plan, as introduced in the Section 2.3. The calibration process is an exceedingly important part of these plans. It determines the location and number of calibration baths required, and justifies their existence in the first place. As a result, no two installations will be exactly identical, and users must specifically calibrate their own DTS for each deployment (i.e., DTS cannot be “precalibrated” – at least for highly accurate measurements).

Efforts from the Center for Transformative Environmental Monitoring Programs (CTEMPS) have drastically improved awareness of various calibration strategies within the earth sciences field with two papers of note: Hausner et al. (2011) for single-ended measurements and van de Giesen et al. (2012) for double-ended measurements. To avoid treading on ground previously covered, this section will only briefly explain and summarize some of the main components of temperature calculation and calibration in DTS. Readers with more interest on the topic of calibration should certainly read the two aforementioned papers. Those who want a deeper understanding of the derivation of the equations employed both here and in those papers are directed toward the work summarized in the supplemental material of Hausner et al. (2011) and Yilmaz and Karlik (2006), which are themselves based on the foundational work of Farahani and Gogolla (1999).

Most of the common derivations for temperature in a DTS system result in Equation 1, with three constants (γ, C, and $\Delta\alpha$), location along the fiber (z), and the relative intensity of the

Stokes and anti-Stokes backscatter (P_S/P_{aS}). The constants and the relative intensity of the backscatter are dependent on location along the fiber and time, to varying degrees.

$$T(z) = \frac{\gamma}{\ln\left(\frac{P_S}{P_{aS}}\right) + C - \Delta\alpha z} \quad (1)$$

The constant γ is a physical constant based on the Boltzmann constant (k_B) and the shift in energy between the incident laser light and the backscattered Raman light (ΔE) (Equation 2). Since the Boltzmann constant has the same dimension as entropy (J K^{-1}), γ has units of temperature (K).

$$\gamma = \frac{\Delta E}{k_B} \quad (2)$$

Typical values for γ are in the range of 480 K to 490 K (van de Giesen et al. 2012). The value is theoretically a constant, but, in practical application, the effective value needed for a DTS interrogator to obtain reliable temperature measurements can differ from the theoretical value. This is typically due to very slight variations in the construction of the DTS hardware. Even within the same model and manufacturer, differences may be present due to differences in the efficiencies of the units' photon receptors (Farahani and Gogolla 1999).

ΔE can be understood as the shift in frequency between incident (or Rayleigh) and backscattered light (e.g., Raman). This is because energy (E) and frequency (ν) are proportional to one another in the Planck-Einstein relation (Equation 3), which relates the two via Planck's constant (h) in the photon-based, quantum view of light, fundamentally different from Maxwell's wave-based understanding of light. For a given molecule of glass within a fiber at a certain energetic state, a photon generated by the infrared laser may impact and excite the molecule to a "prohibited" state (Farahani and Gogolla 1999). At this state, the molecule must release energy in the form of a photon. If the energy released by the molecule is exactly the same as the amount of "excitation" received by the molecule, then the photon it generates will have the

same energy as the incident photon (Rayleigh scattering). If the energy released is less than the amount of excitation received (the molecule increases its energy state) then a Raman Stokes signal results (lower frequency and higher wavelength than incident light). In the opposite case, in which more energy is released than excitation received, Raman anti-Stokes photons are released. The exact change in energy states is dependent on the molecules themselves, making *γ* a function of the type of glass used in the core of the fiber in a given setup.

$$E = hv \tag{3}$$

While the degree to which the frequency of scattered light shifts is based on molecular properties, the probability that one of the frequency changes occurs (Raman scattering) is based on Bose-Einstein statistics. This theory describes the initial energy state occupied by molecules in the fiber. The resulting equations (Equation 4 and Equation 5) assign a much lower probability to anti-Stokes Raman scattering, when compared to Stokes scattering. The temperature-dependence of this probability distribution is what gives rise to the derivation of a temperature equation for DTS like in Equation 1, shown in detail by Hausner et al. (2011) and Farahani and Gogolla (1999).

$$\mathcal{P}_S = \frac{1}{\left[1-\exp\left(-\Delta E/k_B T\right)\right]} \tag{4}$$

$$\mathcal{P}_{aS} = \frac{\left[\exp\left(-\Delta E/k_B T\right)\right]}{\left[1-\exp\left(-\Delta E/k_B T\right)\right]} \tag{5}$$

The constant *Δα* represents differential attenuation of the Stokes and anti-Stokes signals within the cable. As backscattered light travels toward the interrogator, it is attenuated, just like light in nearly any media. This attenuation is an exponential function of distance and the attenuation factor, as mandated by Beer's Law (Equation 6), which describes the ratio of the transmitted power of light to incident power.

$$\frac{P}{P_0} = \exp(-\alpha z) \quad (6)$$

The two spectrums of interest are attenuated at different rates due to the wavelength difference between them. The differential attenuation constant is mostly a function of the fiber employed in the measurements. No two fibers are exactly alike, so $\Delta\alpha$ should be calculated for each DTS deployment and for each separate fiber of interest within a single DTS deployment. While using the Halo DTS system in the studies for this thesis, $\Delta\alpha$ was typically on the order of 8×10^{-5} m^{-1} for a variety of multimode cables. As can be surmised by the units of the differential attenuation constant (m^{-1}) and its coupling with distance, z, the effect of differential attenuation is to adjust the dimensionless natural logarithm of the relative intensity fraction (P_S/P_{aS}) as a function of distance.

The constant C essentially accounts for calibration error that cannot be assigned to either differential attenuation or slight perturbations in the γ value. In the derivation of the DTS equation by Farahani and Gogolla (1999), C encompasses two factors. The first is a wavelength-based approximation of the relative capture coefficients for the anti-Stokes and Stokes signals. That factor, along with the Bose-Einstein probability function, accounts for differences in the amount of backscattered signal directed at the interrogator's photon receptors. The second factor is the relative efficiencies of the interrogator's photon receptors, which accounts for differences in how it receives the Stokes signal versus the anti-Stokes signal.

Determining each of the aforementioned parameters is the primary focus of calibrating a DTS system. Acquiring accurate temperature measurements for environmental applications typically requires a more rigorous approach to calibration than those offered as defaults by DTS manufacturers (Hausner et al. 2011). The approach advocated by Hausner et al. (2011) is to instead employ at least three, but preferably four calibration sections for each fiber of interest. This allows the researchers employing the system to solve a system of equations for the three

unknown parameters (γ, C, and $\Delta\alpha$) by post-processing the raw Stokes and anti-Stokes intensities. A fourth calibration section, if acquired, could then be used to validate the calibration.

A Matlab script promulgated by CTEMPS has been used frequently by researchers to perform calibrations in the manner described above. However, post-processed DTS data in this thesis was produced by a different Matlab script that was developed internally. Like the script from CTEMPS, the script used in this thesis is based on the strategies presented in Hausner et al. (2011). The reasoning for developing the script was two-fold. First, writing code independently ensures full understanding of how the mathematical formulae are applied to processing. Second, an independently written code could be written for the specific aim of processing data from a unique DTS installation, such as the efforts presented in Appendix 1. The code described here is presented for inspection in Appendix 2. Future efforts will make additions to the code to automate the data processing, calibration, and retrieval process.

The work of this thesis does advance a few differences in the approach to solving for DTS calibration parameters. Primarily, the number of calibration sections above the minimum were accommodated in the code. This means that a least-squares solution could be calculated for what would now be an overdetermined system of equations. Such an approach has advantages when compared to only solving a system of three equations. Namely, the overdetermined approach would provide a greater sample of the fiber, so that the fiber's properties and those of the interrogator would be known with greater certainty.

An example of the result of post-processing raw fiber optic data is shown in Figure 2, which contains data from the sentry wells of Borefield #4 at Epic. While the meaning and implications of this data set are discussed more in Appendix 1, it is presented here to serve as an example of the differential between the results generated by the DTS interrogator's default calibration

and the post-processed calibration. The data was generated from a fiber embedded in conduit housed in trenches at a soil depth of 2 m and sent to the bottom of two boreholes before returning to the DTS interrogator. There are eight calibration sections: four at elevated temperatures (> 30 °C), and four in an ice bath reaching nearly 0 °C. The obvious difference between the default temperature data and the post-processed data is what appears to be a nearly uniform increase in temperature of about 3 °C across the profile. However, further inspection (Figure 3) shows that this is not quite the case. Alterations to the default calibrations were heavily influenced by differential attenuation, which can be seen in the slope of the temperature change in Figure 3. However, the differences between the default and post-processed temperature profiles also included different *C* values, as seen by the spikes in temperature change at the locations of the calibration baths in Figure 3. This is because adjustments in the denominator of Equation 1 (like changes to *C*) result in temperature changes that scale inversely with the natural logarithm of the relative Raman backscatter intensity (Figure 4). In other words, the effect of changing calibration parameters does not simply translate the profile upward or downward; the effect on the results is a function of the combination of the raw Raman signal and the *C* parameter.

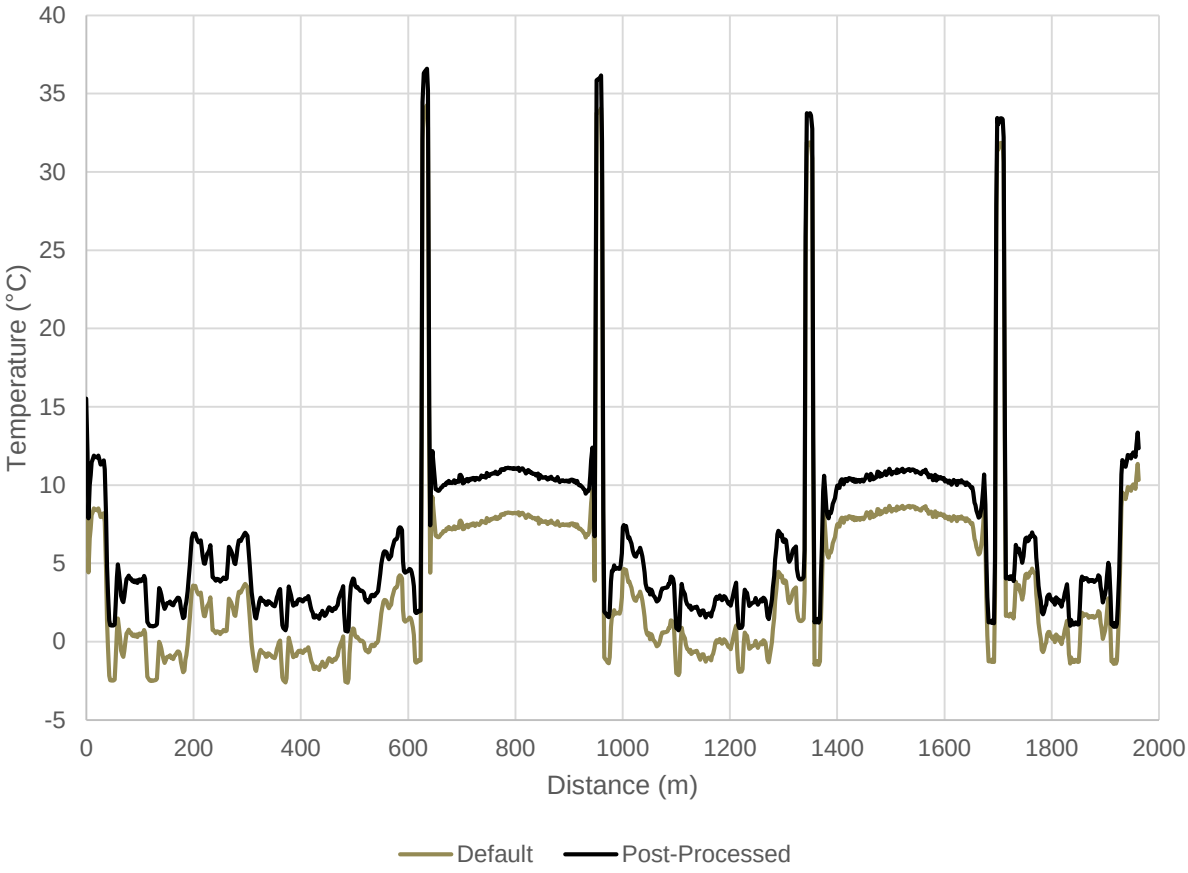

Figure 2: Example DTS profiles resulting from default calibration parameters and post-processed calibration. Data is from the sentry wells of Borefield #4, described in Appendix 1.

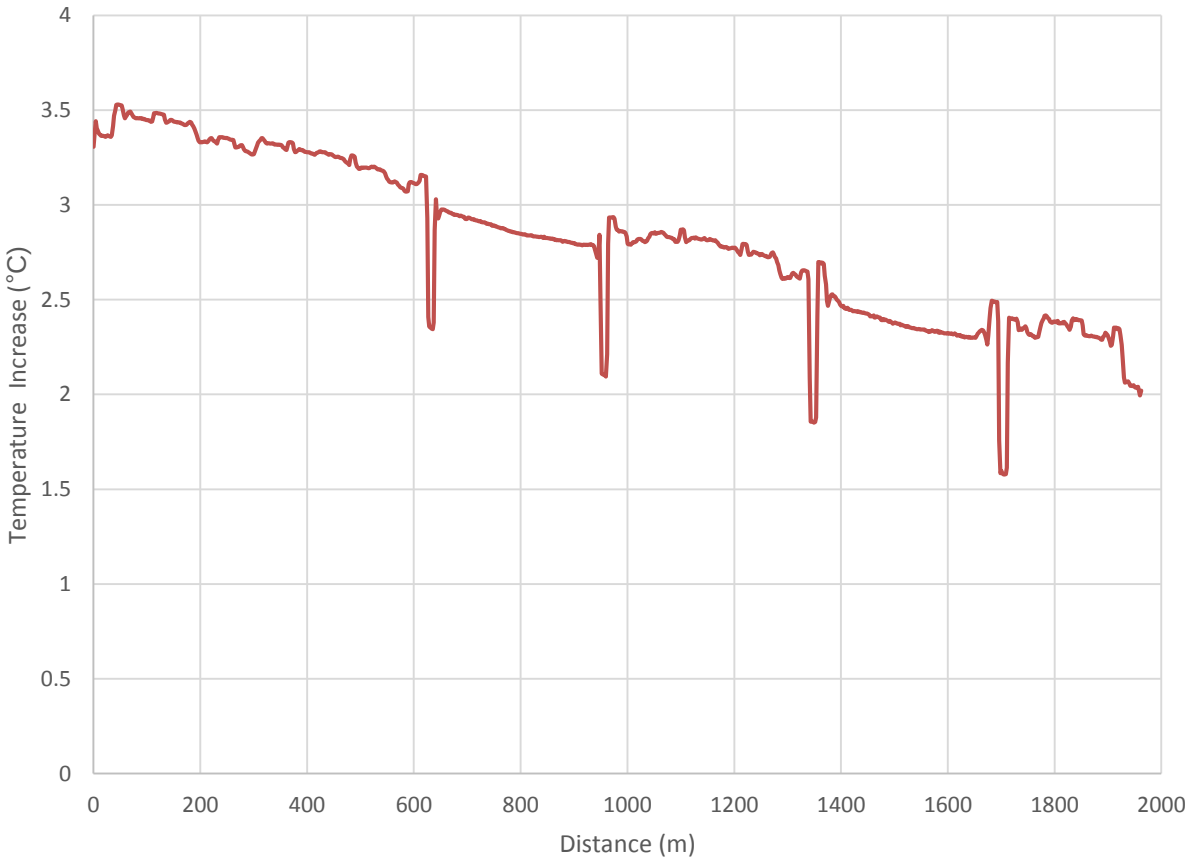

Figure 3: Temperature change between the default calibration in Figure 1 and the post-processed calibration in Figure 1.

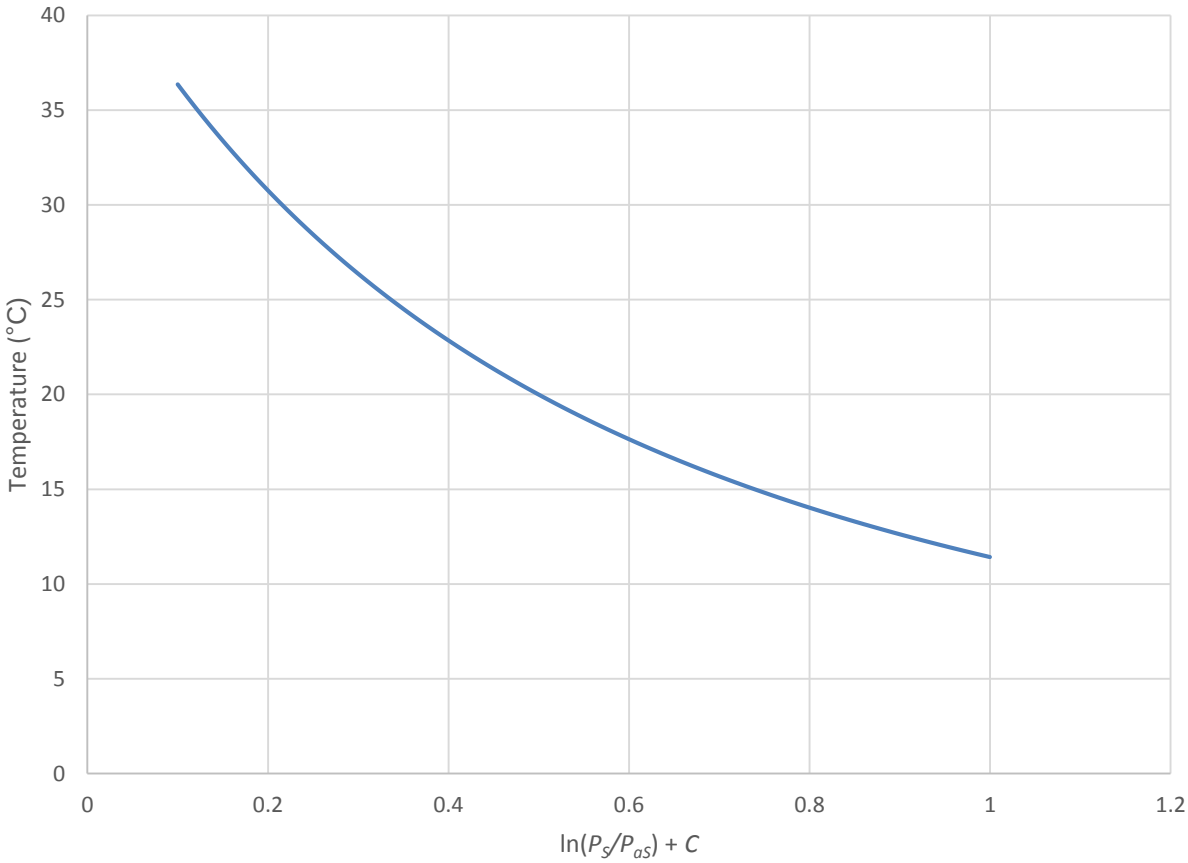

Figure 4: Effect of changing the denominator of Equation 1 on the resulting temperature for a γ of 485 K.

Chapter 3: Thermal Property Measurements of Stratigraphic Units with Modeled Implications for Expected Performance of Vertical Ground Source Heat Pumps

3.1 Introduction

The design of a geothermal exchange system is based on the extreme entering water temperature (EWT), heating and cooling load, and thermophysical properties of the soil and/or rock. The thermophysical properties are typically estimated from handbook values for residential systems due to the high cost of running a thermal response test (TRT) or thermal property tests (Dickie 2010). Due to the expense of TRTs, TRTs are rarely considered as a method of improving the accuracy of residential and small commercial system design. A TRT can be seen as an investment which is more cost-effective when its expense can be recouped by efficiency gains on large heat exchanger fields. These efficiency gains are due to the TRT's role as the standard *in situ* thermal property estimation tool for ground heat exchange fields (Witte 2013).

Residential systems account for the majority of installed GSHP capacity in North America (Lund et al. 2004). Properly sized heat exchange fields keep both the initial cost and operating cost of the system near their theoretical minimums. However, the use of measured thermal properties in a model to determine optimal field size is rarely performed – values of thermal properties from handbooks or rules of thumb are commonplace. Tables of thermal properties collected and synthesized from geology papers or books are generally organized as ranges of values for broadly defined lithologies (e.g. limestone, sandstone, clay, etc.). Even if a system designer considers thermal properties, the range of thermal conductivity available for specific rock types generally exceeds ±3 W m^{-1} K^{-1} (Clauser and Huenges 1995). In these cases, rules of thumb or conservative designs prevail.

Since the initial cost of a GSHP system is a significant decision point for a common residential customer, system sizing based on conservative input values (and thus higher upfront costs) might be unpalatable for the consumer. Although overestimating the site's effective thermal conductivity may initially placate the customers' demand for a cost-effective heating and cooling system, the affordability of a small heat exchange field may be short-lived; the true cost of an under-sized field may manifest itself as an extreme EWT, with inherent high operating costs. The potential outcomes may include an unhappy customer and a poor reflection on residential geothermal exchange systems in general.

One method of improving the utility of lab-measured thermal properties is to make measurements representative of specific lithofacies and stratigraphy from rock cores. Rock formations for a particular geographical area and lithofacies could be characterized for their thermophysical properties. System designers would then have accurate knowledge of the thermal interaction between the borehole heat exchangers (BHEs) and the formations that the BHEs intersect. Classification by formation and lithofacies rather than some general rock type allows for less error between laboratory-collected properties and *in situ* properties. For example, large differences may exist between a thermal conductivity value referenced in a GSHP design textbook for "limestone" and the *in situ* thermal conductivity of a particular limestone intersected by a borehole; these differences would stem from the unique lithofacies of the referenced and *in situ* limestones (i.e. mineralogy, presence of karst, chert nodules, grain content, mud content, etc.) (Clauser and Huenges 1995). Collection of the thermal properties of specific lithofacies will help designers gain better insight into the potential performance of installed systems, but these properties are still estimates, subject to variations, fractures, and hydraulic potential differences particular to a given site. Ultimately, a database of thermal properties is desired such that the public has access to information on the thermal properties of formations and their lithofacies for

a given region. For example, the Wisconsin Geological and Natural History Survey (WGNHS) will publicly disseminate the data collected in this study.

If a designer uses thermal conductivity values for a particular lithofacies, most of the remaining differences between rock core and *in situ* properties would then amount to the effects of *in situ* stresses, fluid flow, fracturing, and scale effects, which are not replicated in lab tests and rarely accounted for in system modeling. Among these differences, the most important for GSHP applications is likely fluid flow, which can be related to the presence of fractures (Gehlin and Hellström 2003). Gehlin and Hellström (2003) modeled the effect of fractures on ground heat exchangers, and found that even low specific flow rates could drastically alter the rate of heat transfer from the heat exchanger. Though potentially significant, fracture networks are difficult to identify in the field, and the distribution of hydraulic potential at a given site is, by definition, site-specific. This is related to the problem of scale in *ex situ* testing because a laboratory specimen can never fully capture the full fracture network of a site, nor can it capture site-specific heterogeneity in lithology, the degree of which is different by formation; some formations are "massive" and fine-grained such that a given laboratory sample is fairly representative, while others might have large cobbles in a fine-grained matrix, difficult to replicate at the lab-scale. The final difference consisting of effective stresses is important as it allows greater heat transfer at particle contacts within soil and rock than in low-stress conditions (Somerton 1992). Somerton (1992) states that increases in rock thermal conductivity due to stress increase is generally small, on the order of 2% for 7 MPa stress increase above 3.5 MPa in sandstones. However, the effect is significant between low-stress conditions and 3.5 MPa of effective stress.

We expect that data from laboratory measurements of thermal properties will provide a powerful and useful resource for installers of residential systems to make informed design decisions. Additionally, commercial and industrial installers would have another resource for subsurface thermal properties to supplement TRTs they may have conducted. We believe that high-quality

science and engineering conclusions and decisions stem from the informed use of multiple, independent lines of evidence, such as those from both *ex situ* and *in situ* testing. To be clear, *ex situ* thermal testing cannot replace the utility of *in situ* testing as represented by TRTs because only *in situ* testing includes the effect of effective stress, fracture networks, field-scale formational heterogeneity, and the presence of fluids. As a result, the uncertainty in applying the results of laboratory testing likely exceeds that outlined by Witte (2013) for TRTs (on the order of 5% to 15%). However in the absence of *in situ* testing results, laboratory testing of specific rock formations offers a next-best alternative, one that involves less uncertainty than loose design guidelines or generalized tables.

Liebel et al. (2010a) and Liebel et al. (2010b) investigated the difficulties of using samples from rock cores to replicate the utility of TRTs. The authors note that deviations between the rock core thermal properties and the effective thermal properties are magnified in wells which intersect many geological units. Liebel et al. (2010a) concluded that this was at least partially due to the use of a single sample to represent the thermal conductivity of the entire well, based on the formation outcropping at the surface. Liebel et al. (2010a) also found that laboratory measurements tended to produce lower thermal conductivity than the effective thermal conductivity measured in TRTs. Liebel (2012) explained this result from Liebel et al. (2010a) by noting the possibility for advective heat transfer from groundwater and 8% differences in thermal conductivity between water-saturated and dry samples according to Clauser and Huenges (1995). We seek to expand on work similar to that of Liebel et al. (2010a) and Liebel et al. (2010b) by estimating the thermal conductivity of a site with depth-weighted arithmetic average of all thermal properties for the geologic units intersected by the well. However, we expect laboratory measurements to continue to be a lower-bound estimation for effective site thermal conductivity as found in Liebel et al. (2010a). This estimation is an approximation of site

conductivity, which would be a place to start for installers and designers who do not have the budget for a TRT.

3.2 Materials and Laboratory Procedure

3.2.1 Rock Specimens

The majority of the rock specimens evaluated in this study were prepared from rock cores archived at the WGNHS geologic repository. The rock cores' corresponding coreholes are spread across the state, though the concentration of available cores and logs is greatest in areas with greater water-well drilling activities and mining exploration. Water-well drilling is most common in the southern two-thirds of the state, where most of the state's population resides and where agricultural activity is most intense. These demands correspond to the location of slightly dipping Paleozoic sedimentary strata, which are generally more hydraulically productive than the state's older formations. Outcrops in the northern third of the state are largely dominated by Precambrian intrusions, volcanics, and metamorphics, some bearing mineral deposits. Cores from both resources, water-well drilling and mining exploration, contribute to the knowledge base of lithologic and thermophysical properties across the state.

3.2.2 Thermal Conductivity and Specific Heat Measurement

A guarded-comparative-longitudinal heat flow apparatus was constructed following ASTM E1225 specifications (Figure 5); however, the heater guard was omitted in favor of additional insulation. Meyer (2013) found that the system performed more accurately when testing the glass-ceramic reference using better insulation and omitting the guard. The heater section and heat sink were constructed from Aluminum 6061. Aluminum 6061 was selected because it is easy to machine, is fairly inexpensive, and transfers heat well. The central column composing the heater section, reference materials, specimen, and stainless steel plug will be referred to as

the testing column. The aluminum plug was inserted in the space below the bottom reference material to minimize axial heat flow from the bottom of the column (Figure 5). Perlite was selected as the insulating material due to ease of use and low thermal conductivity of approximately 0.031 W m^{-1} K^{-1}. An 11.43-cm-diameter PVC pipe (0.19 W m^{-1} K^{-1}) was attached to the heat sink and used to contain the perlite insulation around the testing column.

To determine the thermal conductivity of the unsaturated rock specimens using the method outlined in ASTM E1225, a material with a known thermal conductivity, λ_M, was needed (ASTM 2009). ASTM E1225 recommends the use of a reference material with a thermal conductivity on the same order of magnitude as the specimen being tested. Based on an estimated range of thermal conductivity of 1 W m^{-1} K^{-1} to 8 W m^{-1} K^{-1} for the rock specimens, the reference material selected for this test setup was an Institute for Reference Materials and Measurements (IRMM) certified glass-ceramic (BCR-724). The temperature measurements taken across the testing column at the locations denoted by an X in Figure 5 allowed for the calculation of heat flux per unit area, q', through the reference materials using Fourier's Law:

$$q' = \lambda_M \frac{\Delta T_M}{\Delta Z_M} \tag{7}$$

where ΔT_M is the change in temperature across the reference material, and ΔZ_M is the change in height between the two temperature reading locations in the reference material. Knowing the heat flux through the reference materials, as well as the temperature change across the rock specimen allowed for the calculation of the thermal conductivity of the rock specimen, λ_S:

$$\lambda_S = \frac{(q'_T + q'_B)\Delta Z_S}{2\Delta T_S} \tag{8}$$

where q'_T is the heat flux across the top reference material in the testing column, q'_B is the heat flux across the bottom reference material in the testing column, ΔT_S is the change in

temperature across the specimen, and ΔZ_S is the change in height between the two temperature reading locations in the specimen.

To determine specific heat, calorimetry tests were conducted on each initially unsaturated specimen using a simple calorimeter consisting of a water-filled insulating cup surrounded by perlite in a 30 cm x 38 cm insulating box made from 3.81-cm-thick extruded polystyrene (XPS). An Omega Type T thermocouple was inserted into the water in the insulating calorimeter cup to monitor temperature. Tests were run with an initial rock specimen temperature of 333.15 K to match the temperature conditions of the thermal conductivity tests. The specimen was then inserted in the calorimeter, and temperature measurements in the calorimeter were made in 10 s intervals to determine when the calorimeter reached equilibrium with the sample. This equilibrium temperature of the calorimeter, T_{max}, is representative of the specimen's specific heat capacity (higher T_{max} indicates higher specimen heat capacity). After T_{max} is determined (highest temperature that the aluminum calorimeter experiences during the test), the specific heat of the specimen is calculated as

$$C_{ps} = \frac{m_{cal} * C_{pcal}(T_{max} - T_{min})}{m_s(T_s - T_{max})} \quad (9)$$

where C_{ps} is the specific heat of the specimen, C_{pcal} is the specific heat of an aluminum calibration sample, m_{cal} is the mass of the calibration sample and T_s is the initial temperature of the specimen. The amount of time the sample takes to heat the water in the calorimeter cup is reduced as the water infiltrates the initially unsaturated sample. This test was run for unsaturated rock specimens and is further detailed by Meyer (2013).

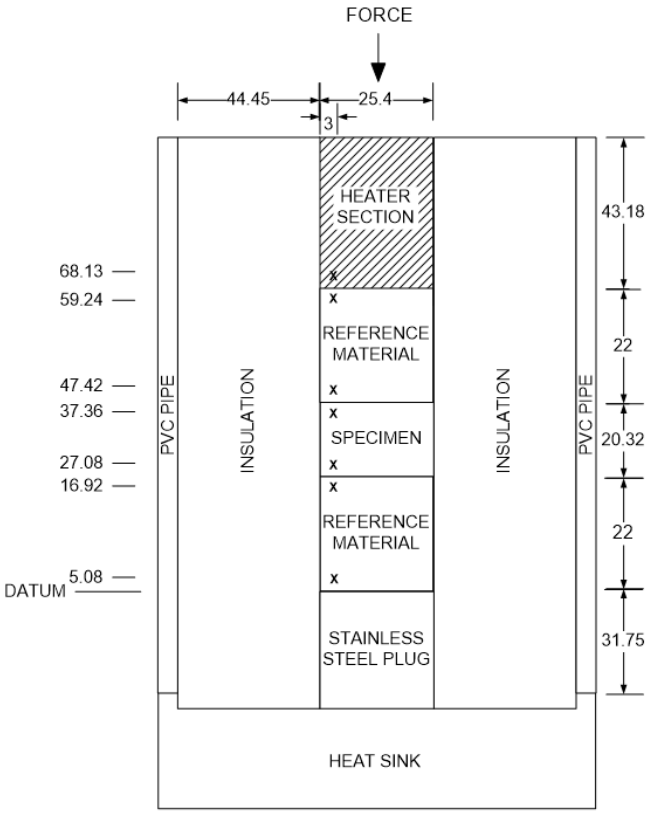

Figure 5: Cross-sectional diagram of the guarded-comparative-longitudinal heat flow apparatus; X's denote thermocouple locations, all dimensions in millimeters.

3.2.3 Uncertainty and Error Analysis

Meyer (2013) determined that the heat loss in the apparatus was negligible by calculating the heat flow through the two reference materials in the testing column. This verified that $q_{in} = q_{out}$ for the system. Additionally, an uncertainty analysis for the guarded-comparative-longitudinal heat flow apparatus was completed using the Kline McClintock second power relation (Figliola and Beasley 2000). This method is derived from a linear approximation of the Taylor series expansion for multivariable functions. Thus, for a linear equation $Z = X \times Y$, the uncertainty can be determined using the following:

$$U_Z = \sqrt{\left(\left(\frac{dZ}{dX}\right)U_X\right)^2 + \left(\left(\frac{dZ}{dY}\right)U_Y\right)^2} \quad (10)$$

where U_Z is the uncertainty in the variable Z, U_X is the uncertainty in the measurement X, and U_Y is the uncertainty in the measurement Y.

In the measurement of thermal conductivity, the total error propagates from errors associated with the measurement of length, area, heat transfer and temperature. Thus, all variables need to be considered when completing the error analysis. The equation used to determine the error in the thermal conductivity measurements (U_λ) can be represented by the equation below:

$$U_\lambda = \pm\sqrt{\left[\left(\frac{l}{A\Delta T}\right)(U_q)\right]^2 + \left[\left(\frac{q}{A\Delta T}\right)(U_l)\right]^2 + \left[\left(\frac{ql}{A^2\Delta T}\right)(U_a)\right]^2 + \left[\left(\frac{ql}{A\Delta T^2}\right)(U_{\Delta T})\right]^2} \quad (11)$$

where l is the specimen length, A is the cross sectional area of the specimen, ΔT is the change in temperature, q is the heat flow, U_l is the uncertainty in the length, U_a is the uncertainty in the cross sectional area, $U_{\Delta T}$ is the uncertainty in the change in temperature, and U_q is the uncertainty of the heat flow. U_l was determined using the following adaptation of the Taylor series expansion for multivariable functions:

$$U_l = \pm\sqrt{((l)(U_c))^2} \quad (12)$$

where U_c is the uncertainty in the calipers used to measure the length. U_a was found in a similar manner, but using the following equation:

$$U_a = \pm\sqrt{((0.5\pi d)(U_c))^2} \quad (13)$$

where d is the diameter of the specimen. The uncertainty in the heat flow U_q was found using:

$$U_q = \pm\,\lambda_{ins}\,A_s\,\frac{T_{spec}-T_{room}}{t_{ins}} \quad (14)$$

where λ_{ins} is the thermal conductivity of the insulation, A_s is the surface area exposed to the insulation, T_{spec} is the specimen temperature, T_{room} is the room temperature, and t_{ins} is the

thickness of the insulation. The uncertainty in the temperature change of the thermocouples was found with the following equation:

$$U_{\Delta T} = \pm\sqrt{6}U_T \quad (15)$$

where U_T is the uncertainty in the thermocouples. This statement is valid because U_T was the same for all 6 thermocouples used in the experimental setup.

The uncertainty analysis yielded error values between 0.04 W m^{-1} K^{-1} and 0.05 W m^{-1} K^{-1}. This corresponds to a relative error of < 3% for the experimental setup, which is much less than the observed experimental error and is indicative of sufficient system design.

Additionally, Meyer (2013) completed an experimental error analysis using simplified statistics for small numbers of observations. Each specimen was tested three times to ensure repeatability as well as to obtain a median and corresponding confidence interval for error (Dean and Dixon 1951). Using this method, the heat flow apparatus yielded an experimental error up to ± 0.70 W m-1 K-1. Error values reported in Table 2 represent the greater of the calculated uncertainty error or the experimental error.

3.3 Modeling

3.3.1 Mathematical Background for the Performance Model

Heat transfer from a U-pipe grouted in a vertical borehole was modeled with coupled analytical solutions for energy balance at the heat pump, heat transfer in fully-developed internal turbulent pipe flow within the U-pipe, and infinite transient line source theory on the subsurface's large scale. This model was developed as a means of realistically limiting the heat transfer rate to and from the ground loop; sole use of the infinite line source allows unrealistically rapid extraction and injection of energy due to simplification of the heat transfer process. The model starts by defining the amount of energy taken out of the ground heat exchange loop; this is the energy

required by the building during the heating season. The energy extraction from the loop affects heat exchange fluid temperatures according to the volumetric flow rate of the fluid. By considering the 1st Law of Thermodynamics (conservation of energy), there will be some change in mean fluid temperature, ΔT, if heat is transferred at rate Q. The amount of temperature drop is proportional to the mass flow rate of the fluid $\dot{m}$ (Incropera and DeWitt 2002).

$$\Delta T_{HP} = \frac{Q}{\dot{m}\, c_{p,fluid}} = \frac{Q}{\dot{V}\, \rho_{fluid}\, c_{p,fluid}} \tag{16}$$

On the scale of the larger subsurface, the system was modeled as an infinite line source with a constant heat flux across the length of the line. This model is assumed to be adequate to model a U-pipe heat exchanger on the larger scale because of the aspect ratio of the borehole; most conventional boreholes drilled for use as BHEs have a diameter of 10 cm to 15 cm and lengths of 30 m to 100 m. Approximations and exact solutions for transient line source solutions have been developed by Carslaw and Jaeger (1959) and Ingersoll and Zobel (1948) for heat transfer and Theis (1935) for fluid flow in porous media. From this theory, it follows that

$$T(t,r) = \frac{q}{4\pi\lambda}\mathrm{Ei}\left(\frac{r^2}{4\alpha t}\right) = \frac{q}{4\pi\lambda}\int_{\frac{r^2}{4\alpha t}}^{\infty}\frac{e^{-u}}{u}\,du \tag{17}$$

where Ei is the exponential integral function, q is the heat transfer rate per unit length of the line, λ is the thermal conductivity of the medium surrounding the line (the rock mass), α is the thermal diffusivity of the medium surrounding the line, r is the radial distance from the line, t is the time since the line began applying heat to the external medium, and T is the temperature change at the given radial distance, r, and time, t. Thermal diffusivity is defined

$$\alpha = \frac{\lambda}{\rho \cdot C_p} \tag{18}$$

that is, the ratio of thermal conductivity to the product of the density (ρ) of the subsurface and the specific heat (C_p).

The final model is an analytical solution for heat transfer given turbulent internal convective pipe flow under constant boundary temperature. This solution is based on the integration of Newton's Law of Cooling over a length of pipe undergoing exponentially decaying mean temperatures (Incropera and DeWitt 2002). Newton's Law of Cooling itself can be understood as a generalized form of heat transfer, stating that a body's rate of cooling by any mechanism (conduction, convection, or radiation) is proportional to the difference in temperature between itself and its surroundings. This integration of the law takes the form

$$q_{conv} = \overline{h_L}\, A_s\, \Delta T_{LM} \tag{19}$$

where q_{conv} is the convective heat transfer from the pipe, $\overline{h_L}$ is the mean heat transfer coefficient, A_s is the internal surface area of the pipe, and ΔT_{LM} is the log mean temperature difference (LMTD) between the pipe interior and the pipe's exterior surface. The LMTD, defined as

$$\Delta T_{LM} \equiv \frac{\Delta T_o - \Delta T_i}{\ln(\Delta T_o / \Delta T_i)} \tag{20}$$

and is used rather than the arithmetic mean temperature difference because mean temperature of the fluid decays exponentially as a function of axial distance from the pipe inlet. The expressions of temperature differences are relative to the pipe wall temperature, such that ΔT_o represents the difference in temperature between the fluid at the pipe's outlet, T_o, and the wall temperature, T_{wall}.

3.3.2 Ground Heat Exchanger Model

For a given model run, certain aspects of each of the three coupled systems – conservation of energy withdrawn at the heat pump, heat transfer to the rock layers through a line source approximation, and heat transfer in turbulent pipe flow – are known, and others are unknown.

The unknowns in one of the three systems are coupled to parameters in the other systems such that all unknowns can be solved for.

In the model of a heat pump's operation, heat transfer rate (Q), fluid mass flow rate ($\dot{m}$), and fluid specific heat ($C_{p,fluid}$) are known; the change in temperature across the heat pump, ΔT_{HP}, is the information that is sought (Equation 21). The change in temperature serves as an input for the other parts of the model so that the absolute temperatures entering and leaving the heat pump can later be determined (Figure 6).

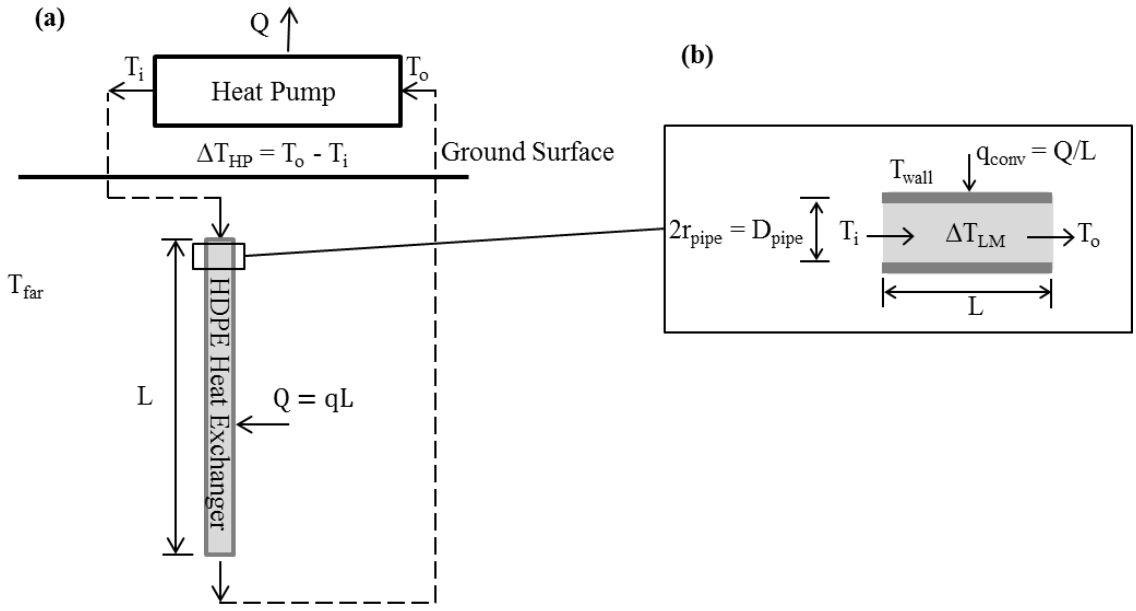

Figure 6: Graphical representation of where particular GSHP model parameters are located, where (a) describes the interaction between conservation of energy at the heat pump and the vertical line source of heat, and (b) shows how convective heat transfer was modeled at the pipe-scale

When applying the original line source formulation (Equation 21) to the heat exchanger problem, certain variables are specified to match the conditions of the problem. The transient infinite line source assumes that the heat transfer rate of the heat pump is evenly distributed along the line's length, L. The length of the line source is equivalent to the depth of the boreholes in the field. Variables α and λ represent thermophysical properties of the subsurface, r is defined to be

the distance between the center of a representative heat transfer pipe and its wall, r_{bh}. T_{wall} represents the temperature at the wall of the heat exchange pipe under influence from the heat transfer load. By taking the temperature at the radius of the borehole, the equations neglect the effect of borehole grout, which typically has thermal properties which differ from the surrounding rock mass. It is assumed that this simplification will have little effect due to the small thickness and volume of grout compared to the rock mass at large. However, there exist situations with large relative grout thickness, low grout conductivity, and short simulation times in which grout properties would heavily influence the thermal interaction between the GSHP and the surrounding rock. The aforementioned modifications to the analytical solution in Equation 21 are represented as

$$\Delta T(t, r_{bh}) = \frac{q}{4\pi\lambda}\mathrm{Ei}\left(\frac{{r_{bh}}^2}{4\alpha t}\right) \tag{21}$$

$$T_{wall} = T_{far} - \Delta T \tag{22}$$

where Ei is the exponential integral function and T_{far} is the reference temperature of the entire domain when $t = 0$. In practical terms, this temperature is a far-field temperature that represents the average temperature from the surface to the depths of the planned borehole heat exchangers, L. The pipe radius, subsurface thermal properties, far-field temperature, and line thermal load are all known quantities, so the wall temperature can be calculated and used as an input for the final coupled model: pipe heat transfer.

Since T_{wall} is known from the solution of the transient infinite line source problem and ΔT_{HP} is known from conservation of energy at the heat pump, T_o and T_i can be determined since there are two equations and two unknowns (Figure 6). First, the expression for ΔT_{HP}

$$\Delta T_{HP} = T_o - T_i \tag{23}$$

plainly relates T_o and T_i, which represent the EWT and LWT for the heat pump, respectively. The expression for ΔT_{LM} (Equation 24)

$$\Delta T_{LM} = \frac{(T_o - T_{wall}) - (T_i - T_{wall})}{\ln(\frac{T_o - T_{wall}}{T_i - T_{wall}})} \quad (24)$$

can be expanded. This can then be solved for T_i by substituting Equation 22 into Equation 24 and rearranging

$$T_i = \frac{(T_{wall} - \Delta T_{HP}) \cdot \exp(\frac{\Delta T_{HP}}{\Delta T_{LM}}) - T_{wall}}{\exp\left(\frac{\Delta T_{HP}}{\Delta T_{LM}}\right) - 1} \quad (25)$$

such that both EWT and LWT are known and can be used to evaluate the performance of the ground loop given input values governing convective heat transfer, total thermal load, and length of operation.

However, this solution still requires ΔT_{LM}, which can be determined through Newton's Law of Cooling (Equation 19) if $\overline{h_L}$ is known. Since the convective heat transfer rate is known over the heat exchanger pipe of known dimensions, the only remaining obstacle to solving for ΔT_{LM} is the heat transfer coefficient, $\overline{h_L}$. For convection in pipes of circular cross section, empirical correlations are available, which are generally dependent on a number of fluid flow characteristics. The flow regime must be characterized as either laminar or turbulent since the convection coefficient depends greatly on which of the regimes is active. Solving for ΔT_{LM}, Newton's Law of Cooling (Equation 19) can be arranged

$$\Delta T_{LM} = \frac{q_{conv}}{\overline{h_L} A_s} \quad (26)$$

in which the log mean temperature difference between the fluid and the wall is forced to accommodate the flow regime, pipe geometry, and required heat transfer rate. Since ground loops in GSHP systems are usually set up to attain turbulent flow with either water or anti-freeze

solutions, only the turbulent regime is considered here. The heat transfer coefficient is dependent on the Nusselt number of the pipe wall, Nu,

$$\overline{h_L} = \frac{Nu\,\lambda_{fluid}}{D_{pipe}} \tag{27}$$

which quantifies the ratio of convective heat transfer to conductive heat transfer. The Dittus-Boelter equation (Dittus and Boelter 1985)

$$Nu = 0.023Re^{0.8}Pr^{n} \tag{28}$$

is used here to calculate the heat transfer coefficient expected in the heat exchange pipe with the aforementioned assumptions. This empirical relationship assumes that the Reynolds number of the fluid is greater than 10,000 and the Prandtl number falls between 0.6 and 160. The Prandtl number is taken to the power, n, of 0.4 when the fluid is heated and to the power of 0.3 when being cooled. To use this correlation to calculate the heat transfer coefficient across the pipe wall, a rough estimate of the fluid temperature is used to approximate the hydraulic conductivity, density, viscosity, and specific heat capacity of the fluid. None of these values are constant, though the maximum temperature difference between points in the system (usually equal to ΔT_{HP}) should never be great enough in a GSHP application to significantly change any of the thermal properties for water or water-dominated heat exchange fluids (with a small percentage of glycol).

3.4 Methodology: Assessing BHE Performance under Varying Subsurface Thermal Properties

The expected performance of a hypothetical residential GSHP vertical ground loop in Southern Wisconsin was modeled under various subsurface thermal conditions. Southern Wisconsin was chosen as the idealized locale because its stratigraphy matches the thickest representative column of formations with rock cores obtained from the WGNHS for thermal testing. Southern

Wisconsin and the surrounding region are largely characterized by flat or slightly dipping Paleozoic sedimentary strata over undulating Precambrian igneous and metamorphic basement rocks (Dott and Attig 2004). Pleistocene-aged glacial deposits overlay the Paleozoic strata and outcropping Precambrian basement in some areas. Most of the strata are laterally continuous over hundreds of kilometers, making the identification of their thermal properties a worthwhile venture. Due to relatively small changes in the lithostratigraphy of each formation over great distances, their thermal properties were expected to be spatially consistent.

The idealized stratigraphic column at the site of the hypothetical ground loop contains sedimentary rock from the Early Ordovician to the Late Cambrian (472 to 501 Ma) overlain by recently deposited unconsolidated fine-grained glacial till. Thermally tested formations in this column include the Oneota formation of the Prairie du Chien group, the Jordan and St. Lawrence formations of the Trempealeau group, and the Lone Rock formation of the Tunnel City group. The Oneota formation is an oolitic, vuggy dolomite with chert deposits (Brown et al. 2013). The Oneota is the sole Ordovician formation, with the following formations deposited in the Late Cambrian. The Jordan formation is comprised of either fine or coarse quartz sandstone. Below the Jordan, the St. Lawrence formation ranges from silty dolomite to dolomitic siltstone (Brown et al. 2013). Finally, the Tunnel City group forms the basement of the column. This depositional group has distinct formations, which are less laterally continuous than many of the overlying formations. However, most of the Tunnel City's formations have poorly cemented medium sand as a large component of their lithology. Overlying the rocks of this strat column, alluvium, glacial till, or glaciofluvial deposits would be expected. However, no uniform characteristics could be expected for these unlithified deposits across large geographic areas, so the idealized column assumes a clay-dominated till of a given thickness with the realization that these overburden formations differ spatially and exert influence on the ground loop, typically

with low thermal conductivity values. The model assumes a 10-m-thick clay layer with a thermal conductivity of 1.5 W m^{-1} K^{-1}.

To represent the range of thermal conductivity expected for given rock formations, “handbook” values of thermal conductivity listed in Table 1 were used as model inputs to compare expected performance with measured values for the formations. These values are commonly cited by GSHP design materials as inputs for field design in the absence of TRT data (ASHRAE 2011). Importantly thermal conductivity values measured in apparatuses similar to that specified by ASTM 1225 are usually dry specimen values, which typically differ from *in situ* conditions in humid climates where ground loops often penetrate the local water table. The thermal conductivity values from literature were gathered from Kavanaugh et al. (1997), Clauser and Huenges (1995), Jaupart and Marschel (2011), and Touloukain et al. (1981). These values were matched to the general lithologic label assigned to each of the formations in the idealized column. The lowest value in each of the ranges in Table 1 was grouped with the others to define the *conservative* case. Likewise, the highest values were grouped for an *optimistic* case. Finally, the average of these two end-members was taken to be a *moderate* approach. Those three cases were then compared against a case with *measured* thermal conductivity values. The weighted thermal conductivity values for the conservative (lower literature values), optimistic (higher literature values), moderate (average literature values), and measured cores were 1.85, 4.37, 3.11, and 3.37 W m^{-1} K^{-1}, respectively. To provide a consistent baseline from which the effect of thermal conductivity can be compared, a constant specific heat capacity was assumed (1183 J kg^{-1} K^{-1}). The value was based on rock of 10% porosity averaging 850 J kg^{-1} K^{-1} for its solid component and 4180 J kg^{-1} $K^{-}1$ for its saturated component; vertical ground loops in humid climates typically contact saturated rock and soil for the majority of their length. The use of a single effective C_p value was also thought to be reasonable due to the small range of $C_{p,rock}$ and the small range of porosity.

The hypothetical ground loop has been specifically developed for a typical residential vertical GSHP installation, fulfilling heating and cooling requirements in a heating-dominated climate. The model assumes a heat pump operating at approximately 14 kW of heating capacity, a common heat pump size that might be reasonably expected to meet the heating requirements of some homes in the Upper Midwest. Real homes might have maximum heating demands greater or less than this, but 14 kW was chosen as a point of reference for field performance. The ground loop is a conventional closed-loop heat exchange field employing U-pipes in 15-cm-diameter boreholes separated by greater than 6 m. These pipes are HDPE tubes with a diameter of 2.54 cm and standard dimension ratio (SDR) of 11 (this indicates that the thickness of the pipe walls are 1/11 of the outside pipe diameter). The specifically modeled scenario assumes that this particular system had been sized by one of a number of commonly-applied contractor rules of thumb: 150 vertical feet for every ton of refrigeration (Lund 1990). Converting to SI units, this design is equivalent to 13 m of borehole depth per kW of heat transfer. To simulate the consequences of using this or similar design rules, the hypothetical system was designed solely with that rule as a consideration, rounding up to a pair of 100-m-deep wells (overdesigning by approximately 9 m per well). The wells penetrate 10 m of overburden clay, 35 m of Oneota Dolomite, 20 m of Jordan Sandstone, 4.5 m of St. Lawrence Dolomite, and 30.5 m of Tunnel City Sandstone (Figure 7). Each of the formation thicknesses are reasonable to expect in areas of the Upper Midwest (Brown et al. 2013). However, formation thicknesses are not constant spatially, and the same formations could cover more or less of a given 100 m well based on location.

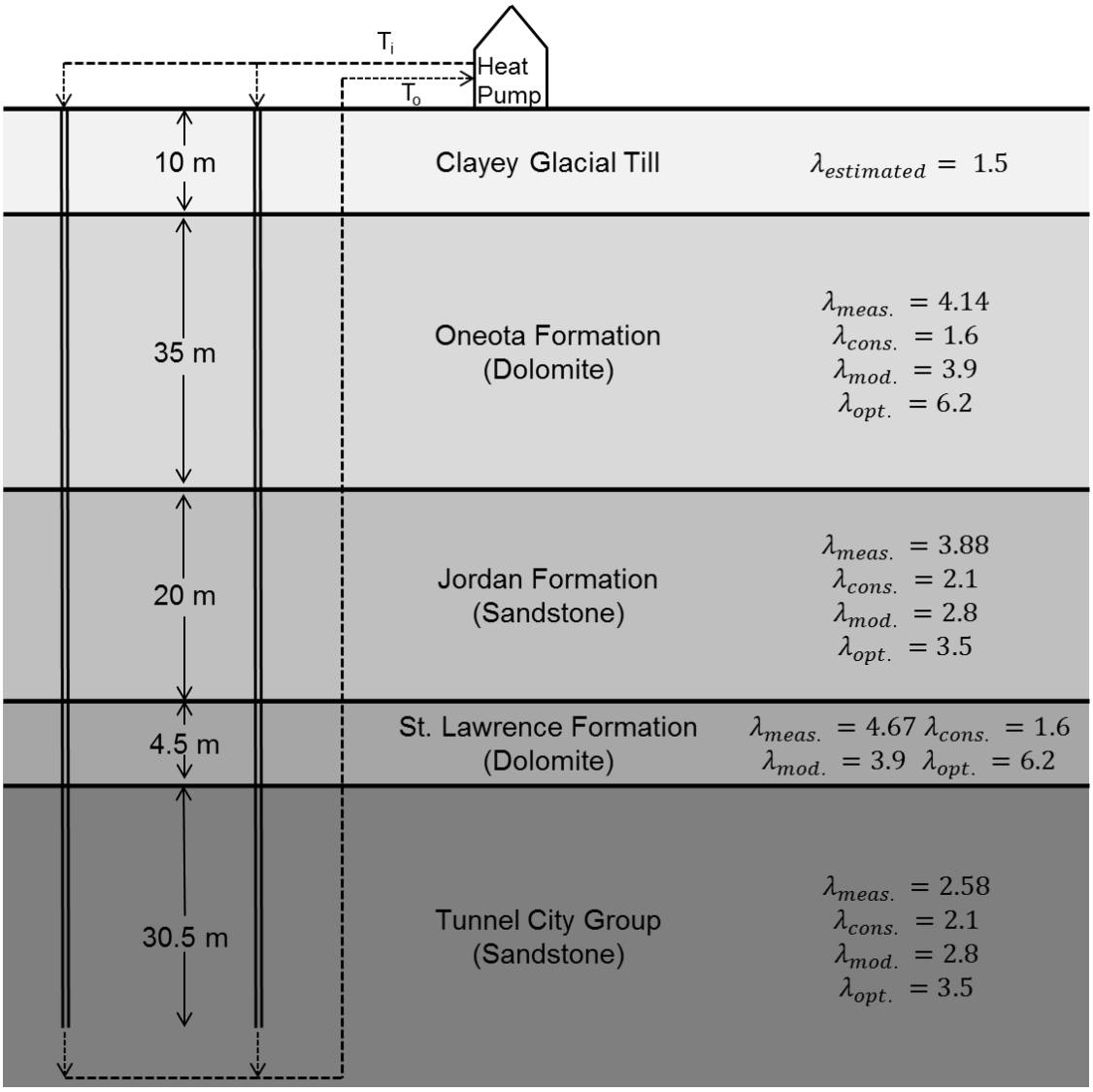

Figure 7: Approximation of the modeled subsurface stratigraphy in the four tested cases with the measured thermal conductivity of each formation along with the conservative, moderate, and optimistic handbook values

Performance of the hypothetical system was measured by the change in the heat pump's EWT over time with the system's max design load. Though this is not necessarily how installed heat pumps will operate for extended periods of time, the design approach provides a useful, consistent metric. The EWT can be expressed as a COP given the manufacturer specifications of a particular heat pump. Additionally, EWT under full thermal load demonstrates system performance in extreme conditions, arguably when performance is most critical. Importantly, this

case's design load of 14 kW has been defined by the model as a measure of heat extraction from the ground loop's heat exchange fluid; the actual heat provided to the home would likely be greater than the heat extraction as the compressor associated with the heat pump adds thermal energy to the system in the exchange process. The flow rate of the ground loop exchange fluid past the heat pump is set at 34 L/min, a common flow rate specified by manufacturers for 14-kW systems. While the fluid will flow past the heat pump at a rate of 34 L/min, the flow rate in the loops will be different if they are in a parallel circuit. Parallel circuits offer the advantage of lower head loss versus series circuits, though series loops have lower short-circuit heat transfer losses. Horizontal runs to the boreholes are assumed to be short, such that all heat transfer can be approximated to occur in the vertical portion of the U-loop. Though not necessarily the case for all heating-dominated systems, this model assumed the use of pure water as a heat exchange fluid. Again, this decision was made so that the results could be used as a benchmark for the performance of systems using any number of anti-freeze solutes or concentrations. The initial, or “far-field,” subsurface temperature is assumed to be a uniform 10 ºC, which is a reasonable value given shallow borehole depths, the low thermal gradient present in Wisconsin (Blackwell et al. 2007), and fairly small lateral changes in subsurface temperature. Unpublished data collected by WGNHS confirms that the majority of groundwater in the state within the upper 300 m of the subsurface is in the range of 9 °C to 12 °C.

Certain model limitations exist as a result of making the loop geometry conform to the constraints of the chosen models. However, the inputs to the model succeed in matching the assumptions required for the models’ empirical correlations with a Prandtl number of 10.5, a Reynolds number of about 10,000, and an aspect ratio of 4,000. To use the transient line source, thermal conductivity values were weighted by their thicknesses before being averaged over the length of one of the wells. This allows the line source’s homogeneous medium requirement (Equation 17) to be met, though it is only an approximation of the true combined

effect on the heat pump well. Additionally, when coupling the pipe heat transfer model to the transient line source, the heat extraction rate is averaged along the line's length to match its assumption of constant power per unit length. Though this demand conflicts with the premise of using a log mean temperature difference (Equation 20), the constraint was expected to still arrive at reasonable values given the averaged nature of the model.

3.5 Results and Analysis

3.5.1 Thermophysical Properties at the Modeled Site

Thermal properties of formations across the state were measured and compared to "handbook" values as shown in Table 1. A visual representation of these values with respect to their range can be found in Fig 4. For the most part, the laboratory-tested rocks fall within the established ranges set by Kavanaugh et al. (1997), Clauser and Huenges (1995) Jaupart and Marschel (2011) and Touloukain et al. (1981). Paying particular attention to the thermal conductivity values used in the model, the two dolomite formations and the sandstone of the Tunnel City Group fall neatly into the range reported by the authors of the referenced works. Conversely, the Jordan Sandstone stretched the given range of conductivity for sandstones. Additionally, the Jordan Formation had a greater sampling than any of the other formations. Two of the Jordan Formation's samples were from the same borehole, but at different depths. Though they are separated by 1.5 m, the two samples are from separate members of the Jordan Formations, the Van Oser and Norwalk members (coarse and fine-grained members, respectively). However, it should be noted that the 0.52 W m^{-1} K^{-1} difference in the samples is within the error bounds of the deeper sample. The sample from the separate borehole matches well with the deeper of the two samples from the same borehole in both thermal and physical properties, differing by less than 1% in thermal conductivity and by less than 5% in density. This demonstrated the measurements' repeatability, or lack thereof, within a formation at different depths and lateral locations.

Notably, the specific heat capacity of each of the samples in the modeled section differed very little. This matched expectations as differences in specific heat are very small across most common rocks and minerals (Kavanaugh et al. 1997). However, the porosity has been measured to account for differences in effective specific heat capacity of these formations; in saturated conditions, the volumetric water content (porosity) will significantly alter the formations' diffusivities since the specific heat capacity of water is nearly three times that of most of the values measured for dry rock here.

Table 1 Thermophysical properties determined from rock cores measured in this research, where the first six samples are those comprising the example stratigraphic section and estimated thermal conductivities from literature (λ_{Lit}) are gathered from Kavanaugh et al. (1997), Clauser and Huenges (1995) Jaupart and Marschel (2011) and Touloukain et al. (1981)

Formation	Core Sample Depth (m)	Rock Type	ρ (kg/m^3)	λ (W m^{-1} K^{-1})	λ_{Lit} (W m^{-1} K^{-1})	Porosity (%)	C_p (J/kgK)
Oneota	7.5	Dolostone	2567	4.14 + 0.59	1.6 - 6.2	6.18	832 ± 27.0
Jordan (Core 1)	13.5	Sandstone	2414	3.88 + 0.32	2.1-3.5	13.2	826 ± 32.6
Jordan (Core 2)	162	Sandstone	2135	3.34 ± 0.46	2.1 - 3.5	22.2	818 ± 42
Jordan (Core 3)	169.5	Sandstone	2347	3.86 ± 0.59	2.1 - 3.5	15.3	818 ± 42
St. Lawrence	188.5	Dolostone	2678	4.67 ± 0.24	1.6 - 6.2	5.00	872 ± 69
Tunnel City	18.3	Sandstone	2446	2.59 ± 0.38	2.1 - 3.5	12.8	891 ± 58
Precambrian	73.3	Andesite	2808	3.09 ± 0.05	1.4 - 4.8	0.40	745 ± 27
Precambrian	33.8	Basalt	3191	2.93 ± 0.45	2.1 - 2.4	0.60	770 ± 39
Precambrian	192.2	Dacite	2718	3.76 ± 0.06	1.5 - 2.5	1.00	807 ± 27
Galena	10.5	Dolostone	2684	4.81 + 0.05	1.6 - 6.2	3.62	838 ± 35.6
Silurian	151.8	Dolostone	2810	4.65 + 0.82	1.6 - 6.2	0.05	838 ± 16.3
Precambrian	10.4	Granite	2650	3.10 ± 0.40	1.9 - 5.2	1.00	824 ± 38
Precambrian	Outcrop	Granite	2578	3.69 ± 0.07	1.9 - 5.2	1.60	729 ± 27
Precambrian	Outcrop	Granite	2616	3.35 ± 0.10	1.9 - 5.2	0.70	736 ± 10
Precambrian	16.2	Granite	2604	3.36 ± 0.22	1.9 - 5.2	1.00	802 ± 41
Precambrian	93.7	Greenstone	2956	2.57 ± 0.04	1.0 - 3.0	0.40	765 ± 16
Precambrian	27.7	Iron Formation	3004	2.47 ± 0.34	1.5 - 2.4	0.80	713 ± 16
Platteville	46.3	Limestone	2666	3.17 + 0.80	1.4 - 6.2	1.33	787 ± 51.5
Precambrian	25.3	Metagabbro	3722	2.94 ± 0.18	2.0 - 2.8	0.6	723 ± 58
Barron	50.3	Quartzite	2602	6.71 ± 0.67	5.2 - 6.9	1.5	714 ± 22
St. Peter	68.9	Sandstone	1930	3.45 + 0.67	2.1 - 3.5	27	766 ± 29.6
Precambrian	79.2	Schist	2880	2.58 ± 0.70	2.1 - 4.5	1.8	798 ± 38
Precambrian	46.6	Schist	2198	2.30 ± 0.05	2.1 - 4.5	22.9	868 ± 39
Maquoketa	224.6	Shale	2590	3.39 + 0.40	1.0 - 4.0	6.45	863 ± 39.8
Eau Claire	260.7	Shale	2477	1.84 + 0.03	1.0 - 4.0	5.26	795 ± 129.0

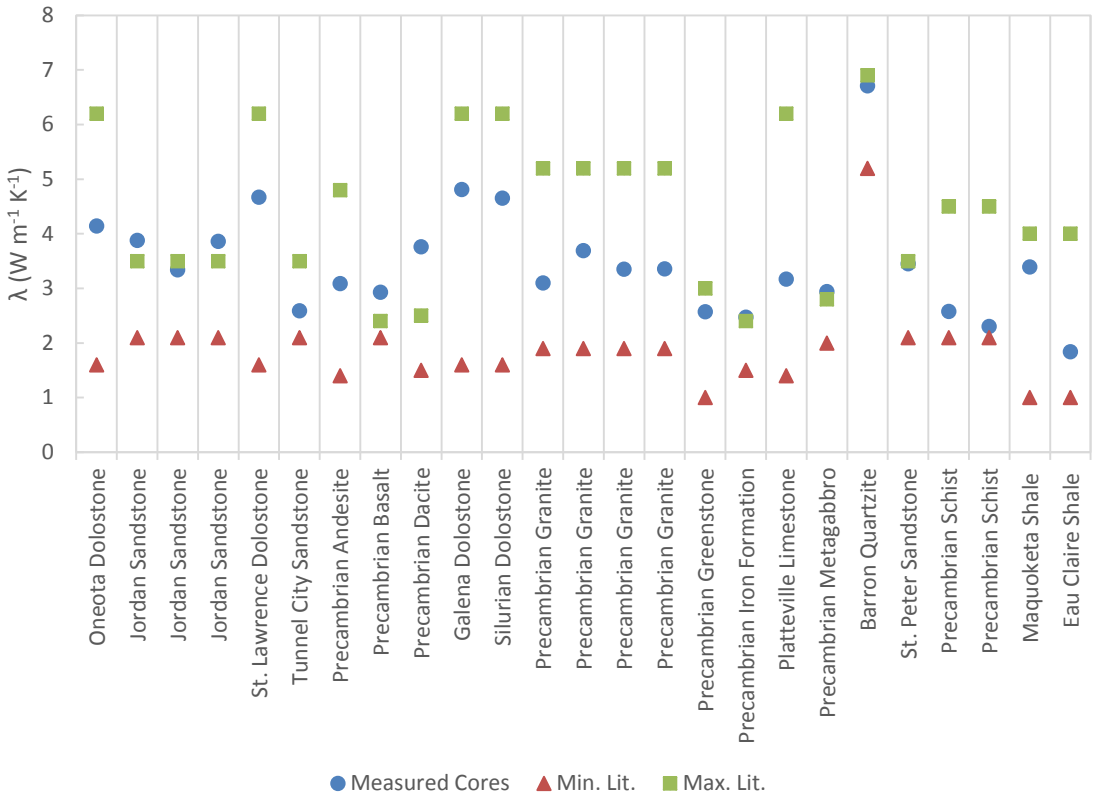

Figure 8: Experimental thermal conductivity values denoted by circles. Typical range of thermal conductivity values specified by literature denoted by triangle and squares for low values and high values, respectively (adapted from Meyer, 2013).

Mineral abundances in some of the samples were assessed using X-ray diffraction (XRD), revealing significant differences in the proportions of common minerals, even within the same "rock type." Within the Jordan formation, the younger of the two samples from the same borehole was 100% quartz, while the older had approximately 20% feldspar and 80% quartz. The Tunnel City Sandstone showed 41% quartz content with 59% dolomite. The only dolostone of the group examined with XRD showed an abundance of 86% dolomite with 14% quartz, possibly from chert nodules or clastic sedimentation. The XRD methodology used to find these mineral abundances and plots generated for the XRD analysis are detailed in Meyer (2013).

3.5.2 Modeling Results

Progressively deteriorating thermal resources over time are apparent in each of the model runs. EWT decreases more quickly and falls to lower ultimate temperatures in cases with lower conductivity and vice versa. Lower formation temperatures result in lower wall temperature, which reduces the amount of energy that the fluid can pick up in the ground loop. As expected, EWT for the conservative thermal property estimation case would be lower than the others at every time step (Figure 9). The rate of EWT decrease is larger for the lower-conductivity cases, easily seen in the semi-log space (Figure 10).

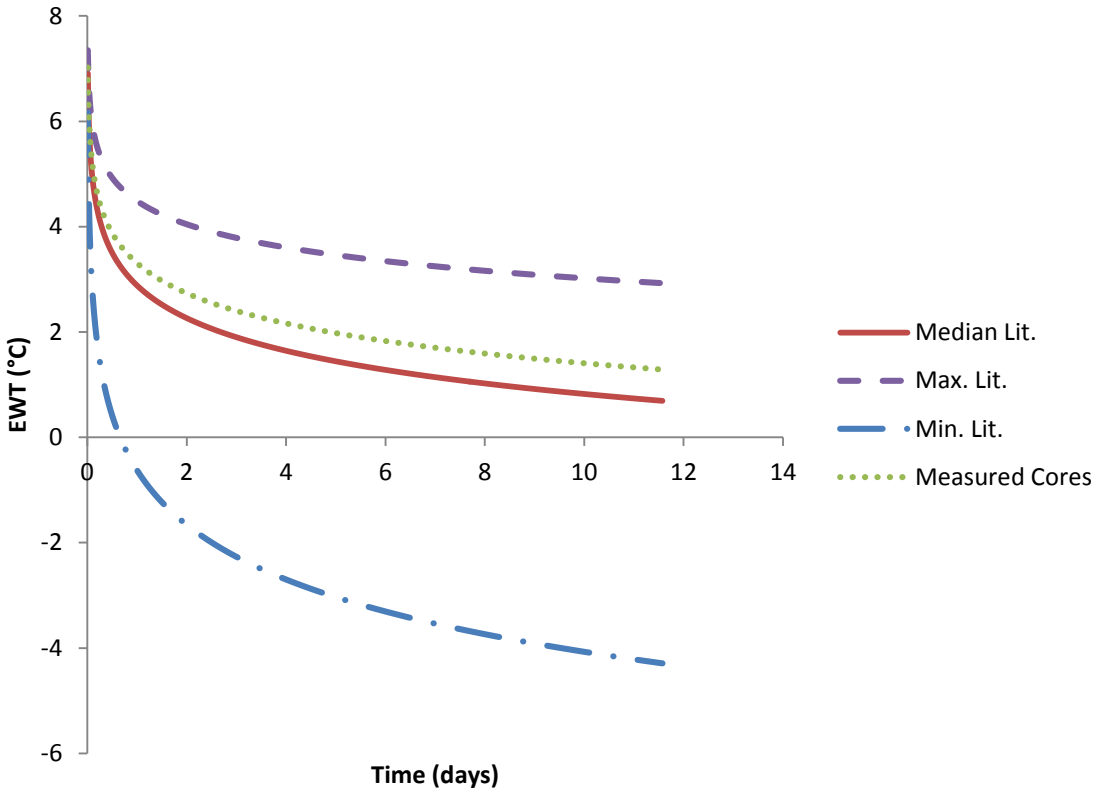

Figure 9: Lowering of EWT over time at maximum capacity of the example system for the four subsurface thermal conductivity estimates (negative results are unrealistic, but demonstrate trends for continued heat extraction).

The decrease of the EWT over time represents the depletion of thermal energy in the formations. This is seen in each chart's similarity to drawdown curves commonly found in

hydrogeologic literature. Though EWT is physically separated from the rock mass, EWT is a measure of how much temperature has been “drawn down” in the formations. The EWT curves in Figure 9 and Figure 10 are analogous to those used in curve fitting for the Theis (1935) and Cooper-Jacob (1946) methods of pumping test analysis, respectively.

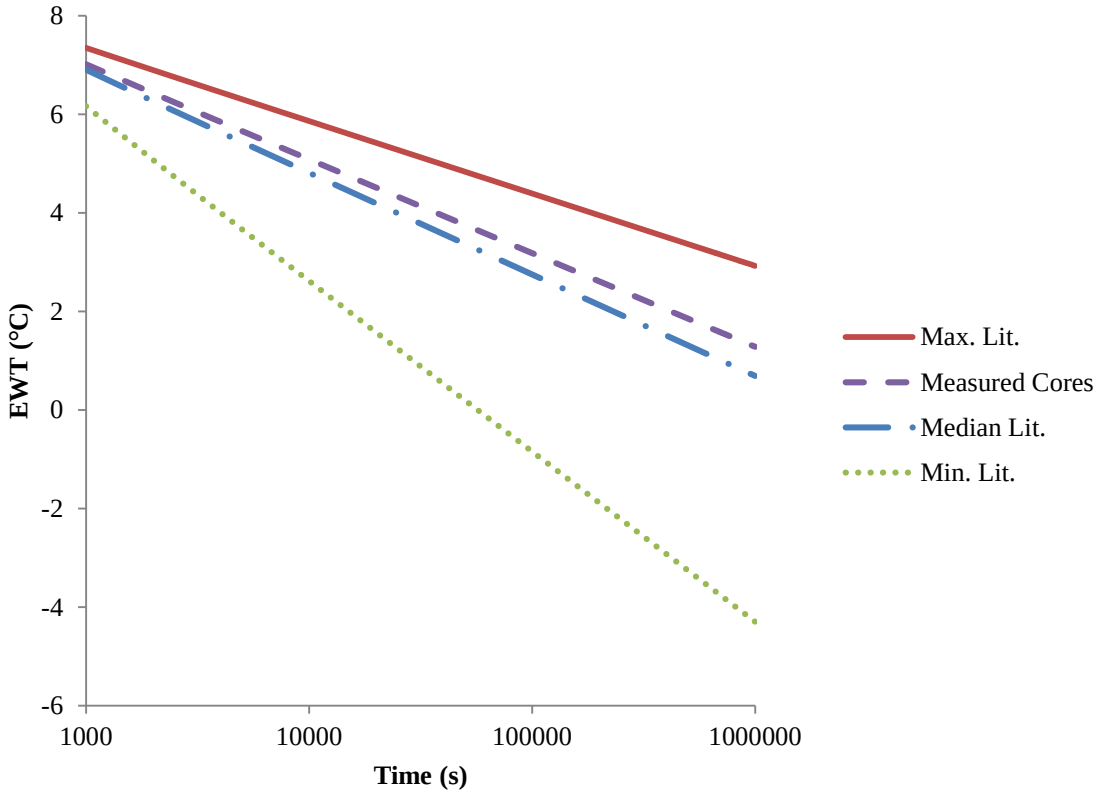

Figure 10: The same model results as in Figure 9, except plotted on semi-log axes to demonstrate the temperature continues to degrade at a faster rate for lower conductivity over time, something not apparent in Figure 9.

3.6 Discussion

Recalling that each of these model results is a different representation of the same materials in the same stratigraphic column, the deviation from the “measured” model is significant. Substantial differences in the performance of this system exist simply because of the different thermal conductivity estimates for this site. 7000 s (about 2 h) after the heat load was applied, the optimistic inputs lead to an EWT 0.7 °C higher than the case with measured rock core

inputs. At the same point in time, the conservative estimates fell 2.2 °C lower than the measured case. Critically, EWT for the lower literature values falls below water's freezing point at 58000 s (about 16 h). However, the LWT of the heat pump would have fallen below freezing well before this point, creating issues with freezing heat transfer fluid if no anti-freeze solution is employed. The sub-zero-degree EWT result is more significant in identifying the lower operating ranges for heat pumps; most residential heat pumps cannot operate with EWTs significantly below 0 °C.

The amount of heat a given heat pump can extract at maximum load varies with the temperature of the evaporator. During normal GSHP operation, decreased EWT leads to less heat extraction and lower efficiency. Therefore, actual heat pumps may tend to "bottom out," no longer being capable of transferring enough heat to meet demand. This is not simulated here as the model's boundary condition mandates that the building's heating demand is met by a constant, defined heat extraction rate, which is only applicable in a fraction of heating situations. Regardless of how the EWT results are viewed, dropping EWT is undesirable because of the reduction in heat extraction, drop in efficiency (COP), and, in some cases, system failure (e.g., inoperable heat pump or frozen pipes).

The ultimate, preventable cause of such unsustainable system loads is the improper sizing of the ground loop. As mentioned in the introduction, economic considerations of ground loop costs influence homeowners to accept undersized ground loops. In these cases, the "rule of thumb" design may assume operation along the line of the "optimistic" subsurface conditions in Figure 9. However, if the actual prevailing conditions were closer to the conservative values in the same figure, the system would be hampered by low efficiency at the very least and possibly require more auxiliary heat than the system's designers had originally planned, further lowering the cumulative efficiency of heating the building.

The expected performance of the GSHP system has been modeled as a function of the rock formations' measured thermal properties and the vertical extent of each formation along the borehole. In this instance, using the average of the book values gave a result similar to the measured core, though that need not have been the case. If the boring encountered only Jordan sandstone, the "book" value would have significantly underestimated the thermal conductivity of the system. These measurements and knowledge of geology at the proposed site were an accessible means of assessing the performance of the hypothetical GSHP system. This performance was represented by the EWT versus time curve expected in the model, allowing the potential range of system performance to be narrowed from the large range expected from the range of thermal conductivity values assigned to generalized rock types. However, this narrowed range of system performance is based on an extreme loading scenario, which represents a higher standard of performance than is normally expected from normally-grouted U-bend GHEs. Loads on a GSHP system would usually be less than the 70 W/m case presented, and they typically are variant with respect to time.

3.7 Conclusion

Thermal conductivity, specific heat capacity, porosity, and density were measured in twenty-five rock cores of various depths, lithologies, and formations. This study was mostly concerned with the differences in thermal conductivity between typical values in handbooks and those measured in the laboratory. The tested Paleozoic sedimentary rocks ranged in conductivity from the Eau Claire Shale's 1.84 W m^{-1} K^{-1} to the Galena Dolomite's 4.81 W m^{-1} K^{-1}. Thermal conductivity of the measured Precambrian igneous and metamorphic rocks ranged from 2.30 W m^{-1} K^{-1} for schist to 6.71 W m^{-1} K^{-1} for quartzite. Laboratory measurements were able to account for specific lithology, which is usually not accounted for in tables of broad rock categories.

Accurately characterizing the lithology and thermophysical properties of individual formations encountered by the ground loop boreholes would allow design and install contractors to

implement systems more effectively. “Rule of thumb” designs and thermal conductivity indexed by generalized rock type are insufficient since the subsurface interaction with ground loops varies drastically even within the same “rock type.” Characterization by formation is especially applicable in regions where the areal extent of each formation is great with similar lithology throughout. Since formations are, by definition, lithologically distinctive, it serves to reason that they are thermophysically distinctive. The confirmation of this hypothesis explains why broad rock types (e.g. sandstone, limestone, granite, schist; sedimentary, igneous, metamorphic) cannot be viewed as thermally characterizable.

Chapter 4: Investigating Ground-Coupled Heat Pump Performance with Fiber-Optic Distributed Temperature Sensing

4.1 Introduction

Ground-coupled heat pump (GCHP) systems are widely seen as an energy-efficient solution for residential heating and cooling (Esen et al. 2009). The energy efficiency of a GSHP stems from the transfer of energy in the form of heat from one location to another, contrasting with conventional furnaces which typically convert energy from stored, chemical form to heat through combustion. GCHP systems also benefit from a smaller temperature difference between its heat sources and sinks than other heat pumps like air conditioners or air-source heat pumps; ground temperatures are typically lower than air temperature during summer months and higher than air temperature in winter months.

The efficiency of GCHP systems can vary widely due to differences in design, heat pump model, and thermal properties of the subsurface in contact with the ground heat exchanger (GHE). This efficiency is typically measured with a coefficient of performance (COP), which is a ratio of heat transferred into or out of a space being conditioned over electrical power consumed. Man et al. (2012) experimentally studied how various system aspects affected COP, concentrating mostly on the difference between intermittent and continuous operation of the heat pumps. Chung and Choi (2012) studied the effects of flow rate and exchanger length on COP, paying particular attention to the speed of the heat pump's compressor and other mechanical aspects of GSHPs. Esen et al. (2009) also studied the effect of heat exchanger length on COP, while also measuring subsurface temperatures along three GHEs at 30-m intervals. In this study, we examine a closed, vertical-loop ground-coupled heat pump (GCHP) system installed at a residence near Grand Marsh, Wisconsin, by monitoring the electrical power draw of the system components and temperatures of the system's heat exchange fluid. In

this study, we have used both conventional temperature-monitoring instruments and distributed temperature sensing (DTS).

DTS is a relatively new temperature monitoring technique, only expanding into a variety of research and industrial applications since the early 2000s (Grattan and Sun 2000). The main advantage of DTS over conventional temperature sensing techniques is that it provides continuous profiles of temperature along the optical fiber used for measurement. Such a feature is particularly advantageous for acquiring temperature profiles along GHEs. In this study of heat exchange and in many others, DTS uses standard fiber optic communications cables with a 50-μm silica core. DTS sensing interrogators shoot infrared (1064 nm) lasers down the fiber. The infrared light has a tendency to scatter back toward the laser equipment, and some of this backscatter is useful in determining the temperature of the fiber. Tyler et al. (2009) and Selker et al. (2006) provide background into considerations for high-precision and high-accuracy DTS measurements when utilizing this particular type of DTS, referred to as Raman backscatter DTS.

DTS has been applied to GHEs in previous studies, usually in enhanced or distributed thermal response tests (ETRT or DTRT, respectively). Initially pioneered by Fujii et al. (2009), researchers perform these tests to measure thermal properties of the borehole, rock, and soil surrounding a GHE in a distributed fashion. Results of the tests are then applied to the design of other GHEs at the site of a new GSHP system. The tests typically involve dropping fiber optic cables down supply and return sides of a GHE, and measuring the spatial distribution of temperature when constant flow rates and heat loads are applied to the GHE from a mobile pump and electrical heating element (Acuña et al. 2009).

What makes the system unique is that it supplies all of the host residence's heating and cooling needs, including domestic hot water (DHW), during all but the most extreme cold weather

conditions. “Extreme cold” relative to the host site is typically sustained ambient air temperature below -20 °C for consecutive days (average daily temperature about -25 C or lower). In these conditions, the residence’s original liquefied petroleum forced-air furnace is used to ensure that circulation water does not freeze. Furthermore, the study site is in a colder climate than in many other study areas, with an average annual temperature of about 7 °C and an average winter temperature of -8 °C. According to the Wisconsin State Climatology Office, the study site averages about 4375 heating degree days (°C with a temperature base of 18 °C) per year. The same site only experiences about 275 cooling degree days (°C with a temperature base of 18 °C) per year. The system will provide some insight into the performance of GSHP systems that do not benefit from annually balanced heating demands.

4.2 Materials

The GCHP system at the studied residence (Grand Marsh, Wisconsin, USA) consists of two heat pumps and three vertical GHEs. Incoming water from the GHEs is first piped through a water-to-water heat pump rated for 7.3 kW of heat extraction (WaterFurnace NSW025 DHW). Then, the leaving water from the water-to-water heat pump passes through a water-to-air heat pump rated for 10.6 kW of either heat extraction or rejection (WaterFurnace NV036). Heat extracted by the water-to-water heat pump serves DHW needs in the residence, and underfloor heating is delivered through a separate water loop connected to the DHW via a plateframe heat exchanger. Heat extracted or rejected by the water-to-air heat pump conditions upper floors of the home connected to ductwork. The water-to-air heat pump’s compressor is equipped with a desuperheater, which uses waste heat to preheat cold well water delivered to the DHW system. Reference photos of the installation can be found in Appendix 4.

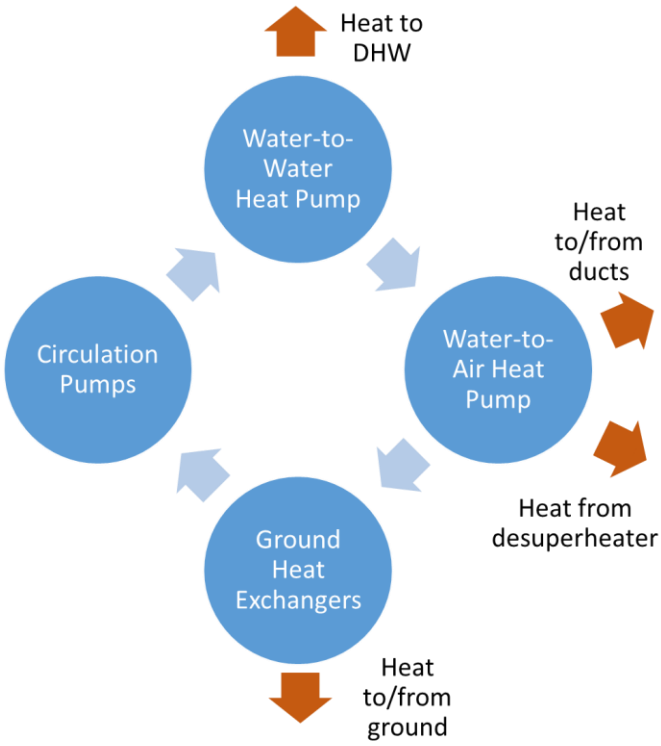

Figure 11: Flow diagram showing the flow of heat through the instrumented heat exchange system.

Water leaving the water-to-air heat pump is finally returned to the three GHEs through a manifold. The manifold has a series of valves configured to allow the system user to choose the flow pathway through the GHEs. Flow can be directed to an individual GHE, to two at a time, through all three in series, through all three in parallel, as well as many other configurations. However, the system is typically set to direct flow to all three GHEs in parallel so as to minimize the pumping power required to reach a given flow rate.

Three circulation pumps are currently installed at the site, and they are programmed to activate incrementally with increased thermal load on the system. As a result, the volumetric flow rate for the system typically falls within a range of 12 L min^{-1} to 49 L min^{-1}. Faster flow rates are more energy intensive than slow flow rates due to increased pumping power, but increasing the system flow rate results in less temperature drop across the heat pump for a given heat

extraction rate. This is especially important during winter months when large temperature drops could potentially bring the heat exchange fluid (water) near its freezing point. Furthermore, high flow velocities can potentially enhance heat transfer within the GHE by maintaining high Reynolds and Nusselt numbers. By definition, a higher Nusselt number means that the system has a higher heat transfer coefficient, if geometry and material properties are held constant (Dittus and Boelter 1985).

The three GHEs for the GCHP system consist of conventional, closed-loop u-tubes with 5-cm nominal diameter high-density polyethylene pipe (standard dimension ratio of 11). Both pipes for each GHE continuously run from the manifold in the basement of the residence to the bottom of their respective boreholes. The u-connection at the bottom of each borehole is the only fusion fitting in each loop. The horizontal section of each pipe was laid in a trench at a depth of approximately 2 m. Due to drilling difficulties, the three GHEs are not of the same length, complicating system analysis somewhat. The first GHE reaches a depth of 90 m, the second reaches a depth of 95 m, and the third reaches a depth of 125 m. The total length of the loops must also include the horizontal length from the residence to the GHE boreholes. The implication of unequal GHE lengths is that flow may not be divided equally between the three GHEs when the flow network is parallel; the longest GHEs could receive the lowest flow rate and the shortest could receive the highest.

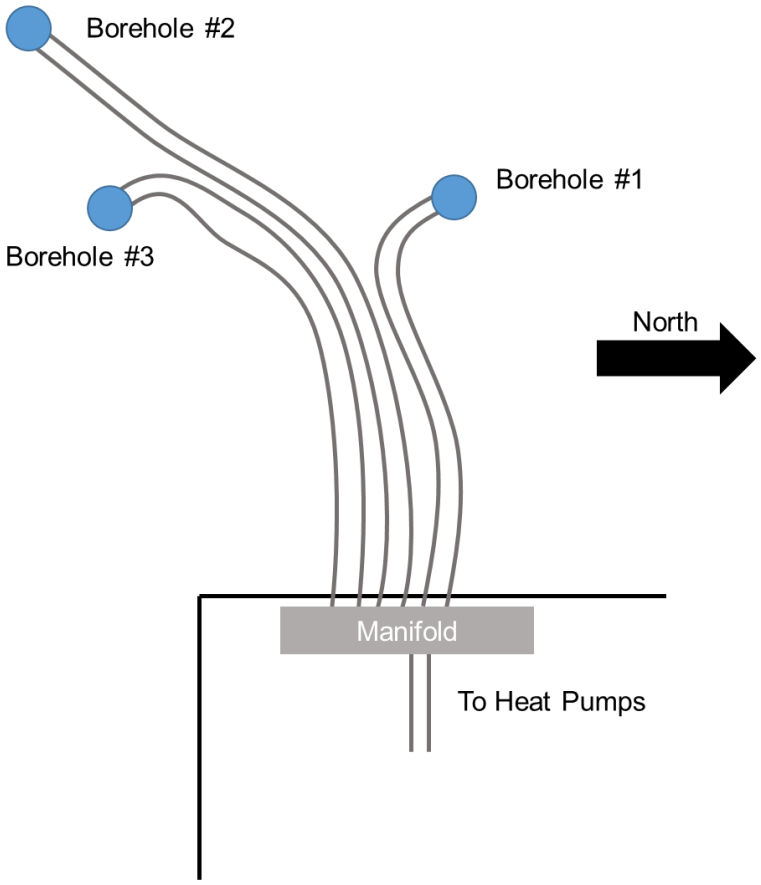

Figure 12: A plan view of the approximate locations of GHEs with respect to the corner of the house where the continuous HDPE pipes are connected to the manifold. The figure is not to scale.

The system installation includes instrumentation to evaluate its efficiency over time. Flow meters (Grundfos VFS QT sensors) were installed on the GCHP-related water loops in the residence, including the loop carrying water from the GHEs, the DHW loop, the under-floor heating loop, and the desuperheater loop. Each flow meter also measures temperature in direct contact with the fluid inside the pipe. Additional temperature measurements are made with thermistors (Campbell Scientific 109 SS) attached on the outside of metal pipe, firmly fastened and insulated to ensure good contact with the pipe surface. Four WattNodes (Continental Control Systems LLC WNB-3Y-208-P) were installed and connected to the GCHP's circuit breaker. The WattNodes are root-mean-squared, alternating current transducers that ultimately measure the electrical energy supplied to all components of the GCHP system.

A datalogger (Campbell Scientific CR10X) with two switch closure modules (Campbell Scientific SDM-SW8A) was used to collect all GCHP system data produced by the aforementioned instruments. Voltage response from the flow meters' sensors were linearly related to their temperature and flow rate measurements. Externally affixed thermistors used AC half bridges to measure voltage outputs and the Steinhart-Hart equation to convert measured resistances to temperature. The WattNodes emit pulses that correspond to units of energy. Pulses were recorded by the datalogger through its connected switch closure modules. A second datalogger (Campbell Scientific CR10X) was installed to record weather conditions from a weather station affixed to the roof of the residence. Both dataloggers were connected to PCs, which were then setup for remote access.

Table 2: Summary of the data collection devices and measurements within the GCHP system.

Instrument	**#**	**Units Measured**
Flow Meter (Flow)	5	L min^{-1}
Flow Meter (Temperature)	5	°C
Thermistor	4	°C
Current Transducer	12	W h
DTS Fiber	4	°C (function of m and s)

The unique aspect of performance monitoring for this residence is the installation of fiber optic cables for DTS within the GHE pipes. Originally, six steel-clad fiber optic cables were planned for installation at the site (one for each of the supply or return pipes of the three GHEs). The fibers are standard multimode communications optical fibers with a core diameter of 50 μm (OM2 optical fiber). However, only two of the GHEs were successfully instrumented with DTS because fibers in one of the GHEs were accidently mishandled during installation. Installation

consisted of guiding each fiber through one end of the GHE with a pull string. The bottom of the fiber was pulled beyond the bottom of the GHE pipe to protect it from the fusion process on the GHE's u-bend. The other end of the fiber was guided through the manifold inside the residence where it could be pulled through a compression fitting. A compression fitting is essential to prevent leaks during the long-term operation of the system.

A DTS interrogator (Sensornet Halo) stimulates the fibers with infrared laser light and reads the backscattered Raman signal within Stokes and anti-Stokes bands. Processing routines then convert the intensity of these signals into temperatures. With the DTS fiber installation setup employed at the residence, certain uncertainties exist in the distributed temperature data obtained in the system. Namely, without calibration baths on both ends of the cable, certain attenuation constants unique to the steel clad cable cannot be accurately ascertained. Uncertainty in attenuation and other correction constants lead to uncertainty in absolute temperature. However, relative temperature changes across the cable can be more confidently stated.

The vertical heat exchange loops of the study site intersect three geologically distinct formations: unconsolidated sand and clay of the Big Flats Formation to 55-m depth, quartz sandstone of the Tunnel City Group from 55 m to 108 m, and granite basement rock extending to an unknown depth below the base of the Tunnel City Sandstone. 15-cm PVC casing was placed to a depth of approximately 60 m for each borehole. The site stratigraphy was ascertained by logging samples from the boreholes during drilling. After drilling was completed, down-hole geophysical logs were acquired to gather further information about the site geology and the borehole itself. Geophysical logs included gamma, self-potential, resistivity, fluid conductivity, temperature, caliper, and optical borehole image. A pumping test was also performed to better understand the distribution of hydraulic conductivity in the soil and rock layers (Appendix 3).

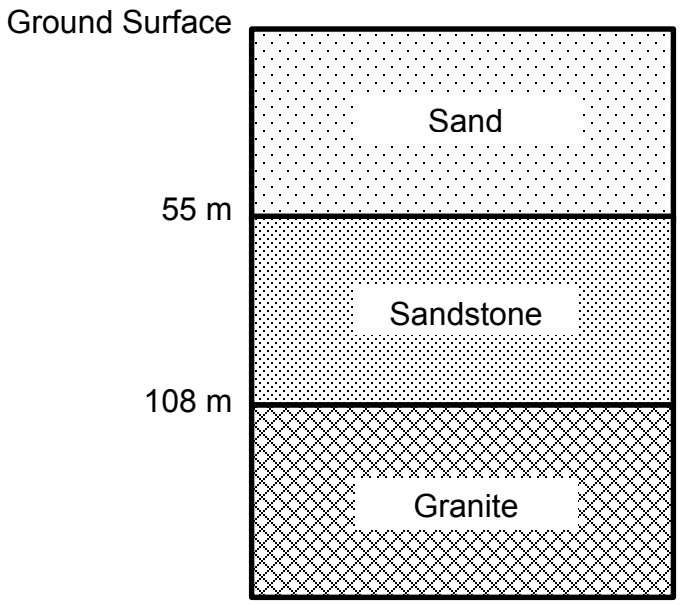

Figure 13: Summary of the geology encountered by GHEs at the study site.

4.3 Methods

As mentioned in the Introduction, the main measure for the efficiency of a GSHP system is its COP. COP consists of the amount of energy moved per electrical energy consumed. During the heating season, the electricity supplied to pumps and compressors generates useful heat. Therefore, different calculations are used during the heating and cooling seasons. For this study, the early heating season was examined specifically, so heating-season COP, denoted COP_H , was used consistently for all data presented.

$$COP_H = \frac{Q+W}{W} \quad (29)$$

In Equation 29, the heating-season COP equals the sum of the heat extracted from the GHE (Q) and the electrical energy supplied to the system (W), divided by the electrical energy. The heat extracted is calculated by measuring the difference in temperature between the supply fluid and the return fluid. If the flow rate and heat capacity of the fluid is known, then the heat transferred can be calculated (Equation 30). Electrical energy consumption data was acquired directly from the installed WattNodes.

$$Q = \Delta T \cdot \dot{m} \cdot c_p \quad (30)$$

At the residence, ΔT was measured for the system overall, but also for the heat pumps separately by using thermistors between the series-aligned heat pumps. In doing this, the Q and COP_H could be calculated both for the system as a whole and for the separate heat pumps.

Measurements of distributed temperature within the GHEs can be applied to measures of the effective thermal properties of sections within the pipe. When the GCHP is under a constant thermal load, the change in temperature over a section of the GHE with known flow rate is equivalent to the heat flux through that section of the GHE. This is the same as the calculation that was performed to determine the heat flux in the COP calculations (Equation 30). Given the heat flux, thermal properties of the subsurface can be determined based on line source models as in Acuña (2010) and Beier et al. (2012).

4.4 Results

Measurements at the site consist of a variety of system facets, including system temperatures, efficiency, and weather conditions. However, the results are most important as a blueprint for potential future applications of DTS in GCHP systems; long-term monitoring with DTS continues to be a novel technology for application in GHEs. All of the measurements will continue to build a database from which the sustainability of the system's net heat extraction may be observed. However, some preliminary statements can be made about the system's performance through the year 2014.

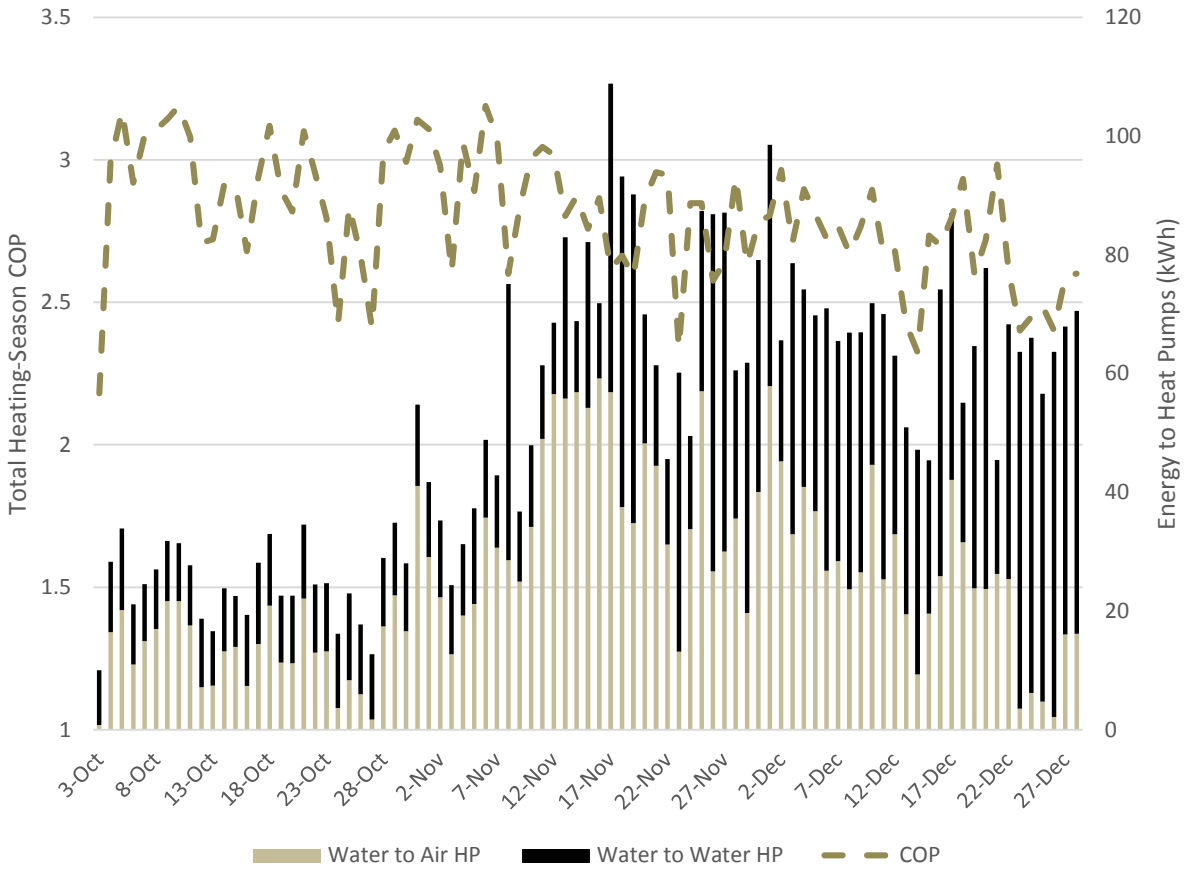

Figure 14: The track of daily total COP of the system through the beginning of the heating season is plotted with the daily energy consumption of heat pumps at the site. The relationship shows that drops in system COP usually corresponds to a higher proportion of water-to-water heat pump use.

Based on the temperature change across the heat pumps and power measurements, COP was calculated for the system as a whole during the beginning of the 2014-2015 heating season. Figure 14 demonstrates that the COP for the system as a whole varied greatly on a day-to-day basis, ranging from a low of 2.18 on October 2 to a high of 3.19 on November 11. This variability had more to do with characteristics of the heat pump hardware than weather conditions, EWT, or other factors. The two heat pumps employed at the residence have inherent differences that lend themselves to different relative efficiencies. The water-to-water heat pump has a single-speed compressor that was frequently cycled on and off to accommodate DHW demand, which tends to be variable. In contrast, the water-to-air heat pump has a variable-speed compressor,

which tends to be more efficient than a single-speed compressor since it can adapt to heating demands.

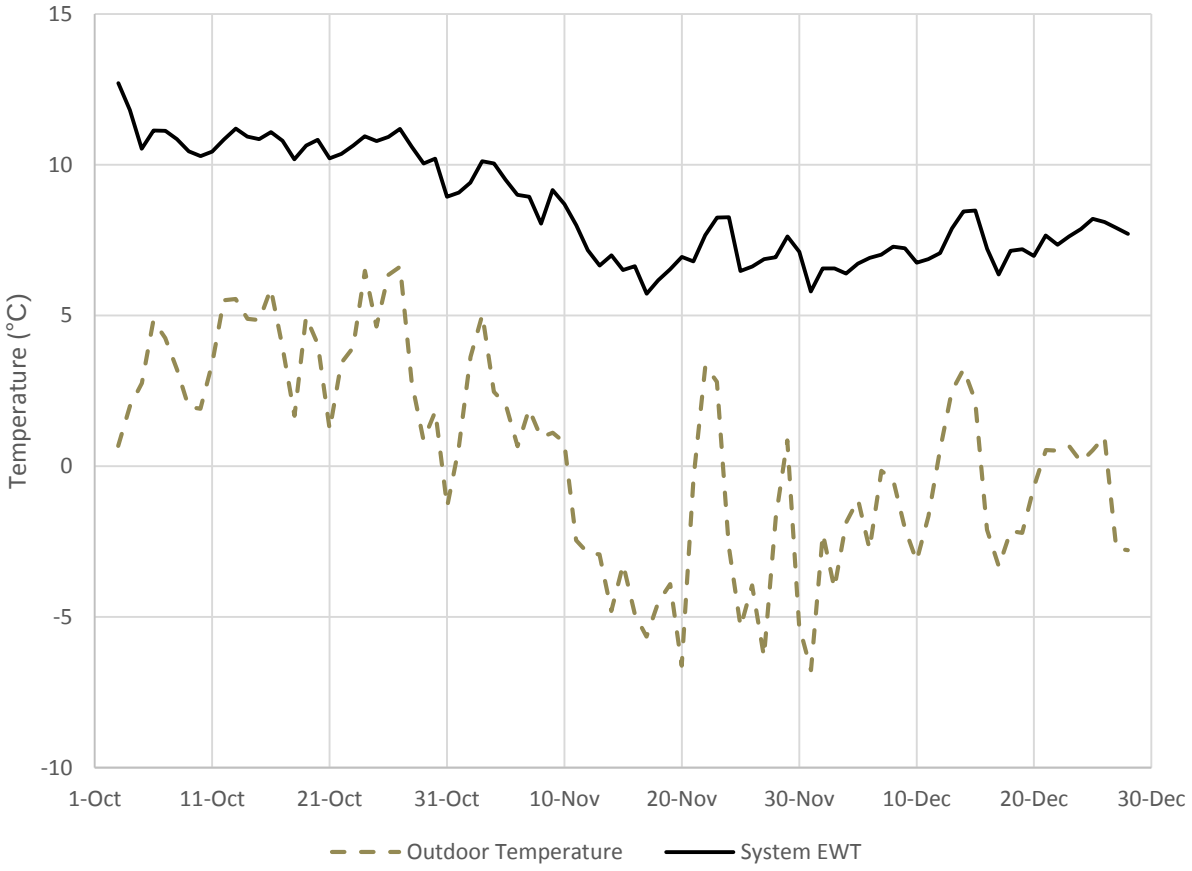

Figure 15: The record of the daily average outdoor temperature is plotted with the daily average EWT for the system. The EWT appears, for the most part, as a dampened form of the outdoor temperature recorded at the site.

To provide a context for the other data presented here, outdoor temperature over time is displayed for the site during late autumn and early winter of 2014 (Figure 15). Compared against averages for nearby weather monitoring stations reporting to the National Oceanic and Atmospheric Administration, the 2014 season had an unseasonably cold November and an unseasonably warm December.

Heating season data was collected by the DTS unit during the middle and end of the 2013-2014 heating season and during the brief 2014 cooling season. Dozens of temperature profiles could

be generated and presented from just a few days of data collection since four fibers were measured and a new measurement is taken on a 1- to 4-min interval. Therefore, only a handful of profiles are presented here to demonstrate what can be expected from a long-term DTS monitoring system installed in the vertical GHEs of a GCHP system.

During January of 2014, results in Figure 16 show that the temperature gained in the loop was only 1.4 °C, far less than the 3.5 °C to 7 °C typically desired from GCHP design (ASHRAE 2011). However, temperature recovery in the GHE is highly dependent on the flow rate of water through the GHE (Walker et al. 2015). The high flow rates employed at the site (35 L min^{-1} to 50 L min^{-1}). The down-flow fiber in Figure 16 shows limited heat recovery in the first roughly 20 m. This corresponds to the length of pipe in horizontal trench. Nearly constant heat recovery is then shown for nearly 90 m, into the up-flow fiber. Usually, heat recovery tapers off starting in the middle of the borehole on the up-flow side. During the coldest months of the 2013-2014 heating season, heat recovery tended to actually reverse in the final 20 m of fiber (see Figure 16), indicating that the exchange fluid temperature exceeded the temperature of the surrounding ground.

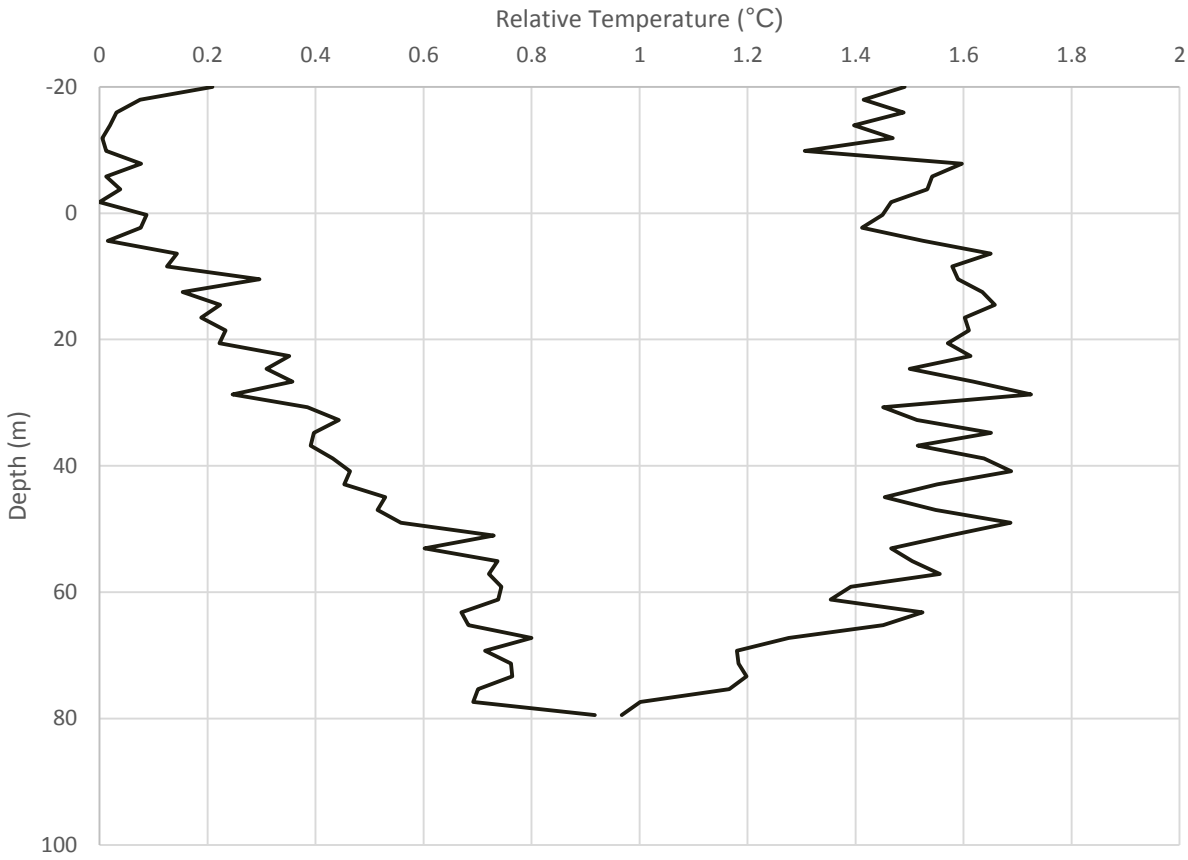

Figure 16: An example profile of temperature increase along the flow path in a winter-season GHE. The line on the left represents the downward flow segment, and the right is the upward flow segment. This particular profile was taken from the experimental site's second GHE on January 30, 2014. At the time, both heat pumps were running and extracting heat. The profiles were collected in successive 1-min acquisition cycles. Depth is relative to the top of the borehole casing.

Results from monitoring during the cooling season contrast somewhat with those from the winter. As shown in Figure 17, heat rejection occurs at a steady rate from the house to the bottom of the borehole. However, not far after the halfway point of the fluid travel path, the rate of heat rejection slows, before nearly halting or even reversing at the top of the borehole.

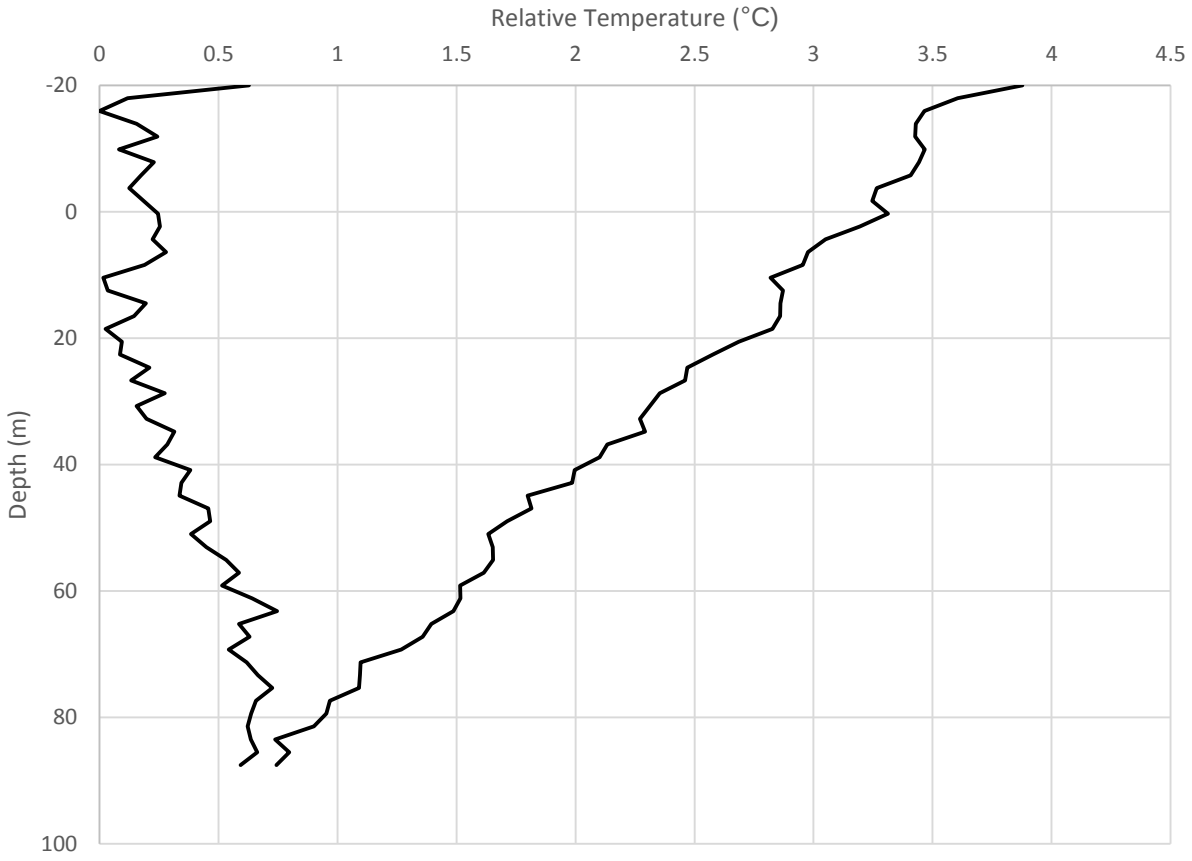

Figure 17: An example profile of temperature decrease along the flow path in a summer-season GHE. The line on the left represents the upward flow segment, and the right is the downward flow segment. This particular profile was taken from the experimental site's second GHE on June 23, 2014. At the time, only the water-to-air heat pump was running and injecting heat. The profiles were collected in successive 1-min acquisition cycles. Depth is relative to the top of the borehole casing.

A final example of temperature profile during the autumn was acquired to show temperature profiles in the GHEs when there is no demand for space conditioning. During seasons with low space heating and cooling demands, the net heat balance extracts heat from the ground to supply the residence with heat for DHW. Figure 18 demonstrates this situation with a very slight change in temperature through the GHE. However, this figure also demonstrates some of the complications with attempting to interpret the DTS profiles during a time with variable thermal load application. The profile doesn't show a consistent shape aside from the fact that the first 50

m of the GHE are at a temperature lower than the rest of the profile. The jumps in this plot could be due to short cycles of DHW demand.

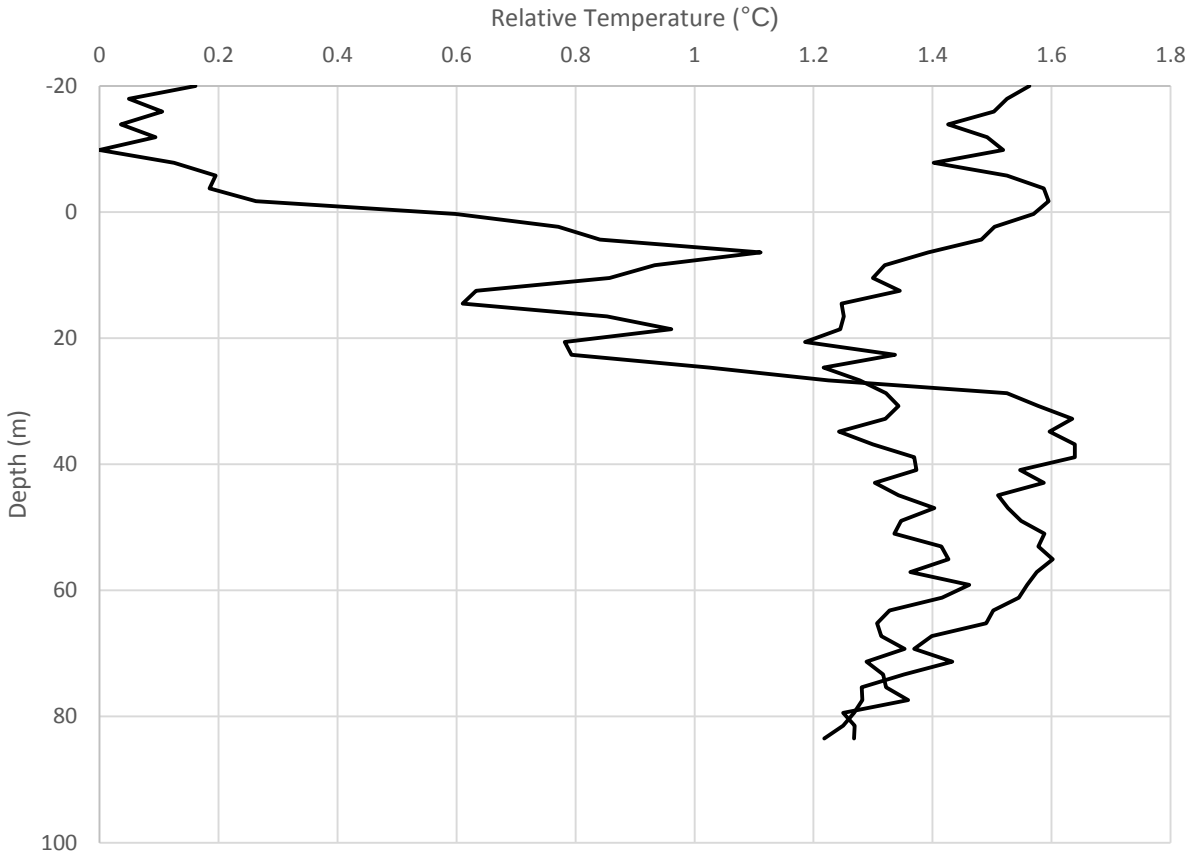

Figure 18: Autumn temperature profile. Profiles during seasons without space heating and cooling demand are dominated by intermittent loads from DHW.

4.5 Discussion

For the period of continuous monitoring of the system in the first portion of the 2014-2015 heating season, COP was related to both the total daily energy usage and the relative energy consumption of the heat pumps. As seen in Figure 3, the days with the lower COPs tended to be days in which the water-to-water heat pump consumed a large portion of the day's total energy consumption (≥50%). These days also tended to be days with low total energy consumption, such that water-to-air heat pump, which is relatively efficient, had little weight in

the system COP calculations. Figure 15 can also be related to the discussion of the system COP, as the outdoor temperature tends to track very well to the energy requirements of the system displayed in Figure 14. There remains a certain component of the system energy requirements that are independent of the site weather conditions (namely DHW demand), but outdoor temperature exerts the most noticeable effect when the trends of Figure 14 and Figure 15 are examined. This correlation also exists between the system EWT and the heat loads, ultimately resulting in the system EWT appearing as a smoothed version of the outdoor temperature.

As mentioned above, the COP signal is dominated by the magnitude and breakdown of the system energy consumption, but EWT also plays a role in the COP, which makes intuitive sense since the efficiency of any heat pump is based on the temperature difference between the heat sink and heat source (i.e., the heat pump can more easily extract heat from a heat source with a higher temperature and vice versa for the rejection of heat to a heat sink). One application of this principle is the aforementioned inefficiency of the water-to-water heat pump under most conditions (COP of < 2.5). This is mainly the result of the heat pump's application to a heat sink (the hot water storage tanks) at elevated temperature; typically, the water-to-water heat pump runs while the heat sink has a temperature around 40 °C. The heat pump's compressor is forced to consume more energy to transfer energy from the 10-°C (or less) heat source to the 40-°C heat sink, resulting in lower COPs than the water-to-air system.

The results of this study demonstrate the preliminary utility of DTS application in the study of the operational efficiency of a GCHP system. Figure 16, in particular, shows how the heat flux in the GHE changes based on location. Temperature recovery was clearly the greatest within the borehole on the downward segment of the flow in particular. This makes sense because the greatest difference between the fluid temperature and near-borehole ground temperature would occur there. By the time the fluid flowed through the u-bend and started traveling upwards, the

fluid approached the ground temperature, thus slowing the rate of heat recovery. Some thermal interaction between the down-flowing and up-flowing portions of the GHE could also be a factor in limiting the total heat gained by the system. However, it is difficult to ascertain the full effect of this thermal interference from profiles like Figure 16 since the position of the pipes is unknown in any cross-section of the GHE. The effect of thermal interference would vary based on the proximity of the GHE pipes to one another.

There appears to be little difference in the heat flux due to differences in the thermal properties of the two formations intersected (sand and sandstone). This could potentially be due to the thermophysical similarity of the two formations, or it could be due to the response being below the threshold of the instrument sensitivity. Since the difference in temperature between supply water and return water for a given profile at this site does not typically exceed 4 °C, finer temperature and spatial resolutions would be needed to recognize minor differences in thermal properties. With the DTS equipment used, such temperature and spatial resolutions could not be obtained, especially since short DTS acquisition times (usually 60 s or 120 s) were used during data collection. These times had been chosen as a tradeoff between spatial “smearing” of the temperature signal and the temperature resolution of the profile. However, this resulted in somewhat jagged signals due to the measurements’ lack of precision. Despite this lack of precision, the experimental setup proved to be adept at discerning the reversal of heat recovery in the trenched sections of the GHEs. The variability in the rate of heat transfer along the pipe of the GHE poses a challenge to modeling efforts that use constant spatial heat flux as a simplifying assumption such as those based in the infinite line source.

The heat recovery reversal is important to note since it essentially represents wasted heat for the system. Though the GHE pipes were placed in trenches nearly 2 m deep, Department of Transportation and North Central River Forecast Center measurements of frost depth in the region for January 2014 approached 1.75 m. Given those circumstances, a situation can be

envisioned where the fluid loses heat while traveling back to the residence. A trenched section of the GHE is vulnerable to heat overextraction since the GHE itself lowers the temperature of the surrounding soil volume, in addition to the temperature drop propagating from the ground surface during the winter. With DTS, it appears that this hypothesized phenomenon of heat loss was observed. The extreme depth of the frost line is a rare case for this particular residence's region (typically only reaches ~1 m), but it is still indicative of the effect of seasonally changing surface temperature on shallowly buried heat exchange pipes.

During the summer, similar observations can be made from the DTS profiles acquired at the study site. Though perhaps not amounting to a full reversal of the heat flux, the section of trenched pipe on the return to the house appears to hold a roughly steady temperature. This however, may be due to the fluid reaching the natural ambient subsurface temperature. The fact that the rate of temperature change slows well before the trenched section of pipe provides an additional line of evidence in support of the hypothesis that fluid within the GHE is approaching the subsurface far-field temperature.

4.6 Conclusion

This study advances long-term DTS as a complimentary piece of monitoring equipment for GCHP systems. At a residential GCHP installation in a heating-dominant climate, measurements were made to calculate COP for the system as a whole during the heating season. COP was shown to be a function of EWT and heat pump usage. EWT and heat pump usage were correlated to weather conditions at the site. The DTS data from the study site showed that the majority of heat was being transferred on the downflow pipe of the GHE after it had passed into the borehole. The potential for a system to lose heat through trenched sections of pipe during the winter was discovered as an inefficiency that may afflict many GCHP systems in heating-dominated climates. Systems with long trenched sections of GHE pipe like the one featured in this study (20 m) may be at more risk to this kind of inefficiency. Though major

thermophysical changes with depth were not identified with DTS at this site, the thermal effect of differing lithological sections may be identified with DTS in future studies. Such effects would result from thermophysical or hydraulic differences between formations encountered by the GHE. Further study with the DTS system could elucidate how system temperatures develop through multiple years of unbalanced use.

Chapter 5: Discussion and Path Forward

Thermal property measurement and modeling was presented in Chapter 3, giving motivation for studying distributed temperature profiles in the subsurface. Chapter 3 demonstrates the many simplifications about the subsurface that must be made to implement a heat transfer model. Even when samples of the subsurface are available, applying laboratory tests to system design and modeling has clear shortcomings. These shortcomings are mainly related to the inherent heterogeneity of soil and rock, even within stratigraphic formations. Even if the exact distribution of thermal properties were known, no model can perfectly replicate the actual combination of thermal loads and the heat transfer process to the ground (i.e., the ground heat exchanger). However, Chapter 4 demonstrates how DTS can provide continuous observations of temperatures in difficult-to-model settings, such as GHEs.

The path forward on advancing the scientific contribution and intellectual merit presented in Chapters 3 and 4 is based on improving the implementation of DTS in GCHP systems. The beginning of this path forward is the instrumentation of a borefield for a campus-scale GCHP system, described in Appendix 1. While the DTS and energy monitoring at Grand Marsh (Chapter 4) remains useful, the plan for a DTS network in Appendix 1 includes major improvements in DTS implementation. The use of continuous fiber segments in the GHEs will allow for double-ended measurements or single-ended measurements bounded by calibration baths. This will be important for full calibration of the fibers; these calibration schemes are not possible with the current implementation of fiber described in Chapter 4. Another improvement in the path forward is the utilization of DTS fiber outside the GHE exchanger. This will allow the observation of thermal breakthrough curves as they propagate from the GHEs, ultimately providing data from which heat transfer models can be calibrated.

The final component of the path forward is a plan to create a fully controlled *in situ* experiment for GCHP heat exchange and DTS use. This plan includes a GHE instrumented with DTS in a manner akin to that described in Appendix 1; fiber optic cables would be installed in the interior of both GHE pipes and borehole grout. However, a major difference between this installation and that in Chapter 4 and Appendix 1 is that the thermal load on the GHE would be controlled for the purpose of better understanding the relationship between the environmental factors (ground temperature, hydraulic gradient, porosity, lithology) and the rate of heat transfer. Part of what makes the studies in Chapter 4 and Appendix 1 appealing is that they are "real-world" operating GCHP installations. However, this advantage also comes with the drawback that the effect of subsurface properties can be difficult to resolve through the intermittent signal of real-world thermal demands. This portion of the path forward would provide an ideal venue to control certain aspects of the in-situ heat transfer problem.

The results from DTS-based studies of GCHP performance will provide valuable inputs to modeling efforts at many scales. Boreholes with multiple DTS fibers at known locations will provide observations from which distributed heat fluxes can be calculated. Models of local GHE heat transfer, such as those employing computational fluid dynamics (CFD), could be compared and possible reconfigured or calibrated based on these observations. In-borefield, "sentry"-type DTS monitoring in the field provides an opportunity to better understand GCHP borefield design models for large commercial systems, such as those based on ILS or the duct storage model (Hellström 1989). In that case, the DTS system would be able to track the "breakthrough" of elevated (or depressed) temperature fronts throughout the long-term operation of a GCHP system with imbalanced thermal loads. Finally, temperature monitoring at piezometers outside the borefield could help track advection of heat through the borefield, assisting with the calibration of models that combine groundwater flow and heat transfer (e.g., MODFLOW with MT3DMS as a proxy for heat transfer as in Hecht-Méndez et al. (2010)).

5.1 Conclusions and Final Recommendations

DTS presents an opportunity for studying the interaction between GCHP systems and the earth with unprecedented detail. The ability to acquire spatially continuous temperature profiles at known locations in the ground is only the beginning of the observations that can be made about ground heat exchange. However, the sophistication of the DTS system presents challenges to researchers seeking to apply it in novel ways.

Permanent installations of DTS monitoring fields on a scale described in Appendix 1 represent investments of planning, time, and capital. Such projects are not possible without drilling resources, heavy construction machinery, fiber-optic technicians, and infrastructure investments in concrete vaults and conduits. To make such an investment worthwhile, researchers need the utmost confidence in their instrumentation and calibration plans.

To make the most of installed or planned DTS infrastructure, efforts should be made to gain a better understanding of the statistical population of DTS calibration parameters in controlled setting. To date, there appears to be few resources for understanding the typical ranges of the calibration parameters described in Chapter 2. Furthermore, the degree of DTS instrument drift over time is not well known. Most permanent DTS monitoring systems employed for industrial warning systems do not require the degree of precision and accuracy that environmental heat transfer modeling does (Hausner et al. 2011). As a result, researchers planning to implement a novel and spatially extensive DTS monitoring system may not be aware of the best strategy for acquiring calibration parameters.

Publishing an index of typical calibration values may not be possible since a “typical” DTS monitoring system likely does not exist. Despite this, the final recommendation for the future work stemming from Appendix 1 is to become acquainted with the calibration requirements of that particular system. Due to the sheer number of fiber segments implemented, conventional

calibration schemes like those in Hausner et al. (2011) may not be applicable. It is essential that calibration for the system in Appendix 1 produces temperature profiles of high enough quality for the desired analysis, while requiring as little calibration as possible to attain that standard.

Appendix 1: Notes on Instrumentation at Epic Systems Borefield 4

This appendix consists of a standalone memo written to summarize the first profiles of data from sentry wells at Epic, a summary of the instrumentation at Epic, and an account of the installation of DTS loops, including selected photos of the process. Instrumentation work at Epic only began within the second half of 2014. Though not an original focus of this thesis effort, managing the instrumentation installation was a major and collaborating research focus in the latter portions of this thesis effort. This appendix is intended to serve as a summary of work done to-date. Many lessons were learned during the days of fieldwork performed for the installation of a thermal-monitoring network in support of the research group's long-term vision at the site, and my hope is that future students might be able to learn from them.

A1.1 Background Temperature Measurement at Epic's Borefield #4

The fiber optic sensing network at Epic Borefield #4 features a set of six boreholes roughly 150 m (500 ft) deep called "sentry wells." Each sentry well contains a continuous optical fiber, which runs from the ground surface to the bottom of the borehole and back to the surface again. The purpose of this fiber optic network is to sense temporally changing temperature distributions across the borefield with depth. Such a network will quickly accumulate a vast amount of data about the borefield's status; each temperature measurement will be assigned a three-dimensional location within the field and the time of the measurement.

In the sentry well system's current configuration, its operation and measurement requires much more data processing than traditional plug-and-play temperature monitoring systems. However, this disadvantage is part of a trade-off that will ultimately allow users of the data to discern the health and stability of the borefield with unprecedented detail. With the background temperature measurements that have been performed, future temperature changes can be captured and compared with the borefield's operational data. Furthermore, when coupled with information

gained from piezometers located on the edges of the borefield, the network may elucidate the influence of groundwater flow (advection) as a heat transfer mechanism.

A1.1.1 Location

Epic's Borefield #4 is located on the north side of Epic's Verona, Wisconsin, campus. As shown in Figure 19, the borefield is bordered immediately to the east by the campus's North Parking Lot. To the south, development of the second Annex facility is ongoing, along with the existing Borefield #3, which also hosts a photovoltaic solar array. Farm fields border the borefield to the north and west. According to Landsat, the surface of the borefield has a significant slope, generally running from the southeast, where surface elevation is approximately 320 m (1050 ft), toward the northwest, where the field's stormwater retention pond has 295 m (969 ft) of elevation. This elevation change occurs over roughly 400 m (1,300 ft), amounting to a slope of about 3.5°. As a result of this topography, conclusions about the effect of stratigraphy on heat transfer will need to be made with respect to elevation rather than depth (i.e., two sentry of the wells will encounter the same formation at different depths). Modeling efforts will need to consider that the topography also changes the geometry of the field; the surface defined by the bottom of the boreholes will be parallel to the ground surface.

Figure 19: Aerial image of Borefield #4 obtained from Google Earth, dated June, 2014. The borefield is bordered to the east by Epic's North Parking Lot, and to the south by Borefield #3, which is covered by photovoltaic solar arrays in the image. The dimensions of the field are approximately 400-m (1300 ft) length by 250-m (820 ft) width.

The six sentry wells are spaced in an array with a longer north-south dimension than east-west, since the borefield has its longer overall dimension running north-south (Figure 20). This spacing will facilitate evenly distributed data collection such that sampling would not be biased toward one particular zone of the borefield. Each of the six sentry wells has been named to match the labels used by the Morse Group for routing the DTS fiber.

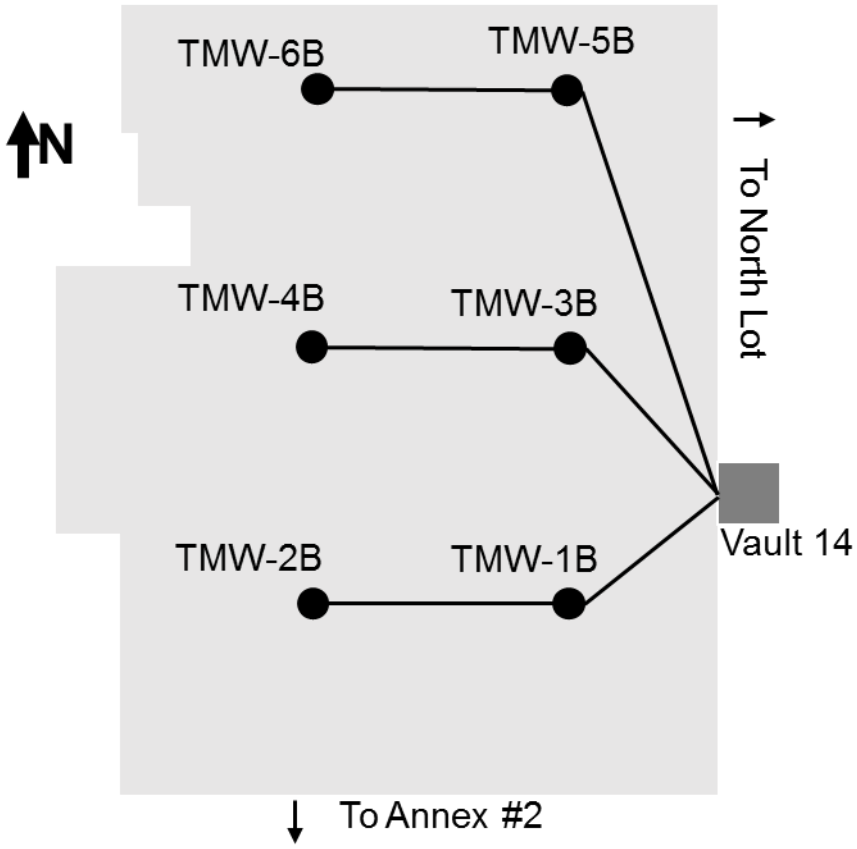

Figure 20: Schematic of Borefield #4's six sentry wells and connecting fibers.

A1.1.2 Installation

Installation of each sentry well consisted of six steps. First, 300 m (1000 ft) fiber was prepared by embedding a standard 2 mm Plenum OM2 simplex cable in a protective ¼" HDPE tube and duplexed on a spool. The HDPE tube protects the fiber as it runs to the bottom of the 150 m (500 ft) well and back to the surface again. Second, the borehole was drilled to the target depth of 150 m (500 ft). Third, the fiber loop protected by 6 mm (¼") HDPE must be dropped to the bottom of the borehole. This step was accomplished through the use of a weighted "torpedo" affixed to the bottom of the loop and sent down with a weight bar. Once the weight bar is brought back to the surface, the well was completed by grouting the fiber in place. During this step, care is taken to protect exposed fiber during casing removal. The final step was fusing fiber from the well into a length of fiber cable with carries the well's signal back to the main

monitoring vault, Vault 14 (see Figure 20). This final step was accomplished after the sentry well head was secured in a 1.2 m x 1.2 m x 1.2 m (4 ft x 4 ft x 4 ft) precast concrete vault.

Each pair of sentry wells on an east-west line forms a single loop connected through fiber lines running between vaults (Figure 21). Each loop has two connecting cables: one running from Vault 14 to the easternmost sentry well of the loop and one running between the sentry wells. Each connecting cable has six fibers, though only two are used in the case of the sentry wells. One fiber carries the DTS signal to the wells, and another carries the signal back.

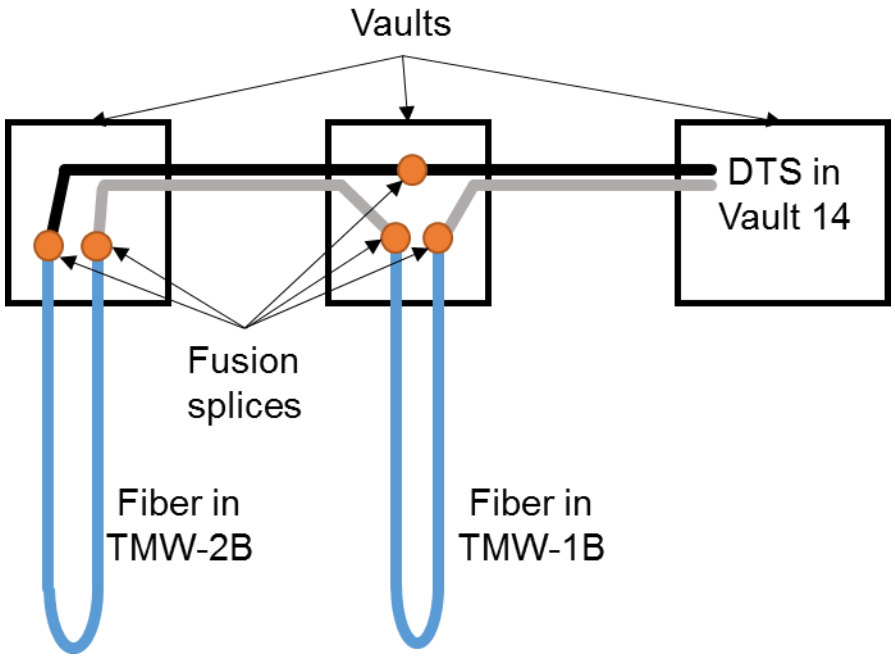

Figure 21: Schematic of the fiber loop joining the fibers embedded in TMW-1B and TMW-2B to the DTS interrogator in Vault 14.

As of the date of this document's creation, five of the six sentry wells had been drilled with their fiber loops embedded. The only remaining borehole to be drilled is for TMW-5B. TMW-6B did not fully reach its target depth due to collapse within the deep sandstone formations during drilling. Currently, TMW-1B and TMW-2B have been linked through fiber lines to comprise the first sensing loop. The other two loops have yet to be completed.

While the fiber comprises one part of the sensing system, the DTS interrogator is the other part. The interrogator is essentially a computer that houses additional laser and receiver hardware in a standard 48 cm (19”) server case. For the initial measurements made at Borefield #4, a Halo DTS interrogator by Sensornet, Ltd. was installed in a server enclosure Vault 14. A more accurate interrogator, the Sentinel DTS (also by Sensornet Ltd.), has been ordered and will permanently replace the Halo DTS in Vault 14 upon its delivery, expected in early 2015. In addition to being more accurate than the Halo DTS, the Sentinel DTS can also interface with a 16-channel multiplexer to take all planned DTS measurements at Borefield #4 (sentry wells, instrumented borehole heat exchangers, and piezometers).

A1.1.3 DTS Basics

DTS is a measuring technique that utilizes the fiber-optic cable to measure temperature along continuous profiles. The application of this technology has been rapidly expanding in both industry and academia due to inherent advantages over networks of conventional temperature-logging sensors (e.g. thermocouples, thermistors, and other temperature detectors). Instead of having discrete sensors which transmit their signal through wires, a DTS interrogator utilizes the entire length of connected fiber as both a sensor and a transmitter of the signal.

Fiber-optic sensing systems generally function by shooting laser light pulses through an optical fiber and analyzing backscatter of this light as it relates to differing physical conditions. This backscatter forms as a result of incident light striking slight imperfections in the fiber’s glass core. DTS at Borefield #4 specifically utilizes Raman backscatter. Raman backscatter is inelastic; backscattered light shift to either higher or lower wavelengths than the incident light. The higher-wavelength component of the inelastically scattered waves is the Stokes component, whereas the lower-wavelength component is the anti-Stokes component. Of all backscatter spectra, anti-Stokes Raman backscatter is, by far, the most temperature-dependent. As a result, the ratio of anti-Stokes intensity to Stokes intensity at given locations in

the fiber relates to the fiber's temperature through calibration processes. DTS devices know the location of signals emitted from locations along the fiber due to the travel time of light through the fiber.

A1.1.4 Data Collection

Users of the system have many options for collecting and interpreting data from the DTS system at Epic. One important choice to be made is whether to collect, calibrate, and interpret temperature in single-ended or double-ended measurements. Single-ended measurements connect to the DTS interrogator with only one connector, and double-ended configurations connect to the interrogator with two connectors. Double-ended measurements have the advantage of better accounting for attenuation of signals along the cable. All of the temperature-sensing loops at Borefield #4 were installed as complete loops, beginning and ending at vault 14. Therefore, double-ended measurements are the suggested means of data collection, so long as there are enough interrogator channels available for the desired measurements; the Halo DTS system has a 4-channel multiplexer, while the Sentinel DTS systems will have a 16-channel multiplexer. In single-ended configuration, the devices have capacity for as many loops as they have channels, but, in double-ended configuration, the capacity is halved (2 on the Halo DTS system, 8 on the Sentinel DTS system).

Another choice to be made is whether the temperature data should be calibrated and collected solely by the manufacturer's software or if the data should be post-processed for data afterwards. Since programming scripts need to be used to manage the vast amount of data produced by DTS system, the user would not need to invest much more time to implement post-processing scripts. The benefits of post-processing include more flexibility in choosing calibration method and better understanding of *how* temperature measurements are obtained from raw measurements. To calculate temperature from raw data, users can refer to Hausner et

al. (2011) for single-ended measurements and van de Giesen et al. (2012) for double-ended measurements.

A1.1.5 Results

On November 4, background temperature measurements were taken on the first sentry well loop, consisting of the fiber at the TMW 1B and TMW 2B boreholes. These measurements preceded the activation of Borefield #4's phase 1 and represent the background temperature on site. Examples of the full temperature measurement profiles taken by the DTS system are shown in Figure 22 and Figure 23. Both of the displayed profiles are single-ended measurements from the Halo DTS interrogator temporarily positioned in Vault 14. Both profiles were acquired with 20-min integration times.

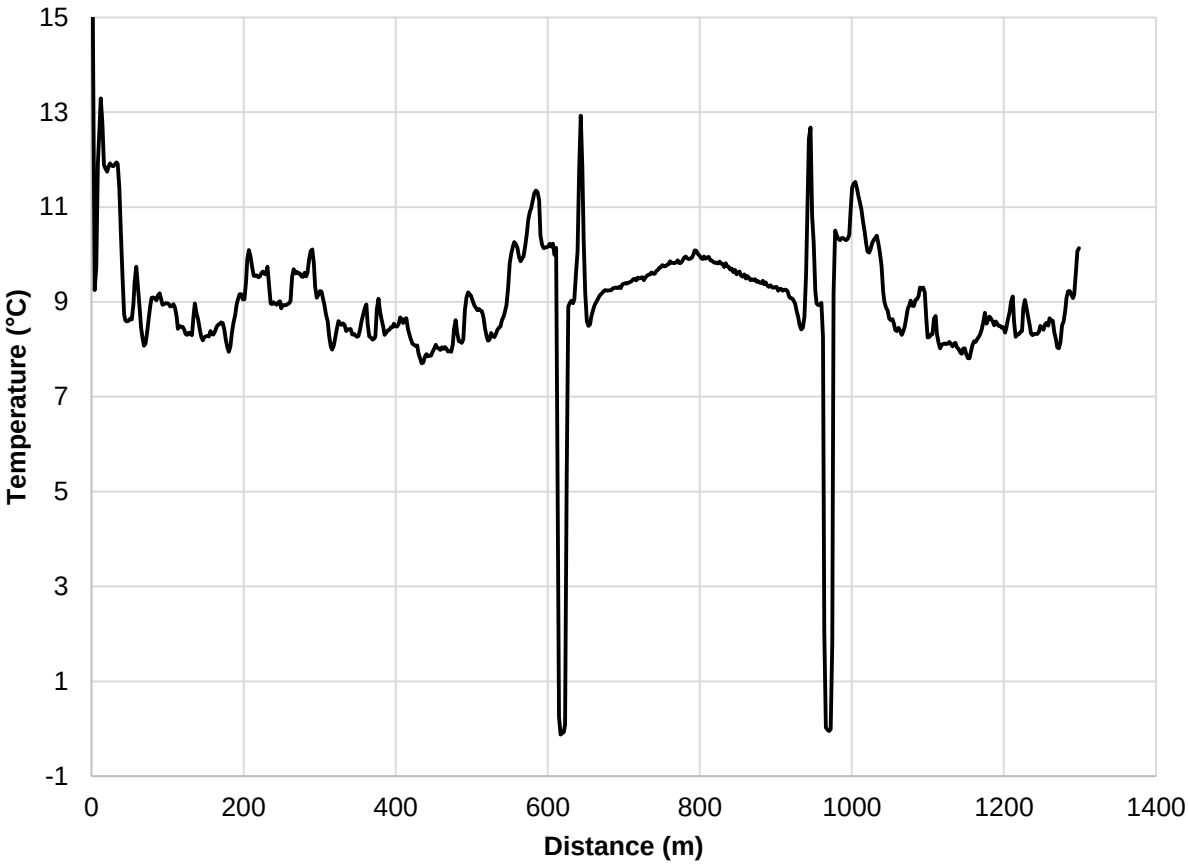

Figure 22: Full profile of temperatures collected on the TMW-2B fiber, the southwestern sentry well. The section of interest is in the middle of the profile, displaying a mirrored geothermal gradient within the borehole. Other points of note include the ice-filled calibration bath on either side of the borehole profile

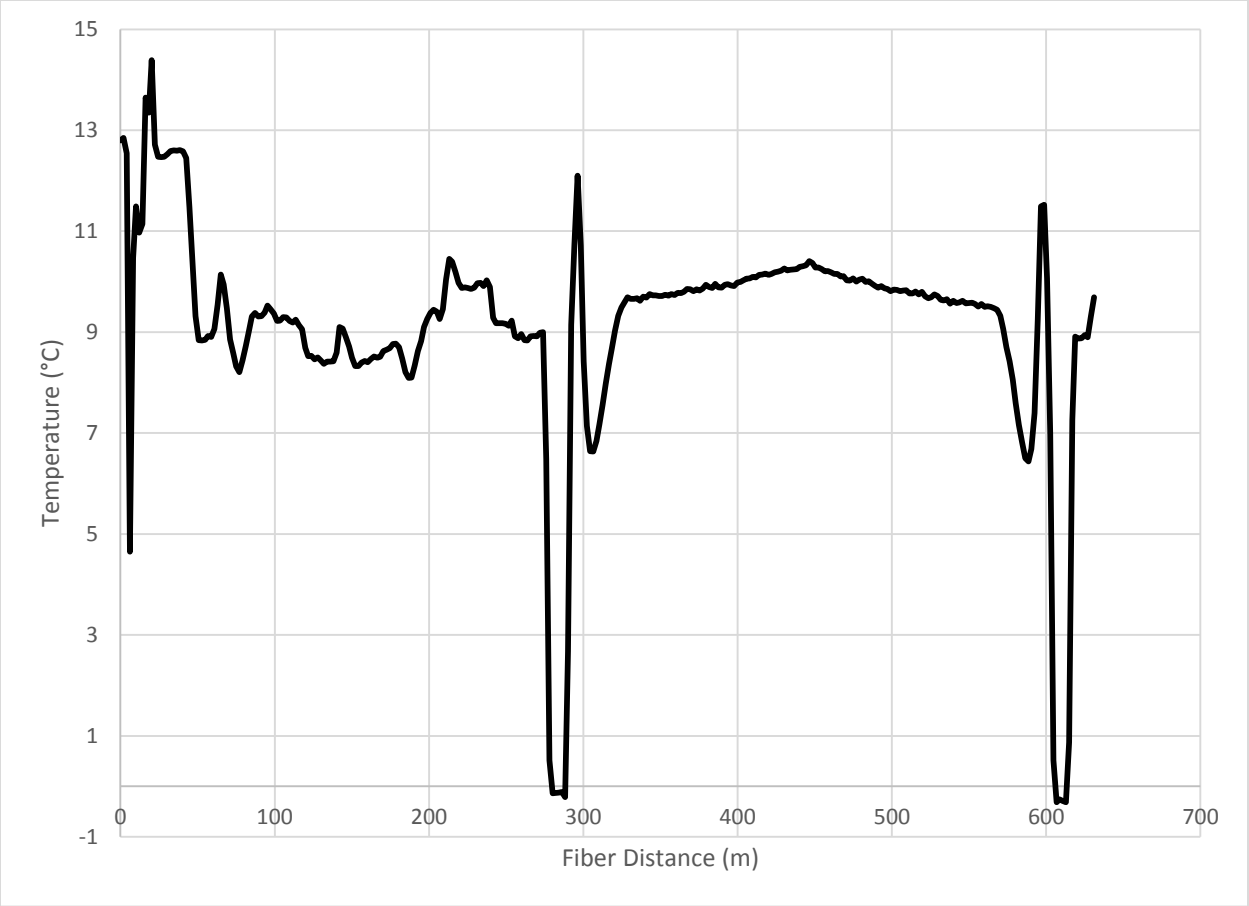

Figure 23: Full profile of temperatures collected on the TMW-1B fiber, the southeastern sentry well. The section of interest is in the middle of the profile, displaying a mirrored geothermal gradient within the borehole. Other points of note include the ice-filled calibration bath on either side of the borehole profile

After obtaining the full profiles, the data was trimmed to only match the sections we are interested in: those within the boreholes. Additionally, the temperatures were averaged at matching depths since two matching temperature profiles are available at each well. In other words, the reported value at a given depth is the average of the “mirrored” pair of borehole profiles. Figure 24 shows the results of this processing for the TMW 1B (the southeast well) and TMW 2B (the southwest well).

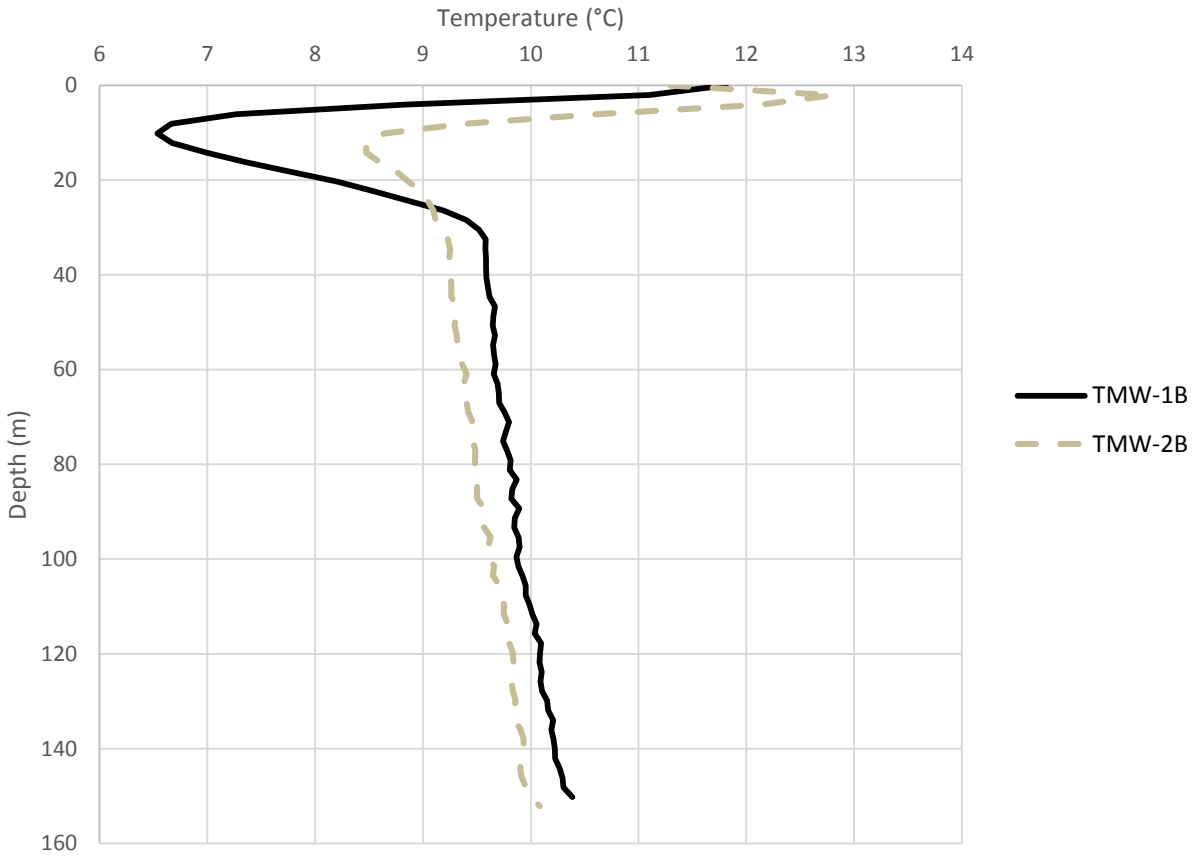

Figure 24: Trimmed and processed profiles for temperatures within TMW-1B and TMW-2B. Temperature and gradients for the profiles are consistent with expected values for Wisconsin's aquifers. A slight gradient shift at about 100 m (325 ft) depth may correspond to a shift in thermal properties.

A1.1.6 Discussion

The background temperature profiles at Borefield #4 will provide a reference point for future temperature changes at the site. The two sentry wells that have been logged are consistent in their gradients. Temperatures in Borefield #4 are cool, though within the range typically expected in Wisconsin's aquifers, roughly 8 °C to 11 °C (47 °F to 52 °F) (Hennings and Connelly 1980). The thermal gradient of about 150 m/°C (270 ft/°F) is low relative to the US average but is typical for Wisconsin's aquifers. Cool temperatures, low gradients, and transmissive aquifer materials are ideal for keeping borefield temperatures low when the system is cooling-dominated, as Borefield #4 is expected to be for the majority of a typical year.

A1.1.7 Future Work

In the following weeks, we will collect data and report on the changes in sentry well temperature after about a month of operating Borefield #4's phase 1. However, large changes to the profiles are not expected as the load applied to Epic's heat exchange system is minimal during winter months. Furthermore, winter is the optimal season for heat rejection in Epic's pond heat exchange loops, located in stormwater management ponds on the campus. By obtaining temperature data within the geothermal exchange pipes of two GHEs in Borefield #4, we may discern the extent to which heat is being absorbed or rejected by the system. When coupled with Borefield #4's operational data, especially during periods of higher thermal loads, these data sets should allow us to identify the most productive formations for heat transfer, a major focus of this study overall.

A1.2 DTS Instrumentation at Borefield #4

The instrumentation at Epic is aimed at a number of research questions related to the use of a campus-scale borefield. A campus- or district-scale borefield is one with hundreds of boreholes to provide space heating and cooling for large buildings or entire campuses. The main question of serviceability for such borefields is related to the long-term sustainability of their use. In other words, to what extent do borefields lose performance over time, and how can such outcomes be ameliorated or prevented? Additionally, there are questions about the role of site hydrogeology on heat transport in a large borefield like those at Epic. A separate, but related, question exists about whether elevated temperatures in the subsurface introduced by the borefield could potentially alter chemistry of aquifers intersected by the boreholes.

To address these questions, an extensive DTS network was devised for installation in Epic's Borefield #4. Many details of the borefield, especially the sentry well network can be found in Section A1.1. Besides the six sentry boreholes described therein, five wells external to the borefield were planned for hydraulic sampling and external temperature sampling. Additionally two heat exchange wells were instrumented to decipher changes in temperature within the heat exchange pipes and borehole grout. These two exchange wells also serve as a comparison between two GHE types: u-tube and coaxial. U-tubes are considered the "traditional" technology for GHEs, while coaxial pipes have gained favor in certain realms for potentially having more heat exchange effectiveness (Acuña and Palm 2010; Acuña and Palm 2013; Beier et al. 2012). By installing and instrumenting a GHE of each type on the same water supply line within the same borefield, the efficiency of each can be compared, side by side.

A1.2.1 Current Status of Instrumentation

At the time of this thesis's publication, nine of thirteen planned instrumented boreholes had been drilled (Figure 25). This includes five of six sentry wells, one of five exterior groundwater monitoring wells, and both of the two instrumented heat exchange wells. As mentioned in

Section A1.1, the two southernmost sentry wells had fiber installed within them and have been connected to Vault 14. The exchange wells have also been connected to Vault 14. In total, four loops are currently being monitored: the south sentry loop, the coaxial pipe loop, the loop within the u-tube, and the loop within the grout of the u-tube. By the time the project is completed, there will be eight loops to monitor.

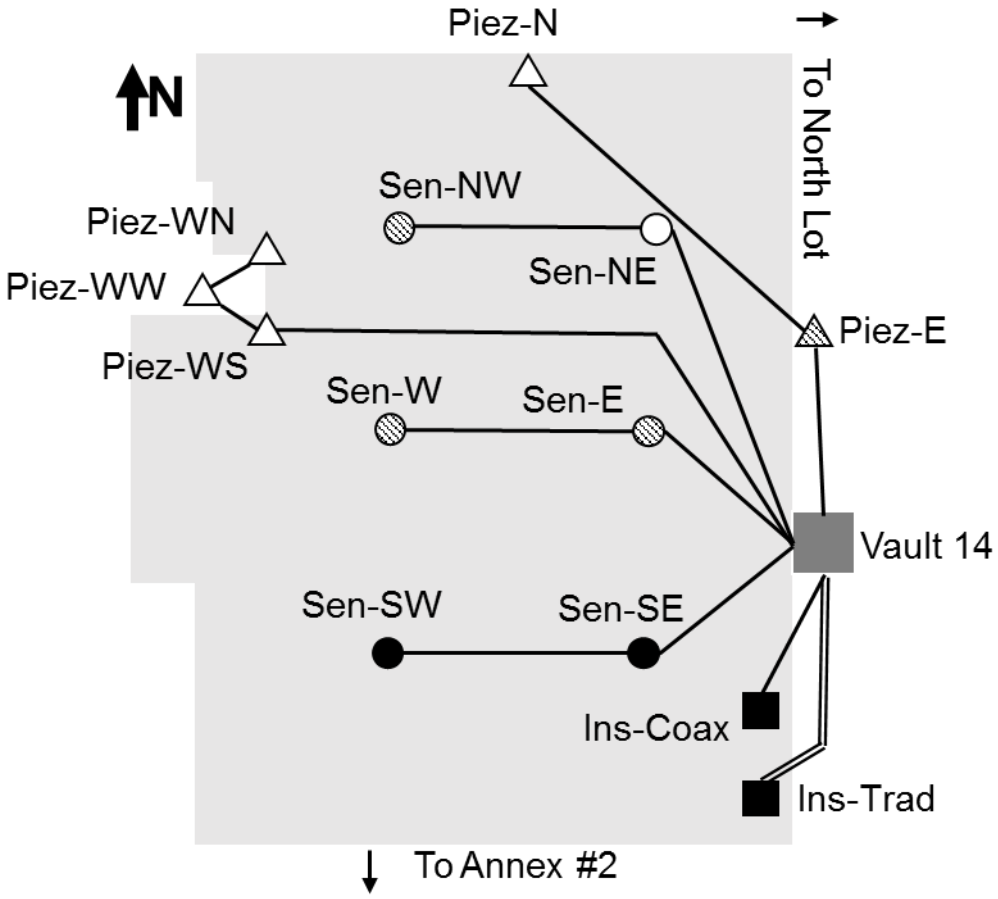

Figure 25: Schematic (not to scale) of Borefield #4's instrumented boreholes. Circles represent sentry wells, triangles represent groundwater monitoring wells, and squares represent instrumented exchange wells. A line connecting one or more wells to the monitoring vault, Vault 14, represents a connecting loop of fiber (see Figure 21). Filled shapes are installed wells which have been connected to Vault 14 and are currently monitored. Pattern-filled shapes indicate drilled wells that do not yet have fiber connections to Vault 14. Open shapes represent planned boreholes, which have yet to be drilled.

Based on the discussion in Section A1.1.6, monitoring Borefield #4 will then require an eight-channel DTS system in single-ended configuration or a sixteen-channel DTS system in double-ended configuration. Currently, a four-channel Halo DTS system (Sensornet Ltd, Hertfordshire, UK) is installed to monitor the four connected loops in single-ended configuration. This DTS system is mounted within a steel National Electrical Manufacturers Association (NEMA)-approved enclosure on the south wall of Vault 14 (Figure 26). The enclosure is not air-conditioned, but the vault typically maintains a cool, steady temperature, which is apparent from the record of the DTS interrogator's interior temperature (Figure 27). As mentioned in Chapter 2, great swings in ambient temperature within the interrogator's housing should be avoided as they can create errors in the DTS system. To date, this mounting solution appears to be adequate for holding a steady temperature around 30 °C.

Figure 26: Halo DTS interrogator as installed in a NEMA enclosure in Vault 14 on December 3, 2014. Four E-2000 APC connectors are connected at the top left of the interrogator.

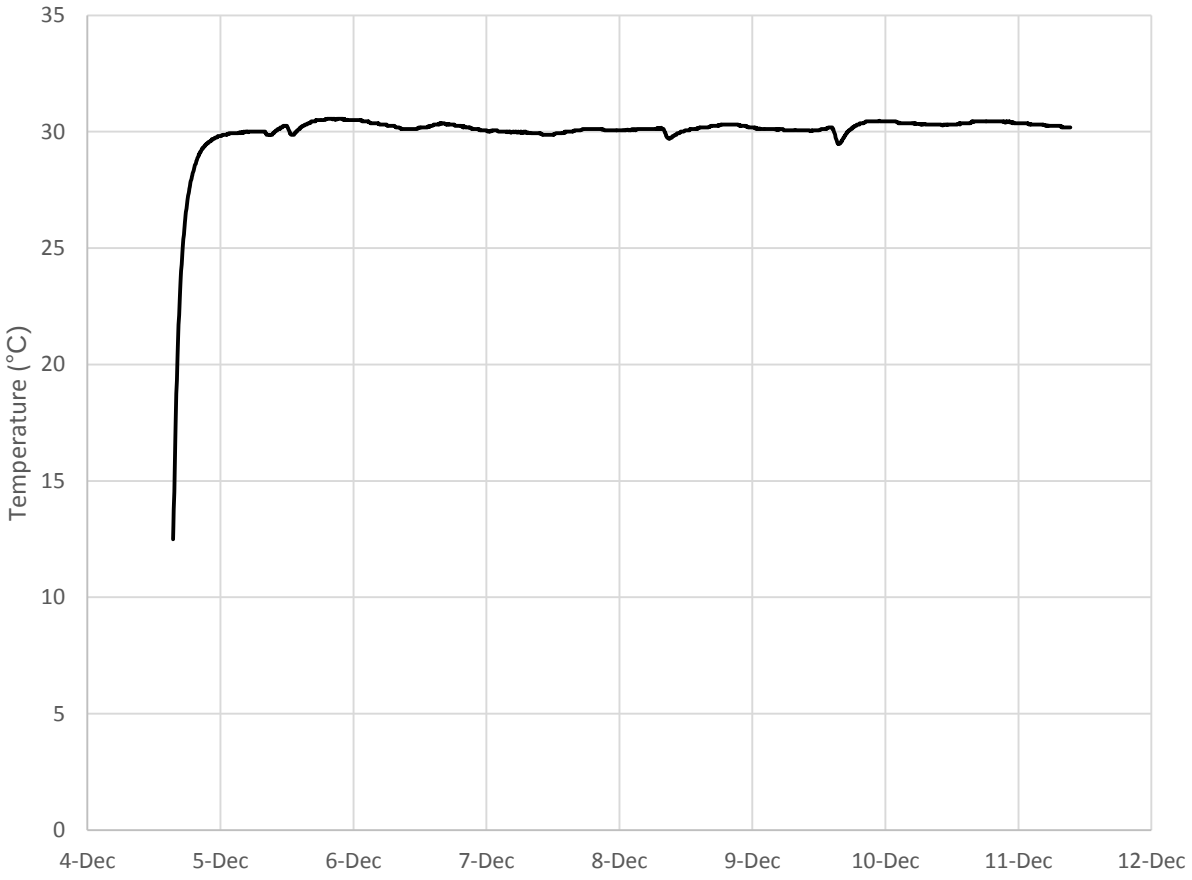

Figure 27: Record of interrogator interior temperature during a week of continuous DTS use within Vault 14. This temperature is used as a reference by the DTS interrogator's Raman backscatter acquisition software, and large swings in temperature can create errors in the raw Stokes and anti-Stokes signal.

A1.3 Installation of Fiber Loops at Borefield #4

A1.3.1 Groundwater Monitoring Well

The first well drilled specifically for research at Borefield #4 was the eastern groundwater monitoring well. Two piezometers and one blank were installed in the well. The blank is a plastic pipe without screening in which fiber optic cable will be placed for monitoring. The piezometers were installed so that hydraulic head can be measured in the two aquifers intersected by the boreholes on the site and water quality changes, if any, can be noted. Figure 28 shows this well nest during a temporary DTS test on the blank.

Figure 28: Easternmost piezometer nest during a temporary DTS test of the blank, which is labeled “DTS” in the photo.

Though there are currently no permanently installed fibers at this borehole, there are plans to add them once the sentry wells are completed. Plans for the placement of DTS fiber within groundwater monitoring boreholes will need to be different from the other boreholes monitored at Epic because the diameter of the blanks is 5 cm, which is less than the minimum turn distance that can be accommodated by the protective HDPE tubing, which is used with the fiber in the other wells.

A1.3.2 Sentry Wells

After the first groundwater monitoring well was installed, sentry wells were drilled. As briefly described in Section A1.1, the sentry well drilling and DTS installation process began with preparing 2 mm OM2 simplex fiber optic cable by protecting it within ¼" HDPE tubing. This process was accomplished by first rolling out a 600 m spool HDPE tubing to its halfway point, which is double the target depth of the sentry wells (150 m). The tube was then cut taking care to keep hold of pull string which had been shipped within the HDPE tube. The fiber optic cable could then be knotted with the pull string and pulled through the entirety of the 300-m tube. The fiber spool itself was sized to leave approximately 30 extra meters of fiber on each end of the tube (360 m total) for calibration and splicing. The extra fiber was pulled ensuring that it was evenly divided. After this, the two ends of the tube were joined to form a "duplexed" loop that could be taped together at regular intervals. After taping, the tubing was rolled back onto a spool with the ends rolled-on first.

The prepared roll of tubing-encased fiber was transported to the recently drilled borehole where it was fitted to a metal torpedo along with the drill rig's weight bar (Figure 29). Special care had to be taken to ensure that the entire setup was heavy enough to counteract any buoyancy from the air-filled HDPE. The torpedo was carefully affixed to the weight bar with duct tape (Figure 30) so that the weight bar could guide the fiber to the bottom without applying tension on the fiber itself. During this process the torpedo would occasionally catch on the borehole wall, especially in karst zones, so care had to be taken not to get the assembly stuck midway down the hole. Once the torpedo and fiber had reached the bottom of the borehole, the weight bar was lifted back to the surface by applying enough force to pull away from the torpedo. After the weight bar has been returned to the surface, the tremie pipe was lowered to grout the borehole. Karst features presented issues to grouting on many boreholes at the site, necessitating greater amounts of casing and larger volumes of grout. Occasionally pea gravel and bentonite chips

had to be used to fill particularly troublesome voids. For all instrumented boreholes, pulling the casing from the borehole was a delicate process. The calibration loops (the extra 30 m of cable on each end of the protective tubing) were coiled at the ends of the HDPE tubing. This fiber was exposed to the rough metal interior of the casing as it was lifted above the tubing sticking out above ground level.

Figure 29: Torpedo being prepared for the installation of the instrumented u-tube heat exchange well. This photo is also representative of the torpedoes used on the sentry well fibers, though those obviously did not include heat exchange pipe as in this photo.

Figure 30: Coiled fiber protected in HDPE tubing is affixed to rig weight bar before being dropped to the bottom of sentry well TMW-2B.

A1.3.3 Coaxial Instrumented GHE

After completion of the sentry wells, the coaxial-instrumented exchange borehole was drilled. The coaxial system consists of a 9-cm-diameter fiberglass composite pipe with a PVC/rubber composite tube suspended on the inside of the composite pipe. During operation of the GHE, water flows down the inside rubber tube and returns upward in the annulus between the composite pipe and the tube. To assess the performance of this alternate GHE design, DTS fibers were installed within it. However, the coaxial GHE's alternate design meant that certain alterations had to be made to the instrumentation installation. Foremost, the fiber could not be encased within an HDPE tube as for the other wells due to the sharpness of the turnaround at the bottom. This meant that fiber protected only by its polymer jacket had to be used within the GHE.

After drilling the borehole, the installation process began by chemically bonding sections of the fiberglass pipe and sending them down the borehole successively (Figure 31). Next, the inner tube was laid out so that fish-tape could be used to place a continuous segment of pull-string inside it (Figure 32). After that, the fiber was pulled through, and doubled back up the outside of the tube where it was affixed to standoffs that centralize the inner tube within the fiberglass outer tube. Once this was completed, the tubing was sent down the outer tube, and the outer tube was grouted in place (Figure 33).

Figure 31: Fiberglass outer pipe of the coaxial GHE within the borehole casing before inner tubing was installed.

Figure 32: Laying out sections of the inner tube for the coaxial GHE before fiber was strung through the inside and wrapped on the outside.

Figure 33: Inner tube of the coaxial system placed within the fiberglass outer pipe while the outer pipe is grouted within the borehole (tremie pipe in red). Fiber travels down the inside of the tube and back up the outside. Excess fiber (orange) was wrapped on the end of the tube and later covered to protect it from the rough edges of the steel casing as it was pulled.

After grouting, which was done painstakingly due to issues with karst as described in Section A1.3.2, an excavator dug out space around the pipes so that a vault could be placed atop the wellhead (Figure 34). A similar excavation process was eventually employed at all of the active DTS monitoring boreholes so that the fiber could be calibrated and fused in a protected environment. At the coaxial well, the exchange pipes had to be trimmed (Figure 35) so that they could be connected into the headers that carry the heat exchange fluid to and from the GHE (Figure 36).

Figure 34: Excavating around the GHE to make room for the vault and well-head (~2 m depth).

Figure 35: Careful trimming of the pipes for the GHE. Special care had to be taken to only cut the pipes and not the fibers. After the pipes were cut in a horizontal plane, they were cut in the vertical plane so that the excess fiber could be pulled out.

Figure 36: Stringing fiber through coaxial wellhead before permanently fusing to the GHE.

A1.3.4 U-tube Instrumented GHE

Preparation for the installation of the u-tube instrumented GHE began similar to the preparation for the sentry wells; fiber was strung through a protective layer of ¼" HDPE. However, this process was complicated by the need to place the fiber and protective tubing within the u-fitting for the 3.2-cm HDPE piping. This step was accomplished by stringing the fiber through three components separately. First, the u-fitting was preassembled by placing a short section of the ¼" tubing inside the u-fitting. A heat gun had to be used to reduce the stiffness of the materials. Then two 150-m sections of tubing were laid out. Fiber was passed first through one 150-m section of tubing, then through the u-fitting, and last sent through the remaining 150-m section

of tubing. The sections were connected together with short sections of copper pipe whose joints were protected with a double layer of shrink-wrap.

This entire assembly was pulled through parallel 150-m sections of the 3.2-cm diameter GHE pipes. As was the case for all other instrumented boreholes, it was important to protect the extra 30 m of fiber optic cable on each end of the protective tubing. In this case, the fiber had to be protected from damage as the tubing was pulled through the GHE pipes. This was accomplished by allowing the fiber to follow behind the tubing as it was pulled through the GHE pipes (Figure 37). After pulling through the assembly, the u-fitting was fused to the GHE pipes with electrofusion couplings because the typical butt-fusion would melt the fiber optic cable within. All of the components were then pressure tested for 2 hours at 700 kPa air pressure. After pressure testing, the pipe was rolled onto a spool and transported to the borehole.

At the borehole, the end of the u-fitting was attached to a torpedo as with the sentry wells (Figure 29). Two additional “sentry loops were also attached to this torpedo to accomplish the goal of measuring temperature within the grout of the borehole. Before sending the assembly down the hole in a fashion similar to that of the sentry well installation (Section A1.3.2), the GHE pipe had to be filled with water so that it would sink within the water-filled borehole. Unfortunately, the presence of the fiber loops made it impossible to attach the drillers’ standard couplings for their water pipe, and a more rudimentary setup using tape and rags had to be used to ensure that water filled the entire spool of pipe. The torpedo was then lowered slowly down the borehole. The borehole was then grouted. It should be noted that the external DTS loops for monitoring grout temperature were not positioned in certain sections of the borehole as originally desired.

Figure 37: Pull string being taped to the fiber's protective tubing. The excess calibration fiber was allowed to trail behind the pull string as the tubing was pulled through.

A1.4 Data Collection and Future Work at Borefield #4

Before data collection could proceed, the fiber loops within completed boreholes across the site had to be spliced into fibers connecting the boreholes to one another and to Vault 14 as described in Figure 25. Technicians from Morse employed fusion splices for their low signal losses, despite being a time-consuming and complex process, one especially difficult to complete in cold and windy conditions. The set of fusion splices at each borehole was protected from any potential future damage by securing them in an enclosure (Figure 38). The integrity of

the fusion splices was checked with the Halo DTS from Vault 14. Any faults in the fusion splices were fixed. However, one fault currently remains in the cross-over connection between the grout fibers of the u-bend borehole.

Figure 38: Photo of fusion splices as they appear in their enclosure at TMW-1B.

Data collection on the four active DTS loops at the site necessitated two calibration baths at the top of each borehole examined. This allowed four calibration sections on the fiber in each borehole, just as suggested by Hausner et al. (2011). To create sufficient temperature contrast to properly invert for the calibration parameters, warm water bath and one cold water bath were used. The warm water bath was created by simply filling water coolers with hot tap water, while the cold water bath was created with a mixture of ice and water. Each 30-m section of fiber at the end of the sensing loop described in section A1.3.2 (Figure 39) was split into two 15-m

sections. By doing so, each end of the fiber sensing loop could be immersed in each of the water baths for the duration of the first measurement period (~1 week) (Figure 40). Independent temperature measurements within the baths were taken with a Platinum Resistance Temperature Detector (PRTD) on a Levelogger (Solinst Ltd.) for the duration of the test. These measurements were in-turn verified with the use of an alcohol thermometer at the beginning and end of the test.

Currently, there are no options for remote retrieval of data from the DTS interrogator; data sets must be downloaded onto a USB storage device manually in Vault 14. Data sets are in the form of tab-delimited text files and must be processed as described in Section 2.4. Due to the vast quantities of data produced by the system the processing is best done with scripts. With the interrogator set on a 1-minute repeat cycle, a separate text file of data is generated every minute. Along with the calibration script mentioned in Section 2.4, CTEMPS also has created a Matlab script to convert the text file data produced by the interrogator into a more manageable data matrix. This script was employed to create the data sets that were then used as inputs for the calibration script (Appendix 2). Figure 2 is the very first temperature profile generated from the data collected at Borefield #4 as described in this work.

Figure 39: An example photo of the wellhead vaults employed at Borefield #4. This photo was taken at the coaxial GHE wellhead. The black pipe carries supply and return water to and from the coaxial GHE. The black tubing caries the fiber out of the GHE to the fusion splice panels. The opening is a standard manhole (~1 m). The floor is slightly larger at 1.2 m x 1.2 m.

Figure 40: A photo representing a pair of calibration baths at Borefield #4. This particular pair is located in TMW-1B.

Future work at Borefield #4 will feature improved interrogators and continued progress toward installing all of the fiber loops described in A1.2. A Sentinel DTS interrogator (Sensornet Ltd., Hertfordshire, UK) will replace the Halo DTS interrogator (Figure 26) currently collecting data in Vault 14 from the first four fiber loops. The Sentinel features improved spatial resolution, and it will be combined with a 16-channel multiplexer to allow double-ended measurements on all eight loops. The interrogator and its multiplexer will be housed in an air-conditioned server rack for a stable measurement environment. Additionally, the interrogator will be connected to internet for remote access and control.

As alluded to in Section 5.1, some of the largest obstacles to the most efficient operation of the DTS system are related to calibration. The delivery and installation of the Sentinel DTS will provide an opportunity to reevaluate the best methods of obtaining the required post-processing parameters. The method of data collection and calibration described in this section may be unsustainable as more DTS fibers are brought online.

Only monitoring baths at Vault 14 may be one solution to the monitoring problem. This would involve continuous monitoring of the calculated C and γ (described in Section 2.4) for each profile to account for temporal instrument drift for those parameters. The parameters could then be used in dynamic calibration of the temperature profiles (i.e., the calibration parameters are updated for every DTS measurement). The advantage of this strategy is that the calibration involves a maximum of 32 calibration sections (four sections for each of eight loops) in two well-controlled baths rather than 60 sections (four sections for each of 15 vertical monitoring loops) split between 26 baths in 13 vaults. Using a calibration strategy with only centrally-located baths would assume that the parameters can be applied to the entirety of each profile.

γ and C are theoretically constants, but they can be adjusted over time to account for changes in the interrogator's sensitivity to Raman signals. This sensitivity is most notable during especially rapid or marked changes in the interrogator's internal reference temperature (Tyler et al. 2009). Even if DTS interrogator is in a location with stable temperature, it is prudent to continue checking on the γ and C values throughout a long-term measurement. Based on the fact that C and γ are mostly dependent on the interrogator and quantum physics, respectively, the calculated values could then be applied to the entirety of the Raman backscatter profiles to calculate temperature.

While this strategy is valid for C and γ, accounting for differential attenuation remains an obstacle because differential attenuation varies predictably (as governed by Beer's Law,

Equation 6) and unpredictably (at discontinuities in the fiber like connectors or fusion splices). Accounting for differential attenuation still would require at least one field calibration for each of the 15 vertical monitoring loops in their individual vaults. The differential attenuation parameter would be a static (one-time) calibration, used in conjunction with the other dynamically calculated parameters for long-term measurements. Using a static calibration for the differential attenuation factor is only valid under the assumption that differential attenuation will not change over time. This is not completely true since a change in tension or other force on the cable could affect the attenuation, but the magnitude of these considerations is expected to be small enough to neglect.

Appendix 2: Matlab Script for Post-Processing DTS Data

```
% ProcessEpic_Sentry
% Script by Matthew Walker mdwalker@wisc.edu
% Takes raw Stokes and AntiStokes from Epic Halo DTS and combines with
% independent temperature observations for calibration

% Calibration is performed through a least squares inversion of an
% overdetermined matrix

% Strategy is based in part on Hausner et al. 2011 and ProcessSensornet.m
% from CTEMPS is used to generate the input.
% Sincere thanks to CTEMPS for their work.

clear all
close all
clc

%% Load data
load('120414_C4_4.mat')
CalTemp(1:length(distance)) = 0; %Placeholder matrix
params(1:3,1:length(Stokes(1,:))) = 0;
p = 1; %Which profile to calibrate
    S = Stokes(:,p); % Stokes vector
    A = AntiStokes(:,p); % Anti-stokes vector

    %% Plot sample temps
    plot(tempC) %Use the plot of the Sensornet output to find reference
sections/baths

    %Mark down the reference sections such that each the first column
represents
    %the beginning and of the reference section
    %respectively.  In the example below, reference section 1 goes from
    %index (304) to index (308).

    %In current configuration TMW 2B is the first 4 baths
    refs(1:8,1:2) = [303,308
        311,314
        470,474
        477,482
        663,667
        670,675
        830,835
        838,843];


    %% Explicit Calculation of Calibration Parameters (Method 2.1 in Hausner)
    %Enter the reference section temperatures that correspond to the
    %indices entered above.  In this example, the first reference section
    %(from index n1 to x1) is 0C (or 273.15 K)

    refT = [2.21 + 273.15
```

```
        35.872 + 273.15
        35.872 + 273.15
        2.21 + 273.15
        33.85 + 273.15
        0.92 + 273.15
        0.92 + 273.15
        33.85 + 273.15];


    %For calculation, each reference section temperature needs to be
    %assigned a distance value. We use the midpoints.
    z(1:length(refs),1) = 0;
    for i = 1:length(refs)
    z(i) = (distance(refs(i,1))+distance(refs(i,2)))/2;
    end

    %Build the "G" matrix for the solution of the inverse problem according
    %to Method 2.1 of Hausner
    G(1:length(refs),1:3) = 0;
    for i = 1:(length(refs))
        G(i,1:3) = [1/refT(i), -1, z(i)];
    end
    %Build the "data" vector from 2.1 of Hausner
    b(1:length(refs),1) = 0;
    for i = 1:length(refT)
        b(i) = mean(log(S(refs(i,1):refs(i,2))./A(refs(i,1):refs(i,2))));
    end


    %Solve the inverse problem. Left divide used here for least squares.
    m = G\b;

    %% Calculation of temperatures
    for i = 1:length(distance)
        CalTemp(i) = m(1)/(log(S(i)/A(i))+m(2)-m(3)*distance(i)) - 273.15;
    end
CalTemp = real(CalTemp);

%% Plots

close all
figure
plot(distance,CalTemp,'r')
hold on
plot(distance,tempC(:,p),'b')
title('Temperature Profile for Sentry TMW-2B')
ylabel('Temperature (C)')
xlabel('Distance from Interrogator (m)')
axis([0 2000 -5 45])

%% Save Data
save Chan1Cfg2Proc.mat
```

Appendix 3: Geophysical Log for Grand Marsh Study Site

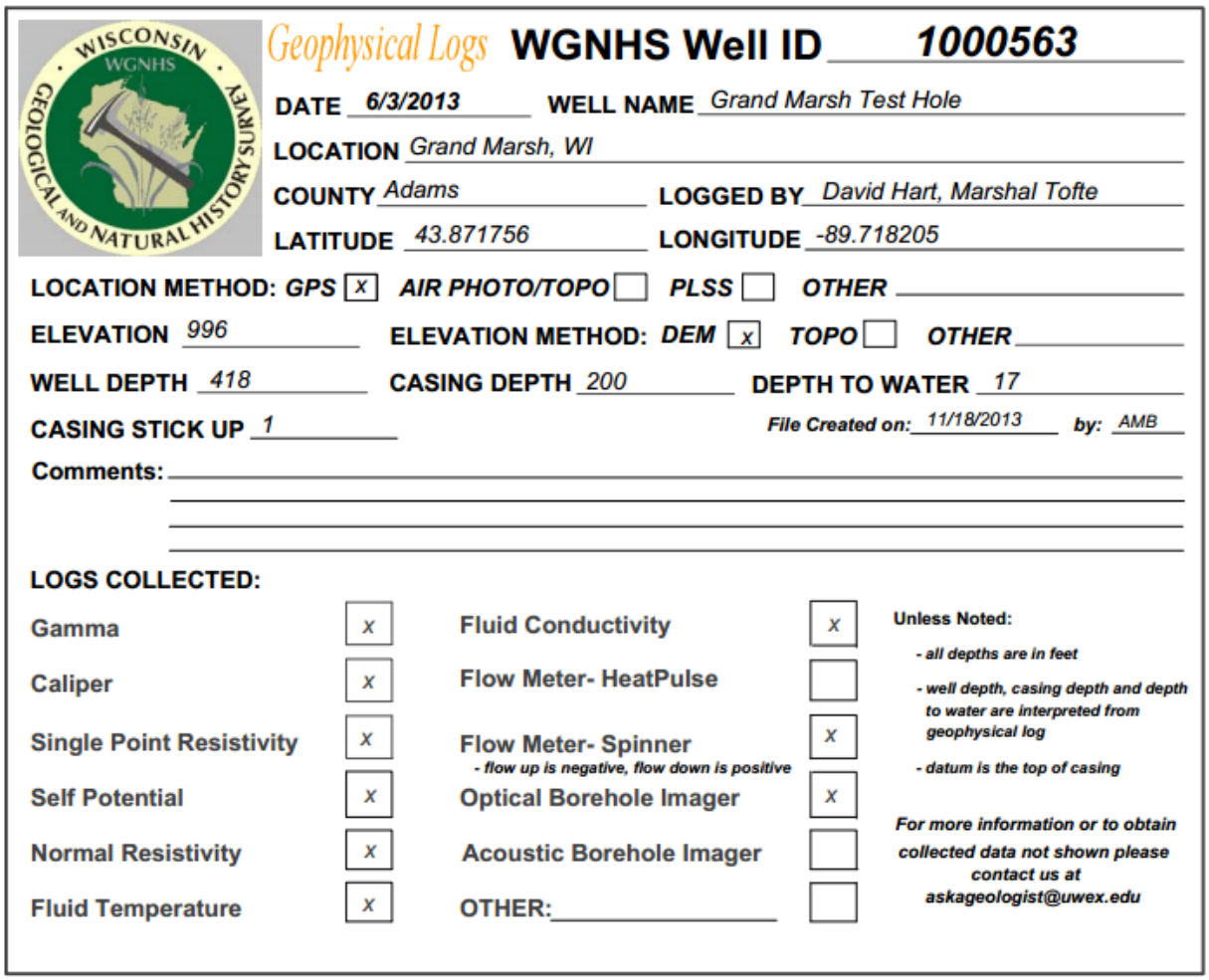

Geophysical Logs **WGNHS Well ID** 1000563

DATE 6/3/2013 **WELL NAME** Grand Marsh Test Hole

LOCATION Grand Marsh, WI

COUNTY Adams **LOGGED BY** David Hart, Marshal Tofte

LATITUDE 43.871756 **LONGITUDE** -89.718205

LOCATION METHOD: *GPS* [x] *AIR PHOTO/TOPO* [ ] *PLSS* [ ] *OTHER* _____

ELEVATION 996 **ELEVATION METHOD:** *DEM* [x] *TOPO* [ ] *OTHER* _____

WELL DEPTH 418 **CASING DEPTH** 200 **DEPTH TO WATER** 17

CASING STICK UP 1 *File Created on:* 11/18/2013 *by:* AMB

Comments: _____

LOGS COLLECTED:

Gamma	x	Fluid Conductivity	x
Caliper	x	Flow Meter- HeatPulse	
Single Point Resistivity	x	Flow Meter- Spinner	x
Self Potential	x	Optical Borehole Imager	x
Normal Resistivity	x	Acoustic Borehole Imager	
Fluid Temperature	x	OTHER: _____	

- flow up is negative, flow down is positive

Unless Noted:

- *all depths are in feet*
- *well depth, casing depth and depth to water are interpreted from geophysical log*
- *datum is the top of casing*

For more information or to obtain collected data not shown please contact us at askageologist@uwex.edu

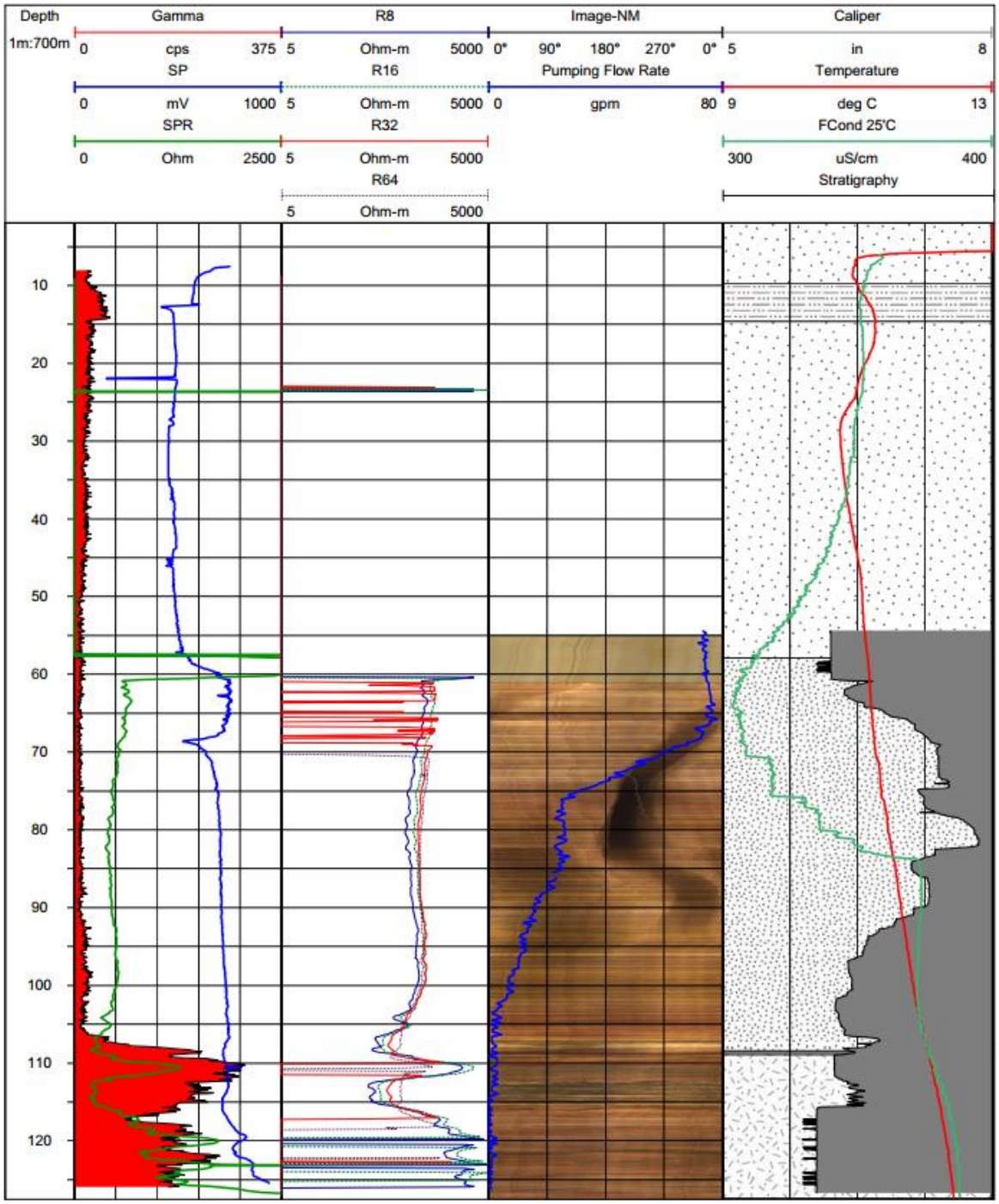
Depth
1m:700m
Gamma
0 cps 375
SP
0 mV 1000
SPR
0 Ohm 2500
R8
5 Ohm-m 5000
R16
5 Ohm-m 5000
R32
5 Ohm-m 5000
R64
5 Ohm-m 5000
Image-NM
0° 90° 180° 270° 0°
Pumping Flow Rate
0 gpm 80
Caliper
5 in 8
Temperature
9 deg C 13
FCond 25'C
300 uS/cm 400
Stratigraphy
10
20
30
40
50
60
70
80
90
100
110
120

Appendix 4: Photo Record of Grand Marsh Study Site

Though the Grand Marsh study site is described in detail in Chapter 4, the content of this appendix serves as a photo reference for the equipment installed there. Readers are directed to Meyer (2013) for additional photos.

Figure 41: Photo of the drilling of the first GHE at the Grand Marsh residence (courtesy of Lauren Meyer).

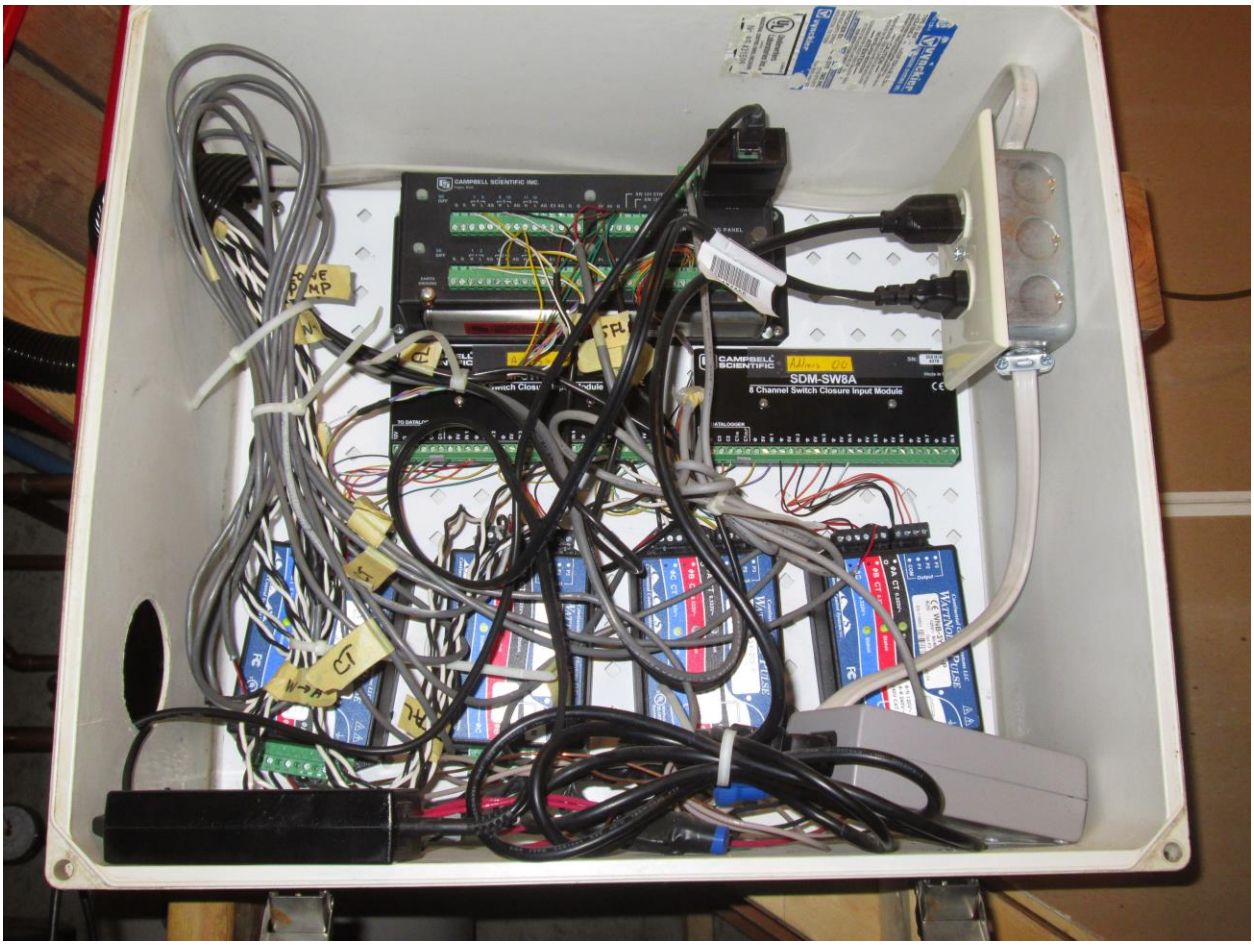

Figure 42: Photo of CR10X datalogger (top), switch closure modules (middle), and WattNodes (bottom) after connecting flow meters (black) but before connection of all system monitoring equipment.

Figure 43: Photo of the two heat pumps at the site, water-to-water at left and water-to air at right. Copper pipes on left carry DHW to and from the water-to-water heat pump. The trio of circulation pumps at center circulate water to the water-to-water heat pump first before traveling to the water-to-air heat pump. Orange PEX tubing at right carry water to and from the desuperheater.

Figure 44: DHW storage tank and associated circulation pumps. At left, pump circulates water from plate heat exchanger to underfloor heating. At center, pump circulates water from DHW tank to water-to-water heat pump. At right, pump circulates DHW to plate heat exchanger.

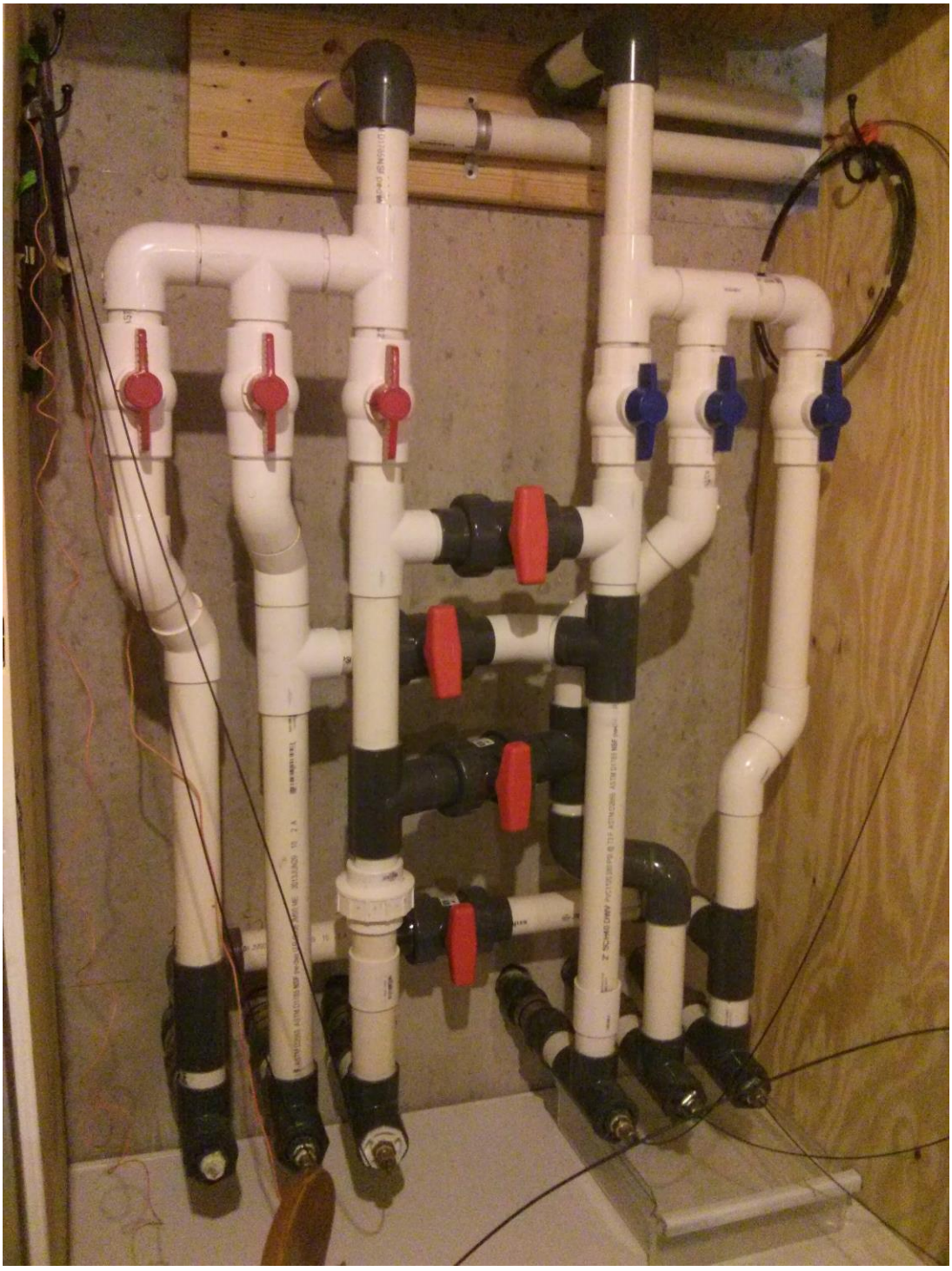

Figure 45: Photo of manifold. At bottom left, water returns to the three GHEs. At bottom right, water returns to the house. Water supply to and from the heat pumps is at top center.

References

Acuña J, Mogensen P, Palm B (2009) Distributed thermal response test on a U-pipe borehole heat exchanger. In Effstock-The 11th International Conference on Energy Storage. Stockholm 2009.

Acuña J, Palm B (2010) A novel coaxial borehole heat exchanger: description and first distributed thermal response test measurements. Proceedings of the World Geothermal Congress 2010.

Acuña J, Palm B (2013) Distributed thermal response tests on pipe-in-pipe borehole heat exchangers. Applied Energy, 109, 312-320.

Acuña J (2013) Distributed thermal response tests: New insights on U-pipe and Coaxial heat exchangers in groundwater-filled boreholes. Doctoral Thesis. KTH Royal Institute of Technology.

ASHRAE (2011) Geothermal energy. In: 2011 ASHRAE handbook - HVAC applications, SI-edition. ASHRAE, pp. 34.10-34.20.

ASTM Standard E1225 (2009) Standard test method of thermal conductivity of solids by means of the guarded-comparative-longitudinal heat flow technique. ASTM International, West Conshohocken, doi: 10.1520/E1225-09

Austin WA (1995) Development of an in situ system for measuring ground thermal properties. MS Thesis. Oklahoma State University.

Bahr JM, Hart DJ, Leaf AT (2011) Distributed temperatures sensing (DTS) as a hydrostratigraphic characterization tool. Final report to the Wisconsin Department of Natural Resources, Open File Report.

Barnoski MK, Jensen SM (1976) Fiber waveguides: a novel technique for investigating attenuation characteristics. Applied Optics, 15(9), 2112-2115.

Beier RA, Acuña J, Mogensen P, Palm B (2012) Vertical temperature profiles and borehole resistance in a U-tube borehole heat exchanger. Geothermics, 44, 23-32.

Blackwell DD, Negraru PT, Richards MC (2007) Assessment of the Enhanced Geothermal System Resource Base of the United States. Natural Resources Research 15.4: 283-308

Brown BA, Massie-Ferch K, Peters RM (2013) Preliminary geologic cross sections of Dane County, Wisconsin. Wisconsin Geological and Natural History Survey, Madison

Carslaw HS, Jaeger JC (1959) Conduction of heat in solids. Oxford University Press, New York

Clauser C, Huenges, E (1995) Thermal condcutivity of rocks and minerals. In: Ahrens T, Rock physics and phase relations - A handbook of physical constants. AGU Reference Shelf, Washington, vol. 3: pp 105-126

Cooper HH, Jacob CE (1946) A generalized graphical method for evaluating formation constants and summarizing well-field history. Transactions, American Geophysical Union 27: 526-534

Dean R, Dixon W (1951) Simplified statistics for small numbers of observations. Analytical Chemistry, 636-638.

Dakin JP, Pratt DJ, Bibby GW, Ross JN (1985) Distributed optical fibre Raman temperature sensor using a semiconductor light source and detector. Electronics Letters, 21(13), 569-570.

Dickie E (2010). Energy exchange: Geothermal exchange and beyond, 3rd edn. Lake Cove, Canada.

Dittus FW, Boelter LMK (1985) Heat transfer in automobile radiators of the tubular type. International Communications in Heat and Mass Transfer 12.1: 3-22

Dott RH, Attig JW (2004) Roadside geology of Wisconsin. Mountain Press Publishing, Missoula

Esen H, Inalli M, Esen Y (2009) Temperature distributions in boreholes of a vertical ground-coupled heat pump system. Renewable Energy, 34(12), 2672-2679.

Farahani MA, Gogolla T (1999) Spontaneous Raman scattering in optical fibers with modulated probe light for distributed temperature Raman remote sensing. Journal of Lightwave Technology, 17(8), 1379.

Figliola RS, Beasley DE (2000) Theory and design for mechanical measurements: Third Edition. John Wiley & Sons, Inc.

Freifeld BM, Finsterle S, Onstott TC, Toole PL, Pratt LM (2008) Ground surface temperature reconstructions: Using in situ estimates for thermal conductivity acquired with a fiber-optic distributed thermal perturbation sensor. Geophysical Research Letters, 35(14).

Fujii H, Okubo H, Nishi K, Itoi R, Ohyama K, Shibata K (2009) An improved thermal response test for U-tube ground heat exchanger based on optical fiber thermometers. Geothermics, 38(4), 399-406.

Gehlin S (1996) TED - a mobile equipment for thermal response test: testing and evaluation. MS Thesis. Lulea University of Technology.

Gehlin SEA, Hellström G (2003) Influence on thermal response test by groundwater flow in vertical fractures in hard rock. Renewable Energy 28: 2221-2238.

Ghafoori-Shiraz H, Okoshi T (1986) Fault location in optical fibers using optical frequency domain reflectometry. Journal of Lightwave Technology, 4(3), 316-322.

Grattan KTV, Sun T (2000) Fiber optic sensor technology: an overview. Sensor and Actuators A: Physical, 82(1), 40-61.

Großwig S, Hurtig E, Kühn K (1996) Fibre optic temperature sensing: A new tool for temperature measurements in boreholes. Geophysics, 61(4), 1065-1067.

Hartog A (1983) A distributed temperature sensor based on liquid-core optical fibers. Lightwave Technology, Journal of, 1(3), 498-509.

Hartog AH, Leach AP, Gold MP (1985) Distributed temperature sensing in solid-core fibres. Electronics letters, 21(23), 1061-1062.

Hausner MB, Suarez F, Glander KE, van de Giesen N, Selker JS, Tyler SW (2011) Calibrating single-ended fiber-optic Raman spectra distributed temperature sensing data. Sensors, 11(11), 10859-10879.

Hecht-Méndez J, Molina-Giraldo N, Blum P, Bayer P (2010) Evaluating MT3DMS for heat transport simulation of closed geothermal systems. Groundwater, 48(5), 741-756.

Hellström G, Mazzarella L, Pahud D (1989) Duct ground heat storage model. Manual for Computer Code, Department of Mathematical Physics, University of Lund, Sweden.

Hennings RG, Connelly JP (1980) Average ground-water temperature map, Wisconsin. Open-File Report. Wisconsin Geological and Natural History Survey. Madison, Wisconsin.

Hurtig E, Großwig S, Jobmann M, Kühn K, Marschall P (1994) Fibre-optic temperature measurements in shallow boreholes: experimental application for fluid logging. Geothermics, 23(4), 355-364.

Hurtig E, Großwig S, Kühn K (1997) Distributed fibre optic temperature sensing: A new tool for long-term and short-term temperature monitoring in boreholes. Energy sources, 19(1), 55-62.

Incropera FP, DeWitt DP (2002) Internal flow. In: Fundamentals of heat and mass transfer, 5th edn. John Wiley & Sons, New York, pp 466-509

Ingersoll LR, Zobel OJ, Ingersoll AC (1948) Heat conduction with engineering and geological application. University of Wisconsin Press, Madison

Jaupart C, Mareschel J (2011) Heat generation and transport in the earth. Cambridge University Press, New York

Kavanaugh S, Rafferty K, Geshwiler M (1997) Ground-source heat pumps: Design of geothermal systems for commercial and institutional buildings. American Society of Heating, Refrigerating and Air-Conditioning Engineers

Kurashima T, Horiguchi T, Tateda M (1990) Distributed-temperature sensing using stimulated Brillouin scattering in optical silica fibers. Optics Letters, 15(18), 1038-1040.

Leaf AT, Hart DJ, Bahr JM (2012) Active thermal tracer tests for improved hydrostratigraphic characterization. *Groundwater*, 50.5: 726-735.

Lee B (2003) Review of the present status of optical fiber sensors. Optical Fiber Technology, 9(2), 57-79.

Lee C, Lee K, Choi H, Choi HP (2010) Characteristics of thermally-enhanced bentonite grouts for geothermal heat exchanger in South Korea. Science in China Series E: Technological Sciences, 53(1), 123-128.

Liebel HT, Huber K, Frengstad BS, Ramstad RK, Brattli B (2010a) Rock core samples cannot replace thermal response tests – A statistical comparison based on thermal conductivity data from the Oslo Region (Norway). In: Proceedings of Renewable Energy Research Conference 2010, Trondheim, Norway, 10 p.

Liebel HT, Huber K, Brattli B, Frengstad B (2010b) Can rock core thermal conductivity data replace thermal response tests?. In: Proceedings of Water and Energy Conference 2010, Amsterdam, Netherlands, 8 p.

Liebel HT, Stølen MS, Frengstad BS, Ramstad RK, Brattli B (2012) Insights into the reliability of different thermal conductivity measurement techniques: a thermo-geological study in Mære (Norway). Bulletin of Engineering Geology and the Environment, 71.2: 235-243.

Lowry CS, Walker JF, Hunt RJ, Anderson MP (2007) Identifying spatial variability of groundwater discharge in a wetland stream using a distributed temperature sensor. Water Resources Research, 43(10).

Lund JW (1990) Geothermal heat pump utilization in the United States. Geo-Heat Center.

Lund J, Sanner B, Rybach L, Curtis R, Hellström G (2004) Geothermal (ground-source) heat pumps–a world overview. GHC Bulletin, 25.3: 1-10.

Meyer L (2013) Thermophysical properties of Wisconsin rocks for application in geothermal energy. MS Thesis, University of Wisconsin-Madison

Oberdorfer P, Holzbecher E, Hu R, Ptak T, Sauter M (2013) A Five Spot Well Cluster for Hydraulic and Thermal Tomography. In Proceedings, 38th Workshop on Geothermal Reservoir Engineering.

Sayde C, Gegory C, Gil-Rodriguez M, Tufillaro N, Tyler S, van de Giesen N, English M, Cuenca R, Selker JS (2010) Feasibility of soil moisture monitoring with heated fiber optics. Water Resources Research, 46(6).

Schmale M, Puffer R, Glombitza U, Hoff H (2011) Online ampacity determination of a 220-kV cable using an optical fibre based monitoring system. In 8th International Conference on Insulated Power Cables.

Selker JS, Thevenaz L, Huwald H, Mallet A, Luxemburg W, van de Giesen N, Stejskal M, Zeman J, Westhoff M, Parlange MB (2006a) Distributed fiber-optic temperature sensing for hydrologic systems. Water Resources Research, 42(12).

Selker JS, van de Giesen N, Westhoff M, Luxemburg W, Parlange MB (2006b) Fiber optics opens window on stream dynamics. Geophysical Research Letters, 33(24).

Sensornet Ltd. Sentinel DTS User Manual. Sen2-UM1.0. Hertfordshire, United Kingdom.

Smolen JJ, van der Spek A (2003) Distributed Temperature Sensing: A primer for Oil and Gas Production. Shell International Exploration and Production. The Hague, Netherlands.

Somerton WH (1992) Thermal properties and temperature-realted behavior of rock/fluid systems. Elsevier.

Sourbeer JJ (2013) Long term soil moisture monitoring and assessing theoretical data interpretation techniques using heated distributed temperature sensing. PhD dissertation. University of Wisconsin-Madison.

Steele-Dunne SC, Rutten MM, Krzeminska DM, Hausner M, Tyler SW, Selker JS, Bogaard TA, van de Giesen NC (2010) Feasibility of soil moisture estimation using passive distributed temperature sensing. Water Resources Research, 46(3).

Striegl AM (2011) Development and field implementation of a distributed soil moisture sensor using heat fiber optics. PhD dissertation. University of Wisconsin-Madison.

Striegl AM, Loheide SP (2012) Heated distributed temperature sensing for field scale soil moisture monitoring. Groundwater, 50.3: 340-347.

Suárez F, Aravena JE, Hausner MB, Childress AE, Tyler SE (2011a) Assessment of a vertical high-resolution distributed-temperature-sensing system in a shallow thermohaline environment. Hydrology and Earth System Sciences, 15(3), 1081-1093.

Suárez F, Hausner MB, Dozier J, Selker JS, Tyler SW (2011b) Heat transfer in the environment: Development and use of fiber-optic distributed temperature sensing. Developments in Heat Transfer. Intech, 611-636.

Theis CV (1935) The relation between the lowering of the piezometric surface and the rate and duration of discharge of a well using ground water storage. Transactions, American Geophysical Union 16: 519-524

Touloukain Y, Judd W, Roy R (1981) Physical properties of rocks and minerals, vol. II-2. Perdue Research Foundation.

Tyler SW, Selker JS, Hausner MB, Hatch CE, Torgersen T, Thodal CE, Schladow SG (2009) Environmental temperature sensing using Raman spectra DTS fiber-optic methods. Water Resources Research, 45(4).

Ukil A, Braendle H, Krippner P (2012) Distributed temperature sensing: review of technology and applications. Sensors Journal, IEEE, 12(5), 885-892.

van de Giesen N, Steele-Dunne SC, Jansen J, Hoes O, Hausner MB, Tyler S, Selker J (2012) Double-ended calibration of fiber-optic Raman spectra distributed temperature sensing data. Sensors, 12(5), 5471-5485.

Wisconsin Department of Administration – Division of Energy (Retrieved January 3, 2015) http://www.doa.state.wi.us/degreedays/

Witte HJL (2013) Error analysis of thermal response tests. Applied Energy 109: 302-311

Walker MD, Meyer LL, Tinjum JM, Hart DJ (2015) Thermal property measurements of stratigraphic units with modeled implications for expected performance of vertical ground source heat pumps. Geological and Geotechnical Engineering Special Issue: Thermo-mechanical Response of Soils, Rocks, and Energy Geostructures. Accepted for publication.

Yilmaz G, Karlik SE (2006) A distributed optical fiber sensor for temperature detection in power cables. Sensors and Actuators A: Physical, 125(2), 148-155.